Master Thesis

Microstructural Effects on the Hydrogen Embrittlement of Dual-Phase Steels

Eirik Leivseth

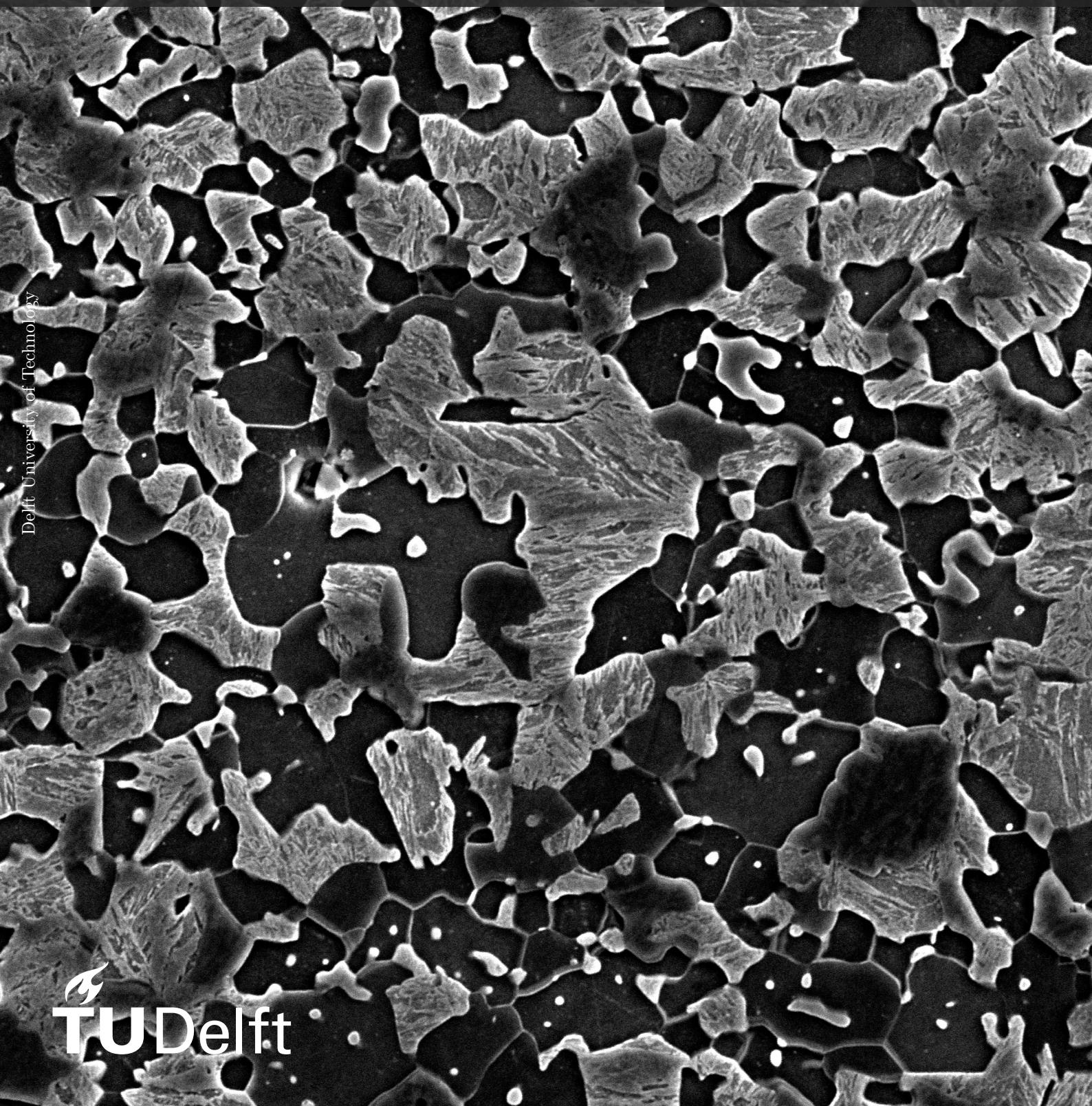

Delft University of Technology

TU Delft

Master Thesis

Microstructural Effects on the Hydrogen Embrittlement of Dual-Phase Steels

by

Eirik Leivseth

A master's thesis submitted in partial fulfillment of the requirement
for the award of the Master of Science (M.Sc.) degree in Materials Science and Engineering,
at Delft University of Technology,
to be defended publicly on July 8, 2024, at 15:30

Student number:	4774353	
Project duration:	November 15, 2023 – July 1, 2024	
Thesis committee:	Dr. Vera Popovich,	TU Delft Department of MSE, supervisor
	Ir. Tim Boot,	TU Delft Department of MSE, supervisor
	Dr. Carey Walters,	TU Delft Department of MTT, external
	Dr. Amarante Böttger,	TU Delft Department of MSE
	Dr. Poulumi Dey,	TU Delft Department of MSE

Cover: Ferrite and martensite microstructure of dual-phase steel after intercritical annealing at 630 $°C$ for 10 min.

TU Delft

Preface

This master's thesis report is the final product of a thesis project spanning the better part of 7 months. The topic of heat treatment of dual-phase steels and its hydrogen embrittlement effects was unknown to me prior to starting this project, but has given me great joy and learning to fully understand the topic and developing the project with my supervisors. Firstly, gratitude is given to my project supervisor, Dr. Vera Popovich, for introducing me to this very fascinating topic and giving me relevant, critical and necessary feedback, suggestions and direction during the duration of the project. A most special gratitude is given to my daily supervisor, Ir. Tim Boot, for many interesting conversations and suggestions giving me constant feedback and direction on the development of the thesis work. Without them, this project would not have been possible.

Furthermore, thanks must be given to the staff at the MSE labs. Particularly, Nico Geerlofs and Raymond Dekker, for helping me with conducting heat treatment using dilatometry and in the Gleeble, giving valuable advice when constructing the heat treatment and making it practically possible to achieve the desired microstructures. Additionally, a thanks to the staff of the mechanical lab, Dr. Ton Riemslag and Elise Reinton, must be made, for giving valuable advice to improve and conduct the mechanical test, helping achieve the desired conditions. Without their aid, this thesis project would not be practically possible.

Finally, special thanks are given to my family back in Norway and the friends I have made in the Netherlands, giving encouragement during this challenging thesis project. They have made the entire M.Sc. program motivating, interesting and fun, giving advice and support during challenging periods. This is greatly appreciated and have made these last two years unforgettable.



Delft, The Netherlands
July 1, 2024

Abstract

To decrease vehicle emissions, automotive manufacturers aim to decrease materials usage. Dual-phase (DP) steels are used in safety critical locations of a vehicle and with stronger DP steels, less material is needed. However, DP steels are known to be affected by hydrogen embrittlement (HE), which decreases the ductility and is thus of significant concern.

This work investigates the effect of heat treatment on the microstructure and HE of DP steel. Heat treatments are developed and conducted using dilatometry, with obtained microstructures characterized using scanning electron microscopy (SEM), optical microscopy (OM), electron backscatter diffraction (EBSD) and hardness measurements. Tensile specimens are heat treated using a Gleeble 3800-GTC thermo-mechanical simulator, before evaluating the HE effect by measuring the total absorbed hydrogen content using thermal desorption spectroscopy (TDS), and determining the static mechanical properties using slow strain-rate tensile (SSRT) testing. The fracture micromechanisms are investigated with fractography using SEM and EBSD with interrupted SSRT and fractured specimens.

The critical transformation temperatures are determined at $686 \pm 1\ ^{\circ}C$ and $571 \pm 10\ ^{\circ}C$ for A_r3 and A_r1 respectively. Intercritical annealing at 590 $^{\circ}C$, 630 $^{\circ}C$, and 670 $^{\circ}C$ results in a martensite content of 25 ± 5 %, 50 ± 4 %, and 78 ± 7 % respectively. Hardness values of 240 ± 31 HV1, 300 ± 9 HV1, and 380 ± 20 HV1 are obtained for the respective intercritical annealing conditions and are an accurate method for comparing the martensite content and microstructure of dilatometry and Gleeble specimens. The martensite distribution changes from a discontinuous network of lath martensite grains with small martensite islands at 590 $^{\circ}C$, to a continuous network of lath martensite without martensite islands at 670 $^{\circ}C$.

TDS yields an increase in the total absorbed hydrogen content of 1.16 ± 0.11 *wppm*, 1.29 ± 0.13 *wppm*, and 1.58 ± 0.27 *wppm* at increasing intercritical annealing temperature, which is attributed to an increase in the ferrite/martensite interface.

Through SSRT the optimal combination of ultimate tensile strength (UTS) and elongation is found at 630 $^{\circ}C$, with UTS of 1025 ± 8 MPa and elongation of 12.6 ± 0.6 %. For all specimens significant HE is observed, with an embrittlement index of 59 ± 7 %, 89 ± 1 %, and 86 ± 3 %, for increasing intercritical annealing temperature. The highest embrittlement at 630 $^{\circ}C$ is attributed to dislocation pile-up around martensite islands, severely increasing embrittlement.

Fractographic investigation revealed the presence of quasi-cleavage fracture bands across the specimen cross-section. This is attributed to preferred crack propagation along martensite bands in the cross-section, with preferred crack nucleation at the martensite surface layer of the specimen short edge. EBSD of the fractured specimen revealed an increase in the kernel average misorientation (KAM) surrounding the ferrite/martensite interface and martensite islands, indicating an increased HE action due to the HEDE and HELP mechanisms.

It is concluded that there is considerable embrittlement of the heat-treated DP steel, which is significantly influenced by the martensite content and distribution. Since DP steels are used in safety critical components, controlling the distribution of martensite in the microstructure is vital, and avoiding surface layer martensite and martensite bands can reduce the HE effect.

Contents

Preface i

Abstract ii

Table of Contents v

List of Figures vi

List of Tables viii

Nomenclature ix

Symbols x

1 Introduction 1

1.1 Use of Advanced High-Strength Steels . . . 1

1.2 Hydrogen Embrittlement . . . 2

1.3 Aim of the Thesis Project . . . 3

1.4 Thesis Structure . . . 3

2 State of the Art 4

2.1 Heat Treatment of DP Steels . . . 4

2.1.1 Critical Transformation Temperatures . . . 4

2.1.2 Determination of Critical Transformation Temperatures . . . 5

2.1.3 Heat Treatments Done on DP steels . . . 7

2.1.4 Microstructural Characterization of DP Steels . . . 9

2.2 Hydrogen Embrittlement . . . 9

2.2.1 Hydrogen Ingress . . . 10

2.2.2 Diffusion and Trapping of Hydrogen . . . 11

2.2.3 Hydrogen Embrittlement Mechanisms . . . 14

2.3 Hydrogen Embrittlement Testing . . . 15

2.3.1 Hydrogen Charging . . . 16

2.3.2 Measuring Hydrogen Content . . . 18

2.3.3 Mechanical Testing of Hydrogen Embrittlement . . . 18

2.3.4 Investigating Fracture Micromechanisms . . . 20

2.4 Hydrogen Embrittlement of DP Steel . . . 20

2.5 Conclusions and Research Objectives . . . 22

2.5.1 Conclusions . . . 22

2.5.2 Research Objectives . . . 24

2.5.3 Approach . . . 24

3 Materials and Methods 25

3.1 Specimen Preparation Methods . . . 25

3.1.1 As-Received Material . . . 25
3.1.2 Tensile Specimen Design . . . 26
3.1.3 Heat Treatment in Dilatometer . . . 27
3.1.4 Heat Treatment in Gleeble 3800-GTC . . . 27
3.2 Materials Characterization . . . 29
3.2.1 Critical Transformation Temperature Determination . . . 29
3.2.2 Microstructure Characterization . . . 30
3.3 Thermal Desorption Spectroscopy . . . 31
3.4 Slow Strain-Rate Tensile Testing . . . 32
3.4.1 Interrupted SSRT with EBSD . . . 35
3.5 Overview of Specimen Tests . . . 37

4 Results and Discussions **38**
4.1 Determination of Critical Transformation Temperatures . . . 38
4.2 Microstructure Characterization . . . 40
4.2.1 Quantification of Martensite Content . . . 40
4.2.2 Qualitative Analysis of Microstructure . . . 44
4.2.3 Comparative Analysis of Microstructure . . . 47
4.3 Thermal Desorption Spectroscopy . . . 48
4.4 Slow Strain-Rate Tensile Testing . . . 50
4.5 Overview of Quantified Results . . . 56
4.6 Fractographic Analysis . . . 56

5 Conclusions **65**

6 Outlook and Recommendations **68**

References **69**

Appendices **I**

A Supporting Python Code - All Data Analysis **I**

B Case study - Tensile Specimen Heat-Treatment Selection **VII**

C Supporting Figures - Critical Temperature Determination **X**

D Supporting Figures - Quantitative and Qualitative Microstructure Analysis **XIII**

E Supporting Figures - Dilatometry and Tensile Specimen Comparison **XVI**

F Supporting Figures - Tensile Specimen Temperature Data and Hardness **XXII**

G Supporting Figures - TDS Plots **XXVI**

H Supporting Figures - Nominal SSRT Stress-Strain Curves **XXVII**

I Supporting Figures - Fractography Images **XXIX**

List of Figures

1 EU emissions by transport mode . . . 1
2 Advanced high-strength steels . . . 2
3 Dual-phase steels used in a vehicle body-in-white . . . 3
4 Iron-Carbon equilibrium phase diagram . . . 5
5 Equilibrium volume fraction of phases development with temperature . . . 6
6 Three different processing routes for DP steel from Adamczyk et al. . . . 8
7 Adsorption and absorption of hydrogen from gaseous and aqueous environment . . . 10
8 Hydrogen trap energies . . . 12
9 Atomic and microscopic scale sites and traps for hydrogen . . . 13
10 Different hydrogen fracture mechanisms . . . 14
11 Hydrogen charging setups . . . 16
12 Schematic of a TDS apparatus . . . 18
13 Example of TDS spectrum from Escobar et al. . . . 19
14 Example of TDS spectrum from Drexler et al. . . . 21
15 Tensile specimen preparation process . . . 26
16 Engineering drawings of tensile specimens . . . 27
17 Tensile specimen clamped in Gleeble . . . 28
18 *Bruker G8 Galileo* oven for TDS analysis . . . 32
19 Benchmarking SSRT testing setup . . . 34
20 HE SSRT testing setup . . . 35
21 Flowchart of techniques conducted on dilatometry and tensile specimen . . . 37
22 Dilatometry curves for the critical transformation temperature determination . . . 38
23 Dilatometry curves for specimen in A_r intercritical region . . . 40
24 Effect of intercritical annealing temperature on martensite content . . . 41
25 Estimated martensite content depending on intercritical annealing temperature . . . 42
26 Effect of time on martensite content . . . 43
27 Qualitative SEM microstructural analysis of dilatometry specimen at magnification 300x . . . 44
28 Qualitative SEM microstructural analysis of dilatometry specimen at magnification 2000x . . . 45
29 SEM of the as-received DP1000 material . . . 46
30 Comparison of hardness (HV1) from heat treatment with dilatometry and in the Gleeble . . . 47
31 Adapted TDS curves for different intercritical annealing conditions . . . 48
32 Total absorbed hydrogen content as function of intercritical annealing temperature 49
33 Engineering stress-strain curves . . . 51
34 Example of correction method for HE nominal strain . . . 52
35 HE engineering stress-strain curves . . . 53
36 Embrittlement index development with intercritical annealing temperature . . . 55

37 SEM fractography of 670 °C benchmarking tensile specimen 57
38 SEM fractography of HE tensile specimen intercritically annealed at 590 °C 57
39 SEM fractography of HE tensile specimen intercritically annealed at 630 °C 58
40 SEM fractography of HE tensile specimen intercritically annealed at 670 °C . . . 59
41 SEM of cross-section of Gleeble specimens 60
42 SEM close-up of cross-section edges of 670 °C specimens 61
43 EBSD KAM images of interrupted SSRT specimens 62
44 EBSD KAM images of SSRT 630 °C and 670 °C specimens 150 μm from fracture edge 63
45 Schematic of the proposed HE action 64
B.1 Comparison table of possible heat treatment methods VII
B.2 Temperature development in Bruker IR furnace VIII
B.3 Various designs of the Gleeble trial specimens VIII
B.4 Temperature development for Gleeble trial specimens IX
C.1 Example of determination of critical transformation temperatures X
C.2 Additional dilatometry XII
D.1 Effect of intercritical annealing temperature on martensite content from SEM images XIII
D.2 Effect of intercritical annealing temperature on ferrite content from OM images . . XIII
D.3 Effect of intercritical annealing temperature on martensite content from EBSD images XIV
D.4 Effect of intercritical annealing time on martensite content from SEM images . . . XIV
D.5 Effect of intercritical annealing time on ferrite content from OM images XIV
D.6 SEM images of dilatometry specimen intercritically annealed at 610 °C, 630 °C, and 650 °C XV
D.7 SEM of dilatometry samples intercritically annealed for 5 and 15 minutes XV
E.1 Hardness (HV1) profile of specimens heat treated with dilatometry and in the Gleeble XVI
E.2 SEM comparison images at magnification 2000x for dilatometry and Gleeble specimen XVIII
E.3 SEM comparison images of tensile specimen intercritically annealed at 590 °C . . . XIX
E.4 SEM comparison images of tensile specimen intercritically annealed at 630 °C . . . XX
E.5 SEM comparison images of tensile specimen intercritically annealed at 670 °C . . . XXI
F.1 Temperature profiles of Gleeble trial specimens XXII
F.2 Hardness (HV1) profile of specimens heat treated in the Gleeble XXIV
F.3 Vertical hardness profile (HV1) for Gleeble specimens XXV
G.1 Full TDS curves obtained during measurement XXVI
G.2 TDS curve of the electrode furnace crucible XXVI
H.1 HE SSRT engineering stress-strain curves XXVII
H.2 HE SSRT load-train displacement curves XXVIII
I.1 SEM fractography of 590 °C benchmarking tensile specimen XXIX
I.2 SEM fractography of 630 °C benchmarking tensile specimen XXIX
I.3 SEM close-up of cross-section edges of 590 °C specimen XXX
I.4 SEM close-up of cross-section edges of 630 °C specimen XXX

List of Tables

1 Literature heat treatments . . . 7
2 DP mechanical properties obtained by Adamczyk et al. . . . 8
3 Relative trapping site strengths . . . 13
4 Comparison of properties of DP steels . . . 21
5 DP steel composition . . . 25
6 Heat treatment of specimen using dilatometry . . . 27
7 Gleeble heat treatment program . . . 28
8 Critical transformation temperature determination heat cycles . . . 29
9 Overview specimen counts . . . 37
10 Critical transformation temperatures . . . 39
11 Effect of intercritical annealing temperature on martensite content based on microscopy technique . . . 42
12 Effect of intercritical annealing time on martensite content based on microscopy technique . . . 43
13 Martensite grains size with increasing intercritical annealing temperature . . . 46
14 Comparison of hardness (HV1) from heat treatment with dilatometry, Gleeble and as-received material . . . 47
15 Total absorbed hydrogen from TDS . . . 49
16 Ferrite/martensite interface to martensite area ratio . . . 50
17 Benchmarking SSRT mechanical properties . . . 52
18 HE SSRT mechanical properties . . . 53
19 Calculated embrittlement index . . . 54
20 Overview of quantified results . . . 56

Nomenclature

Nomenclature

AHSS	Advanced High-Strength Steels
AIDE	Adsorption Induced Dislocation Emission
ASTM	American Society for Testing and Materials
BCC	Body Centered Cubic
BCT	Body Centered Tetragonal
BiW	Body-in-White
CP	Complex-Phase
DP	Dual-Phase
EAC	Environmentally Assisted Cracking
EBSD	Electron Backscatter Diffraction
EDM	Electron Discharge Machining
GND	Geometrically Necessary Dislocations
HE	Hydrogen Embrittlement
HEDE	Hydrogen-Enhanced Decohesion
HELP	Hydrogen-Enhanced Localized Plasticity
ISO	International Organization for Standardization
KAM	Kernel Average Misorientation
OM	Optical Microscopy
OCP	Open Circuit Potential
SEM	Scanning Electron Microscope
SCE	Saturated Calomel Electrode
SSRT	Slow Strain-Rate Test
TDS	Thermal Desorption Spectroscopy
TEM	Transmission Electron Microscopy
TRIP	Transformation Induced Plasticity
UTS	Ultimate Tensile Strength
XRF	X-ray Fluorescence

Symbols

Mathematical Symbols and Units

A_c1	K	Start temperature of austenite formation during heating
A_c3	K	End temperature of austenite formation during heating
A_r1	K	End temperature of ferrite formation from austenite during cooling
A_r3	K	Start temperature of ferrite formation from austenite during cooling
D	$\frac{m^2}{s}$	Diffusion coefficient
D_0	$\frac{m^2}{s}$	Maximal theoretical diffusion coefficient
E_a	$\frac{J}{mol}$	Activation energy for diffusion
I	%	Hydrogen embrittlement index
J	$\frac{mol}{m^3 \cdot s}$	Diffusive flux
M_s	K	Martensite start temperature
M_f	K	Martensite finish temperature
R	$\frac{J}{K \cdot mol}$	Gas constant (8.314 $\frac{J}{K \cdot mol}$)
RA	m^2	Reduction in area
T	K	Absolute temperature
T_Q	K	Temperature under M_s to which sample is cooled
$V_V^{\alpha'}$	–	Volume fraction of martensite
β	–	Constant equal to approximately -0.011
ε	m	Elongation

1 Introduction

At the 2015 United Nations Climate Change Conference, the Paris Agreement, all signatory nations agreed to substantially reduce emissions [1]. The main goal of reaching net-zero by 2050 was made to reduce the potentially disastrous effects of climate change. This impacts all levels of society, and the search of new methods for the use of energy and materials is imperative. In the Netherlands, the nationwide program *Groen Vermogen* (transl. Green Power) works to increase the market for green hydrogen [2]. There have been significant investments by the Dutch government towards this, with €250 million being invested in *Groen Vermogen* in 2022 [3]. Research into the use of hydrogen and its effect on materials is therefore highly relevant.

As a result of these politically made decisions, as well as increased consumer attention, there is a drive within the automotive sector to decrease the emissions of their vehicles. As seen in Figure 1, road transportation represented the majority of emission in the European Union within the transportation sector in 2019 [4]. By developing lighter vehicles, reducing material use and fuel consumption, emission can be reduced. Nevertheless, there are strict safety regulations and requirements, to ensure the safety of the occupants of a vehicle in the event of an accident.

In vehicles, advanced high-strength steels (AHSS) are used in strategic sections of the automobile, contributing to the safety of the occupants. Research on AHSS involves increasing the strength of the steel, thereby decreasing emissions with less material needed to uphold safety requirement. However, AHSS are identified to be susceptible to hydrogen embrittlement (HE), which lowers the ductility of the steel, causing premature fracture at lower stress and strain levels. This offers a significant safety concern and this thesis aims to contribute to the important research into AHSS and HE.

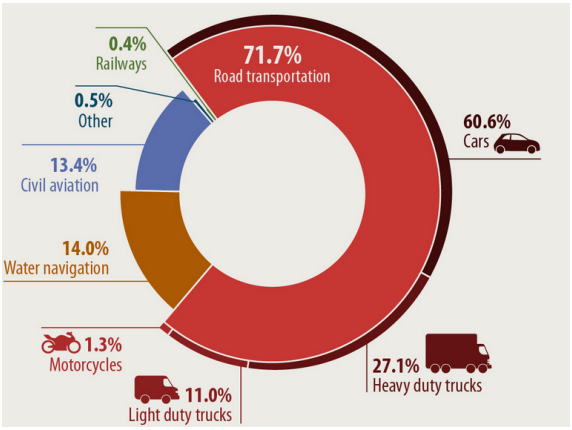

Figure 1: Breakdown of greenhouse gas emissions of the EU by transport mode in 2019. [4]

1.1 Use of Advanced High-Strength Steels

Vehicle manufacturers together with steelmakers developed AHSS in the mid-late 1970s, to decrease vehicle weight. It is estimated that a $20 - 30$ % weight reduction is possible by utilizing AHSS rather than conventional steels [5]. These steels are primarily used in the chassis of a vehicle, which accounts for $\sim$ 45 % of the total weight of a vehicle. By increasing the strength of such components, significant weight reductions can be achieved.

There are three generations of AHSS, with the mechanical properties being compared in Figure 2. While the second generation has the highest lightweight potential, they rely heavily on alloying elements, giving high production costs and poor productivity [6]. The third generation attempts to bridge the gap between the first and second generations, and is currently in development. However, complete control over the microstructural development is not yet attained, and therefore they are not in use [5]. The first generation, consisting of dual-phase (DP), complex-phase (CP), transformation induced plasticity (TRIP) and martensitic steels are the most used of the AHSS. As seen in Figure 2, TRIP and martensitic steels have higher ductility and strength respectively, while DP and CP steels are a compromise between the two.

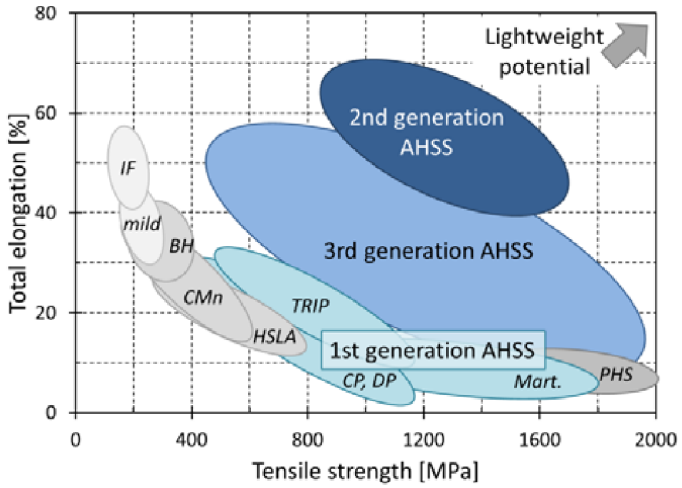

Figure 2: The tensile strength and total elongation properties of different advanced high-strength steels, of the first, second and third generation. Development of steels toward the upper right corner of the figure result in a greater lightweight potential. [7]

Of the AHSS, DP steels are primarily used in automotive applications. As evident from Figure 3, DP type steels account for 29.2 % of the steel used in a *Ford Fusion* body-in-white (BiW), which is the joined frame of the vehicle [8]. Furthermore, DP steels are used in locations critical for the safety of the occupants of the vehicle in the event of an accident. High toughness while retaining ductility is important to withstand deformation and absorb impact energy. DP steels consist of two phases, martensite grains and islands with a surrounding ferrite matrix [6]. The martensite provides strength and toughness, while the ferrite gives the steel ductility.

1.2 Hydrogen Embrittlement

Since DP steels are used in locations of the BiW important for the safety of the vehicle, and with a goal of reducing material use and weight, the margins on the performance of DP steels are narrow. AHSS, including DP steels, are known to be susceptible to HE [9, 10]. Hydrogen, being the smallest element, can easily enter a steel, obstructing the movement of dislocations, decreasing the ductility of the steel. This offers a significant safety concern, making the investigation and understanding of the HE effect on AHSS, particularly DP steels, important. Generally, with increasing material strength, there is an increasing HE effect.

While the HE effect on steels have been known since the work of Mr. William H. Johnson in 1875 [11], there are many challenges remaining to be addressed by research, to gain a full understanding

of the HE effect. With the expanding use of HE susceptible materials, and the emergence of a greener hydrogen market, this research is becoming more relevant than ever.

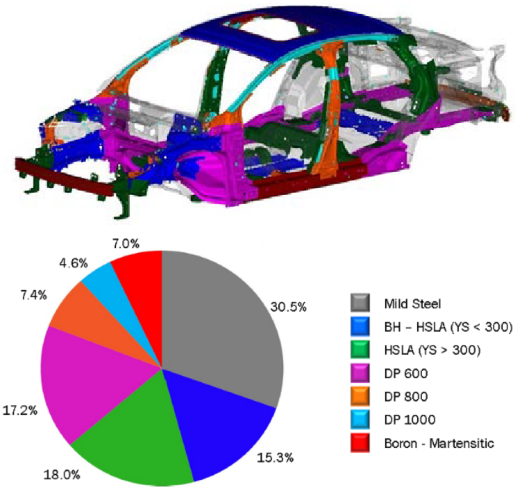

Figure 3: Different steels used in a vehicle's BiW. DP types account for 29.2 % of the total steel used in the BiW of a 2013 *Ford Fusion*, being used in structurally important locations. [12]

1.3 Aim of the Thesis Project

DP steels are used in safety critical locations of vehicles, while being susceptible to hydrogen embrittlement. The safety margins become narrow when the material weight is decreased as automotive manufactures use stronger DP steel, making HE a greater issue. Understanding how the HE affects DP is of great interest. While the mechanical degradation is well characterized in literature, there is a lack of understanding of the effect of heat treatment on the microstructure and the HE effect. Furthermore, the underlying fracture micromechanisms require more attention.

This thesis project is the final part of obtaining the *MSc Materials Science & Engineering* master's degree at *TU Delft*. It has the main focus of understanding the effect of heat treatment on the microstructure, and the effect of the heat treatment and microstructure on hydrogen embrittlement of DP steels by understanding the change in mechanical performance and finding the fracture micromechanisms.

1.4 Thesis Structure

The thesis is divided into distinct sections, based on the standard of an academic report. Section 2 is a comprehensive literature review, reviewing the state-of-the-art on the effect of heat treatment on DP steel, the effect of HE on DP steel and the principles of HE testing, while uncovering important research gaps, to be answered in this thesis. Section 3 describes the procedure for the experimental part of the work: characterizing the heat treatment, the microstructure and the HE effect. Section 4 presents and discusses the obtained results. The thesis is concluded in Section 5, where the final conclusions are made based on the various results and discussions, with the outlook and recommendations for further works on the effect of HE on DP steels being given in Section 6.

2 State of the Art

This section outlines the current state-of-the-art from academic works, as a preparation for the experimental work done in this thesis. Firstly, fundamental considerations regarding the heat treatment of DP steels are conducted, including the examination of different methods of microstructural characterization of DP steel. Secondly, the underlying principles of HE are briefly explained, with a primary focus on the reported effect of HE on DP steels. Relevant techniques for capturing the HE effect on DP steels are then examined. At the end of this section, the main conclusions from the investigation into the state-of-the-art are presented, highlighting the existing research gaps. This leads to the research objectives of this thesis, alongside a brief explanation of how the thesis is approached based on the research objectives.

2.1 Heat Treatment of DP Steels

There are multiple processing routes that lead to a DP microstructure in steel. Common for all routes is the use of intercritical annealing to obtain a certain phase fraction of ferrite and martensite, tuning the strength and ductility of the steel [13]. By changing the annealing temperature and time, different microstructures, with different phase contents of martensite and ferrite, are obtainable. The temperature boundaries of the intercritical region are the critical transformation temperatures, and must be determined for a specific steel composition to create a DP microstructure from heat treatment.

2.1.1 Critical Transformation Temperatures

The critical transformation temperatures for steel are based on the iron-carbon equilibrium phase diagram, and indicate the upper and lower boundaries of the two-phase austenite and ferrite region, indicated in Figure 4 [14, 15]. For a given carbon content, the critical transformation boundary becomes a single temperature point. In the iron-carbon equilibrium phase diagram, the critical transformation values shown are the equilibrium temperatures. They change depending on whether the steel is heated or cooled, as well as the rate of heating/cooling. The A_c1 temperature corresponds to the point at which the eutectic reaction occurs, where austenite starts to form during heating. A_c3 indicates the temperature at which the austenite transformation reaction completes during heating, and the steel consist completely of austenite. Similarly, the A_r3 temperature is the start of the ferrite formation reaction during cooling, while A_r1 is the finalization of the ferrite formation reaction during cooling.

At A_c1/A_r1 and A_c3/A_r3, the steel will consist of 100% ferrite and 100% austenite, respectively. This is seen in Figure 5. Holding at temperatures between these two boundaries will result in obtaining an equilibrium phase fraction of ferrite and austenite. Therefore, by controlling the intercritical annealing temperature, the ferrite content is governable.

Since DP steel consist of ferrite and martensite, the martensite start temperature M_s is a relevant critical transformation temperature as well, albeit less important than the A_c1/A_r1 and A_c3/A_r3 critical transformation temperatures for DP steels. This is due to the intercritical annealing controlling the ferrite content and that the remaining austenite is transformed to martensite during quenching. Since the austenite to martensite transformation is not an equilibrium phase trans-

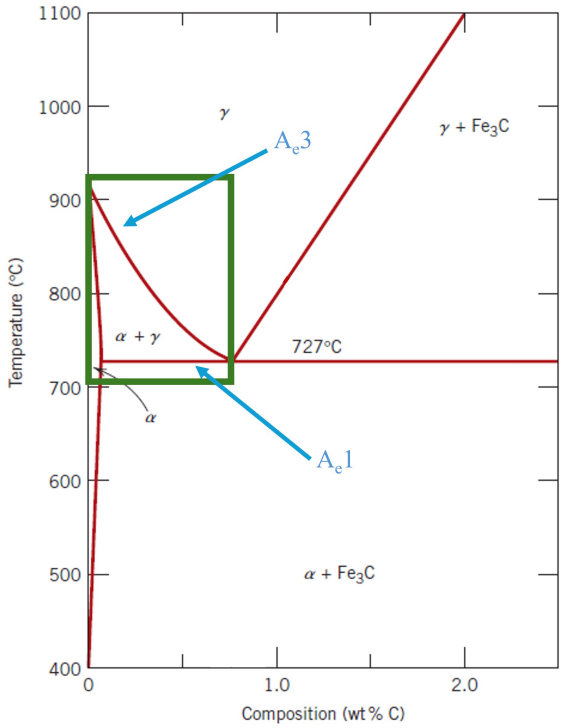

Figure 4: Iron-carbon equilibrium phase diagram showing the stable phases at a certain temperature and carbon content. The equilibrium A_e1 and A_e3 (blue) are indicated in the diagram, making up the two phase austenite and ferrite ($\gamma + \alpha$) region (green box), where a DP microstructure is obtained.[14]

formation, time does not play a role in this reaction [16]. Rather, the degree of undercooling below the M_s temperature controls the amount of austenite that is transformed to martensite. The volume fraction of martensite can be estimated from the Koistinen and Marburger equation, see Equation 1 [17].

$$1 - V_V^{\alpha'} = \exp\left(\beta \cdot (M_s - T_Q)\right) \tag{1}$$

In the equation, $V_V^{\alpha'}$ is the volume fraction of martensite, β is a constant approximately equal to -0.011, and T_Q the temperature to which the sample is cooled. By quenching from the intercritical annealing temperature to room temperature, a large undercooling under the M_s temperature is achieved. Based on Equation 1, a large undercooling results in almost all the remaining austenite from the intercritical annealing being transformed to austenite, with no retained austenite being identified in literature heat treatments.

2.1.2 Determination of Critical Transformation Temperatures

Multiple methods for the determination of the critical transformation temperatures have been developed. This includes using equations based on the chemical composition of the steel, estimations from modeling software such as *Thermo-Calc* and capturing the phase transformation using dilatometry.

Andrews' Equations, developed by K. W. Andrews in 1965, can be used to estimate A_c1, A_c3,

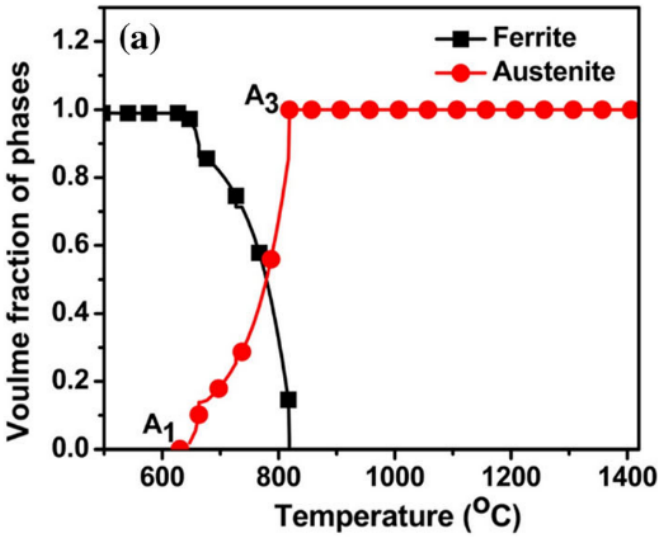

Figure 5: Equilibrium volume fraction of austenite and ferrite phases, obtained by Thermo-Calc in the work of Reddy et al. on DP980. As temperature increases, the austenite phase fraction increases at the expense of the ferrite phase fraction Below $A1$ the steel is 100% ferrite and above the $A3$ it is 100% austenite. [18]

and M_S of low alloy steels with less than 0.6 $wt\%$ C, and are commonly used to determine these critical transformation temperatures [19, 20]. The equations are modeled on experimental results, and are given in Equations 2–4 [21].

$$A_c1\,[^\circ C] = 732 - 10.7 \cdot Mn - 16.9 \cdot Ni + 29.1 \cdot Si + 16.9 \cdot Cr + 290 \cdot As \tag{2}$$

$$A_c3\,[^\circ C] = 910 - 230 \cdot C^{1/2} - 15 \cdot Ni + 44.7 \cdot Si + 104 \cdot V + 31.5 \cdot Mo \tag{3}$$

$$M_s\,[^\circ C] = 539 - 423 \cdot C - 30 \cdot Mn - 17.7 \cdot Ni - 12.1 \cdot Cr - 7.5 \cdot Mo \tag{4}$$

Computational modeling software, such as *Thermo-Calc*, can model the equilibrium phase diagram of a steel depending on its composition, and from that estimate the equilibrium critical transformation temperatures. This method is also commonly used to find the critical transformation temperatures to construct the intercritical region [18, 22, 23].

Dilatometry is a thermal characterization technique frequently used for the investigation of phase transformations occurring in steel during a heat treatment [15]. By measuring the change in length of a sample during heating and cooling, it is possible to capture the phase transformation from ferrite to austenite during heating, austenite to ferrite during cooling and austenite to martensite during quenching. As austenite, ferrite and martensite have different crystal structures, face-centered cubic (FCC), body-centered cubic (BCC), and body-centered tetragonal (BCT) respectively, with different lattice constants, there is a change of volume associated with the change from one phase to another. With dilatometry, it is possible to accurately determine the critical transformation temperatures during heat and cooling of a sample.

In the investigated literature, dilatometry is not used to determine the critical transformation temperatures. Rather, *Thermo-Calc* and Andrew's Equations are used instead, despite dilatometry being the most accurate technique. For the case of *Thermo-Calc*, it only provides the equilibrium

critical transformation temperatures, which are inaccurately presented as the A_c temperatures in literature [18, 23]. Since there is an effect of heating or cooling on the critical transformation temperatures, this is not captured by modeling software. Similarly, Andrews' Equations are estimations from other research, and differences are to be expected for a specific steel composition. Furthermore, there might be local inhomogeneities in the precursor material, that affect the critical transformation temperatures during the heat treatment, not captured by either *Thermo-Calc* or Andrew's Equations. As dilatometry is the most accurate technique to quantify the critical transformation temperatures, it should be included in the development of heat treatments to obtain different martensite contents and microstructures.

2.1.3 Heat Treatments Done on DP steels

Within the investigated literature, significant research has been done on the heat treatment of DP steels. However, there are significant differences in the heat treatment methods, making comparison across literature difficult. An overview of heat treatments done in literature with the corresponding critical transformation temperature technique and heat treatment method is shown in Table 1.

Table 1: Overview of heat treatments done in literature, with the corresponding critical transformation temperature determination technique (CTTDT) and heat treatment method. AUS = austenitization, ANN = intercritical annealing, WQ = water quenching, AQ = air quenching

Author	Source	CTTDT	Heat Treatment Method
Wang et al. (2020)	[23]	*Thermo-Calc*	ANN - WQ
Reddy et al.	[18]	*Thermo-Calc*	ANN - WQ
Bilir et al.	[22]	*Thermo-Calc*	AUS - WQ - ANN - WQ
Khorasani et al.	[20]	Andrews' Equations	AUS - WQ - ANN - WQ
Adamczyk et al.	[19]	Andrews' Equations	I: AUS - AQ - ANN - WQ
			II: AUS - WQ - ANN - WQ
			III: AUS - ANN - WQ

In the work of Wang et al. (2020), intercritical annealing of DP steel in a vacuum tube furnace for 30 min resulted in increasing martensite content (18.5 %, 46.7 %, 68.3 %, and 96.3 %) with increasing annealing temperatures (780, 810, 840, and 870 $°C$) [23]. It was further found that at martensite contents of 68.3 % and higher, a continuous network of martensite forms.

Similarly, the work of Reddy et al. yielded that intercritical annealing close to A_c1 resulted in a decreased martensite content (38 %), while close to A_c3 resulted in an increased martensite content (66 %), when compared to the as-received condition (59 %) [18]. Additionally, electron backscatter diffraction (EBSD) analysis revealed that increasing martensite content results in a higher kernel average misorientation (KAM) and increasing concentration of geometrically necessary dislocations (GND) in both the ferrite and martensite phases. However, for both the work of Wang et al. (2020) and Reddy et al. an effect of the precursor material on the final microstructure is expected, as no austenitization took place.

Bilir et al. investigated the effect of austenitization temperature and time on DP steel during intermediate quenching [22]. This heat treatment involves first austenitization followed by water quenching to room temperature, resulting in only martensite in the microstructure. Then there is intercritical annealing, where martensite is transformed to austenite which is transformed to ferrite, before quenching and any remaining austenite transforms back to martensite. Their results

yielded that increasing austenitization temperature did not affect the average size of martensite fibers and islands, while increasing austenitization time decreased the amount of martensite islands within ferrite grains. However, different heat treatment methods, not including the intermediate annealing would yield different results. This is due to the final microstructure being obtained from a martensitic precursor rather than an austenitic precursor.

The effect of intercritical annealing time was investigated in the work of Khorasani et al. [20]. In their work, they found an increasing martensite content (40 % to 54 %) as the intercritical annealing time increased from one to ten minutes. Whether the equilibrium martensite content was reached after ten minutes was not identified, as the martensite content at longer intercritical annealing times was not conducted. As for the work of Bilir et al., comparison to other heat treatment methods is difficult. However, with an austenitic precursor, it would be expected that with increasing time a lower martensite content would be obtained. This is due to less time being given for the transformation from austenite to ferrite. Regardless, the intercritical annealing temperature is shown to affect the martensite content to a greater extent than the intercritical annealing time.

The resulting mechanical properties of DP steels made using different heat treatment methods were investigated in the work of Adamczyk et al. [19]. Figure 6 shows the three different processing routes to obtain a DP microstructure. With three different processing routes, tensile test were conducted to find the mechanical properties. The results, shown in Table 2, show that *Route I* have the highest tensile and yield strength, but the lowest uniform and total elongation. *Route II* has the best combination of strength and ductility. Depending on the heat treatment the mechanical properties of the DP steel can be tuned to obtain higher strength or higher ductility.

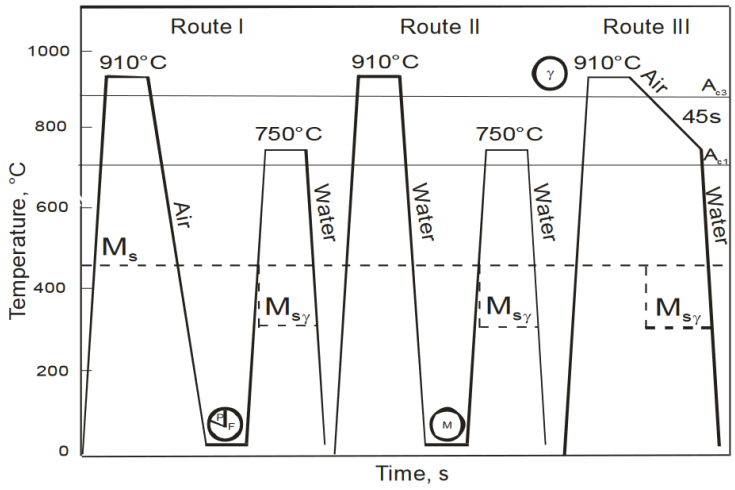

Figure 6: The three different processing routes to obtain a DP microstructure used in the work of Adamczyk et al. [19]

Table 2: Mechanical properties obtained in the work of Adamczyk et al. for DP steels created using three different processing routes. [19] UTS = Ultimate Tensile Strength, YS = Yield Strength, UEl = Uniform Elongation, TEl = Total Elongation.

Route	UTS [MPa]	YS [MPa]	UEl [%]	TEl [%]
Route I	751	501	12.3	15.0
Route II	798	516	16.0	19.3
Route III	998	636	11.7	14.6

2.1.4 Microstructural Characterization of DP Steels

Once a heat treatment has been applied, there are multiple characterization techniques applicable to characterize the obtained microstructure. These include microscopy techniques such as SEM and OM, the diffraction technique EBSD, and mechanical characterization through hardness measurements.

Scanning electron microscopy (SEM) and optical microscopy (OM), are the two most common techniques for microstructural characterization found in literature [18, 24, 25, 26]. OM uses light to illuminate the sample surface, while SEM uses an electron beam which interacts with electrons in the sample surface, creating images for further analysis. To distinguish between the martensite and ferrite phases, etching, in addition to sanding and polishing, must be applied. Commonly, the etching agent *Nital* is used, a mix of nitric acid (3 % or 5 %) and ethanol [24]. Since the martensite and ferrite phases have different resistant towards the etching agent, the phases will be dissimilarly etched, creating a height difference. The height difference will create differences in the interaction between the sample surface and the light/electrons, indicating one phase as lighter/darker than the other. Further image processing using imaging software is required to quantify the phase content, based on SEM and OM images.

Electron backscatter diffraction (EBSD) uses backscattered electrons to obtain insight into the crystal structure and orientation of a sample surface. *Kikuchi* patterns, characteristic of a crystal structure, are generated when backscattered electrons hit a phosphorous screen [27]. Inherently, EBSD cannot distinguish between similar phases, such as ferrite (BCC) and martensite (BCT). However, due to a higher concentration of lattice distortions and dislocations in the martensite phase, there is more electron interference, decreasing the image quality, when compared to ferrite [18]. Therefore, it is possible to distinguish between ferrite and martensite using EBSD. Additionally, EBSD can obtain quantified data regarding grain boundaries and dislocation densities in a sample.

Hardness testing can be used to qualitatively estimate the martensite content of a specimen. Particularly, it can be used to compare the same heat treatment with different techniques. Since martensite is a harder phase than ferrite, an increased martensite content would result in a higher hardness values [16]. Multiple hardness measurement techniques exist, with Vickers hardness being a common one [28]. During Vickers hardness testing, using a diamond-shaped indent with a predetermined force, an indent is made in the surface of the sample. Once the indent is removed, the diagonals of the resulting indentation are measured and related to a hardness value. During hardness testing it is important to capture the macro-properties of the sample, the hardness across multiple grains, rather than the hardness of individual grains, as that would give disparate hardness values for martensite and ferrite grains. While hardness can be used for qualitative comparison of martensite contents, it is not seen in literature regarding heat treatment and HE. This is due to most literature using only one heat treatment method and therefore do not require comparison.

2.2 Hydrogen Embrittlement

HE is the loss of ductility of a metal caused by the entry of hydrogen into the metal [29]. Since hydrogen is the smallest element in the periodic table, it can easily enter metals, obstructing the movement of dislocations and thereby cause embrittlement. As hydrogen prefers to enter interstitial

sites, the solubility of hydrogen is high in many metals. The HE phenomenon is highly complex, making it important to understand the underlying mechanisms and controlling variables.

For a DP steel used in automotive applications, there are multiple possible sources of hydrogen, which can accumulate into the steels, causing embrittlement. Hydrogen can both enter during the manufacturing and the use stages of the material. During manufacturing, processes such as electroplating, acid-pickling and welding can cause the generation of hydrogen, which can accumulate and saturate within the steel. During the use stage of a vehicle, corrosion processes or cathodic protection reactions can result in hydrogen evolution close to the surface of the steel, which can be absorbed into the steel [30].

2.2.1 Hydrogen Ingress

Hydrogen ingress into a metal occurs in two processes. First, there is adsorption of hydrogen from the environment to the metal surface. This occurs either from gaseous hydrogen or hydrogen ions in electrochemical solutions, see Equations 5 and 6 respectively. After hydrogen is adsorbed on the material surface, atomic hydrogen is either recombined into hydrogen gas or as absorbed into the steel. Figure 7 shows the entire hydrogen ingress process from the environment into the steel for both the gaseous and electrochemical case.

$$H_2(g) \rightleftharpoons 2H_{ads} \tag{5}$$

$$H^+ + e^- \rightarrow H_{ads} \tag{6}$$

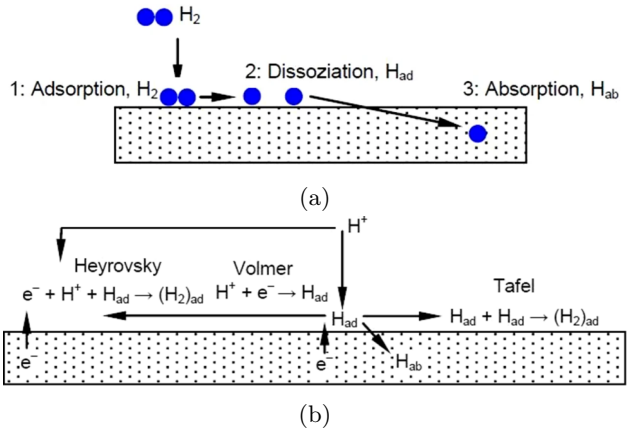

Figure 7: Schematic illustrations of the adsorption and absorption mechanisms of hydrogen from the environment, entering the metal lattice from: a) the gas phase and b) aqueous solutions [31].

For the gaseous case, indicated in Figure 7a, the adsorption occurs first by physisorption, where the hydrogen molecules are physically adsorbed to the surface through van der Waals forces [31]. There is a decrease in free energy on the surface, making adsorption favorable. After physisorption, chemisorption occurs, where the hydrogen molecule dissociates into atomic hydrogen. Atomic hydrogen can either recombine into the hydrogen molecule or be absorbed into the steel, indicated in Equation 7. Whether the atomic hydrogen recombines or is absorbed depend on the surface and

environmental conditions, such as surface roughness, partial pressure of hydrogen and temperature [32].

$$H_{abs} \rightleftharpoons H_{ads} \tag{7}$$

Electrochemical ingress of hydrogen, where hydrogen ions combine with electrons adsorbing on the metal surface, can occur either spontaneously or with impressed currents [31]. The main reaction for the adsorption of hydrogen is the Volmer reaction, depicted in Figure 7b. Once at the surface, different recombination reaction compete with the absorption of hydrogen (Equation 7), namely the Heyrovksy and Tafel reactions (Equations 8 and 9 respectively). Like the gaseous case, whether the hydrogen is recombined and absorbed depends on the local environment and the surface, such as the presence of various recombination inhibitors.

$$H_{ads} + H^+ + e^- \rightarrow (H_2)_{ads} \tag{8}$$

$$H_{ads} + H_{ads} \rightarrow (H_2)_{ads} \tag{9}$$

2.2.2 Diffusion and Trapping of Hydrogen

Once absorbed into the sub-surface of the metal lattice, atomic hydrogen will diffuse further into the lattice. For BCC and BCT lattices, such as ferrite and martensite, the hydrogen preferentially occupies the tetrahedral interstitial sites [33]. Tetrahedral interstitial sites have twice the radius of octahedral interstitials, causing the tetrahedral site to readily accommodate hydrogen. The diffusion of hydrogen throughout the lattice is described by Fick's laws of diffusion.

$$J = -D \cdot \frac{dC}{dx} \tag{10}$$

$$J = -D\nabla C \tag{11}$$

Fick's first law, given in one and three dimensions in Equations 10 and 11 respectively, describes the relationship between the diffusive flux (J, $[\frac{mol}{m^3 \cdot s}]$) and the concentration gradient ($\frac{dC}{dx}$, $[\frac{mol}{m^4}]$) [34]. In the 3D equation, the nabla operator (∇) acts on the scalar concentration field $C(x, y, z, t)$, and produces the concentration gradient field (∇C). D $[\frac{m^2}{s}]$ is the diffusion coefficient, which is as a proportionality constant and material specific property. The flux will move from a high concentration to a low concentration, meaning hydrogen absorbed into the surface layer of the metal has a concentration difference based driving force for diffusion into the bulk of the metal. In research, the effective diffusion coefficient (D_{eff}) is often reported, depending on microstructural features of steel, describing how easy the hydrogen can diffuse through the steel.

$$\frac{\partial C}{\partial t} = D \cdot \frac{\partial^2 C}{\partial x^2} \tag{12}$$

$$\frac{\partial C}{\partial t} = \nabla \cdot (D \nabla C) = D \cdot \nabla^2 C \tag{13}$$

Fick's second law, given in one and three dimensions in Equations 12 and 13 respectively, describe the time dependence of the diffusional process, relating how diffusion changes the concentration gradient with time [34]. It models how the concentration increases or decreases with time ($\frac{\partial C}{\partial t}$, $[\frac{mol}{m^3 \cdot s}]$), depending on the rate of change of the concentration gradient ($\frac{\partial^2 C}{\partial x^2}$, $[\frac{mol}{m^5}]$) and the diffusion coefficient (D). As these are second order partial differential equation, various solutions can be found based on the initial and boundary conditions.

In addition to depending on the microstructure, the diffusion is affected by temperature. Increased temperature facilitates more movement of hydrogen, increasing diffusion. This can be modeled using the Arrhenius equations, given in Equation 14 [34].

$$D = D_0 \cdot \exp \frac{-E_a}{R \cdot T} \tag{14}$$

In the Arrhenius equation, D is the diffusion coefficient at a certain temperature $[\frac{m^2}{s}]$, D_0 is the pre-exponential factor, also known as the maximal theoretical diffusion coefficient $[\frac{m^2}{s}]$. E_a is the activation energy for diffusion $[\frac{J}{mol}]$, R the gas constant $[8.314 \frac{J}{K \cdot mol}]$, and T the temperature that is considered $[K]$.

In a perfect lattice, hydrogen will diffuse through and occupy tetrahedral interstitial sites. However, since a material is not perfect there are other sites in the microstructure with lower associated potential energies compared to the interstitial sites, causing hydrogen to occupy that site instead [30]. This is schematically illustrated in Figure 8. Because of the lower potential energy, significant kinetic energy is required for the hydrogen to leave the site, thereby *trapping* the hydrogen until it is provided. This causes an accumulation of hydrogen in such trapping sites.

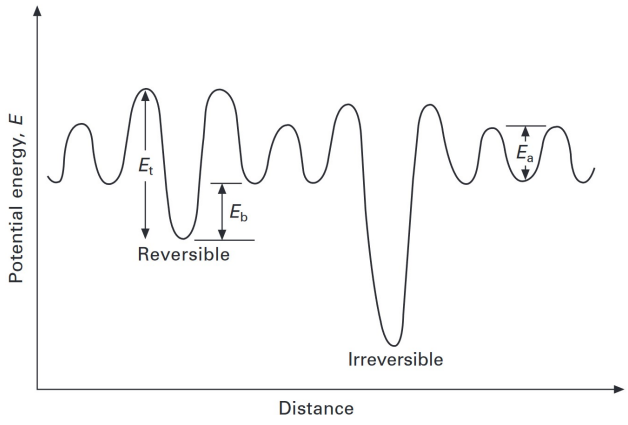

Figure 8: Schematic illustration of the difference in potential energy of interstitial diffusion sites, with activation energy E_a, of reversible and irreversible traps. The reversible trap sites have a trapping energy E_b and an activation energy E_t. [33]

Different microstructural features have different potential energies associated with them, giving them different trapping strengths. Two categories of traps are defined. Reversible traps have a higher potential energy, and lower trapping strength, meaning hydrogen atoms can leave the trap provided enough kinetic energy. Irreversible traps sites have a much lower associated potential energy, giving a near-zero probability of hydrogen leaving the trap. However, with increasing tem-

perature, irreversible trap sites can become reversible as thermal energy is supplied to the system, increasing the probability of hydrogen leaving the trap [33]. Figure 9 shows a schematic illustration of different trapping sites that exist for hydrogen in a metal, on the atomic and microscopic scales.

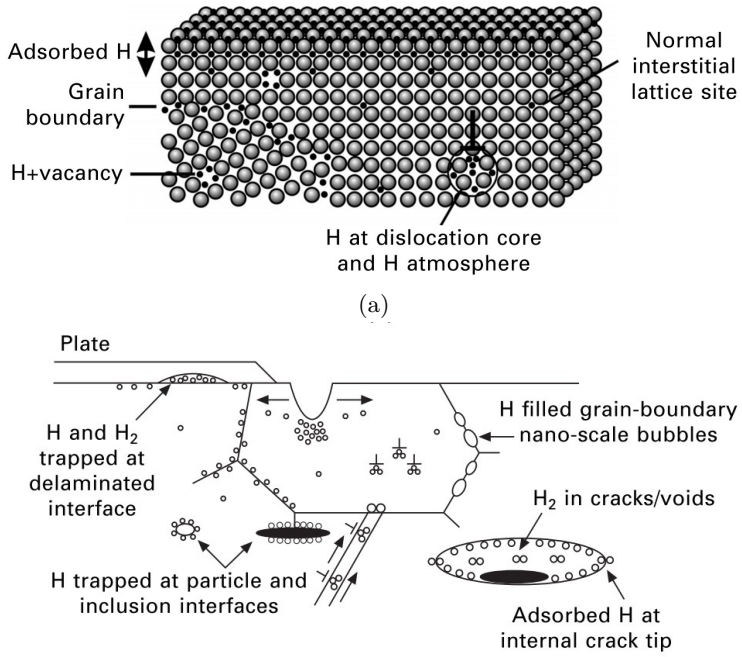

Figure 9: Schematic illustration of different sites and traps for hydrogen on the a) atomic and b) microscopic scales. [30].

Common trapping sites include other microstructural features such as grain and phase boundaries, solute atoms, or inclusion/matrix interfaces. Additionally, trapping sites can be crystal defects, such as vacancies and voids, cracks, and dislocations. Table 3 lists these trapping sites in order of increasing trapping strength.

Table 3: Trapping sites in order of increasing relative trapping strength. [33]

Trapping Strength ↓
Solute atoms
Free surfaces
Vacancies
Dislocations
Grain boundaries
Precipitate/matrix interfaces
Inclusion/matrix interfaces
Voids/internal cracks

The presence of trap sites within the crystal structure affects the diffusivity of hydrogen in the metal. With an increasing number of trap sites and increasing strength of the traps, effective diffusion of hydrogen decreases [33]. Hydrogen atoms remain in the trapping sites and thereby are not diffusing through the lattice. During mechanical exertion, these accumulated trapped hydrogen atoms will leave their traps and migrate towards deformations, causing the hydrogen

embrittlement effect. However, this is only for reversible traps. Since irreversible traps have a near-zero probability of leaving the trap, it is not considered contributing to HE.

2.2.3 Hydrogen Embrittlement Mechanisms

The underlying HE mechanisms remain debated in literature. Multiple mechanisms have been proposed in research, without a consensus being reached [35]. The most common mechanisms are hydrogen-enhanced decohesion (HEDE), hydrogen-enhanced localized plasticity (HELP) and adsorption-induced dislocation emission (AIDE). The three mechanisms are schematically depicted in Figure 10. Recent advances have, however, identified that multiple HE mechanisms occur together, creating a synergetic effect on HE. Djukic et al. detected a simultaneous action of the HELP and HEDE mechanisms depending on the local hydrogen concentration, where HELP dominated at low concentration and a HEDE mechanism manifestation once a critical hydrogen content is reached [35]. Similar result are reported in the work of Wasim et al.[25]. The dominant mechanism for HE fracture can be determined from SEM fractography [36].

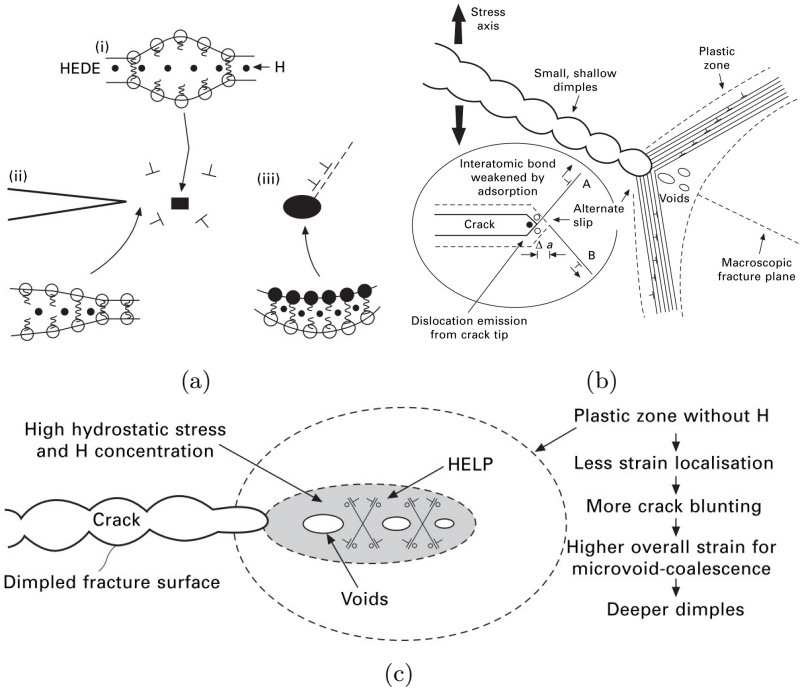

Figure 10: Schematic illustration of the a) HEDE, b) AIDE, and c) AIDE hydrogen embrittlement mechanisms. [30].

Hydrogen-Enhanced Decohesion

The HEDE mechanism, seen in Figure 10a, was first introduced in 1926, and proposes that hydrogen decreases the cohesion of cleavage planes [37]. Later, the mechanism was expanded to include that hydrogen decreases the cohesion of the interatomic iron-bonds, thus causing decohesion [38]. This mechanism has been identified to occur at different locations in the lattice: the atomically sharp crack tip due to absorbed hydrogen, slightly ahead of the crack tip at the tensile-stress maximum due to dislocation shielding effects, further ahead of the crack tip at positions of maximum hydrostatic stress, and at particle-matrix interfaces ahead of the crack [30]. It is however, debated

whether high enough elastic stresses to reach sufficiently high hydrogen concentrations to cause decohesion is possible. Furthermore, obtaining experimental evidence is difficult, as no techniques to observe the crack tips of bulk material at the atomic scale exist. Since the hydrogen causes a weakening of the interatomic iron bonds, it can be explained that this causes a weakening of mechanical properties and less stress is required for final failure of the metal.

Hydrogen-Enhanced Localized Plasticity

HELP, seen in Figure 10c, was first proposed in 1972 and is based on fractographic observations that hydrogen concentrations were close to crack tips due to hydrostatic stresses or hydrogen entering at the crack tip [39]. Linear-elastic calculations show the repulsive force between dislocations and obstacles is lessened with hydrogen being present, while atomistic simulations show that there is a decrease in dislocation-core energy due to hydrogen, making dislocation movement easier [30]. Furthermore, in-situ Transmission Electron Microscope (TEM) observations show that when hydrogen diffuses into the specimen, stationary dislocations begin to move and moving dislocations increasing their velocity. Some softening of bulk specimens are also observed. Changes in the spacing and height of slip planes, as well as the number of active slip systems due to hydrogen, which can be both beneficial and detrimental, have been reported. Based on the mentioned evidence, it was proposed that deformation is localized next to crack tips due to solute hydrogen facilitating dislocation activity. A prerequisite for HELP is the diffusion of hydrogen ahead of the crack tip. As the crack path is transgranular or intergranular, the occurrence of the HELP mechanisms depend on the region of a high hydrogen concentration, within the grain or at the grain boundary. Nevertheless, in HELP, hydrogen causes easier dislocation movement, facilitating plastic deformation, which explain the decrease in ductility caused by HE.

Adsorption-Induced Dislocation Emission

AIDE, seen in Figure 10b, was proposed in 1976, after the aforementioned mechanisms [40]. It was first suggested that adsorption of hydrogen leads to dislocation nucleation on a surface [41]. This was developed into AIDE, where dislocation emission involves the dislocation nucleation of at the crack tip, with the dislocation subsequently moving away from the crack tip. Hydrogen adsorption is critical for dislocation nucleation, facilitated by a weakening of the interatomic iron-bonds. The surface layer provides lower potential energy sites than the bulk lattice, causing higher hydrogen concentrations at the surface than the bulk, affecting crack initiation sites. Furthermore, atomistic simulations provide evidence that dislocations are more easily emitted in the presence of hydrogen. In the AIDE mechanism, hydrogen encourages the nucleation dislocations, influencing the mechanical properties of the steel.

2.3 Hydrogen Embrittlement Testing

To evaluate the effect of hydrogen embrittlement on a steel, multiple techniques have been developed. This includes methods of charging hydrogen into a sample, measuring the absorbed hydrogen content and the mechanical characterization of the HE effect.

2.3.1 Hydrogen Charging

Hydrogen can enter a material in the gaseous state or from electrolytic solutions, as described in Section 2.2.1. For HE testing purposes, hydrogen can be deliberately charged into a sample. This can occur either using gas or cathodic charging, with the charging setups for gaseous and electrochemical charging schematically shown in Figure 11. Electrochemical cathodic charging is most common in literature. In the comparison between electrochemical and gaseous charging done by Zhao et al., it was determined that electrochemical charging resulted in considerable more absorbed hydrogen (3.49 wppm) than gaseous charging (0.24 wppm) [42]. Electrochemical charging provides a higher driving force for hydrogen absorption than gaseous charging. Furthermore, electrochemical charging gives a charging environment similar to that which is expected for DP steel used in automotive application, where hydrogen is present trough electrochemical corrosion and cathodic protection reactions.

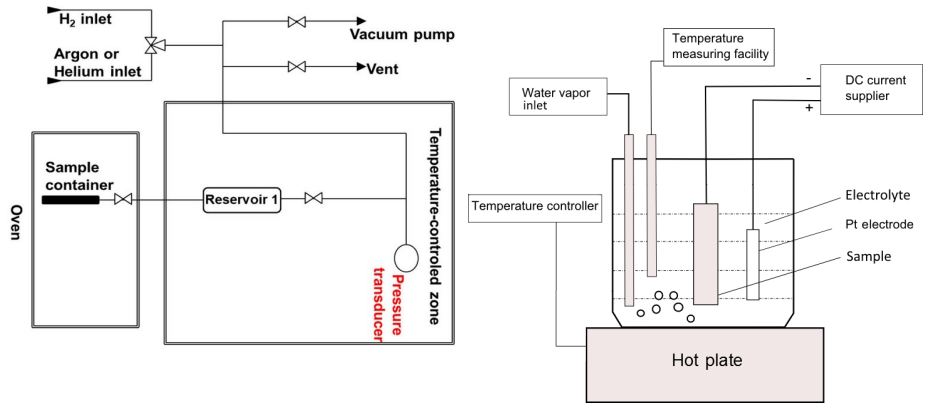

(a) (b)

Figure 11: Schematic illustrations of a) a Sieverts apparatus for hydrogen charging [43], and b) an electrochemical hydrogen charging setup [44].

Gaseous Charging

Gaseous charging of hydrogen occurs with the use of a Sieverts apparatus, seen in Figure 11a [42]. By utilizing a high H_2 pressure, ad/absorption of hydrogen into a sample is achieved. H_2 pressures up to 10 MPa are common [42, 43], although pressures reaching 150 MPa have been reported [45]. However, with varying the pressure from 7 to 15 MPa no additional hydrogen fatigue behavior was reported with higher pressure. To increase ad/absorption, the temperature can be increased, encouraging diffusion.

Using a Sieverts apparatus, it is possible to measure the absorbed hydrogen directly, based on the measured pressure difference measured during charging. Additionally, during discharging of hydrogen (dehydrogenation) the temperature can be elevated to promote the removal of the hydrogen from trapping sites within the lattice. However, there are significant safety risk associated with gaseous hydrogen, due to high flammability. This limits the H_2 gas pressure that can be used for charging.

It was found in the work by Zhao et al. that gaseous charging creates a uniform distribution of hydrogen in the sample [42]. Since a relatively low amount of hydrogen is absorbed during gaseous charging, a softening effect on the metal is observed. This is explained by an enhanced screw

dislocation mobility or the nucleation of double kinks, softening the material.

Electrochemical Charging

Electrochemical cathodic charging uses either an impressed current or impressed potential to force hydrogen into a sample. In an electrochemical cell, seen if Figure 11b, the sample is the working electrode (cathode), where hydrogen ions are reduced on the sample surface through the aforementioned Volmer reaction (Equation 6). The counter electrode is an inert material, such as platinum or stainless steel. As for gaseous charging, the temperature can be controlled to encourage ad/absorption.

Multiple electrolytes, with the main purpose of providing H^+ ions to the solution through the electrolysis of water, are used in literature. Common ones include sodium hydroxide ($NaOH$) [10, 31, 36, 46, 47], sulfuric acid (H_2SO_4) [26, 31, 42, 48], and sodium chloride ($NaCl$) [49, 50, 51]. When selecting an electrolyte, considerations must be made regarding the pH of the solution and any potential effect of the pH on hydrogen charging. Sodium hydroxide has a high pH, while sulfuric acid has a low pH. Sodium chloride is neutral, not affecting the pH of a solution.

To encourage the absorption of hydrogen adsorbed to a surface, rather than recombination into hydrogen gas, recombination inhibitors are added to the electrolyte. These inhibit the gas formation reaction. Common elements found in these inhibitors are S, P, As, Sn, Pb, Se and Te [52]. The most common recombination inhibitor is *thiourea* ($SC(NH_2)_2$) [26, 31, 36, 47, 48, 52]. However, it is reported that thiourea oxides to formamidine disulfide at an open circuit potenital (OCP) of -1650 mV vs. SCE (saturated calomel electrode) [53]. Additionally, bubble formation, indicating recombination of hydrogen, has been observed at an OCP of 1.5 V vs. a saturated Ag/AgCl reference electrode [52]. This indicates that at certain OCPs thiourea is ineffective as a recombination inhibitor. Ammonium thiocyanate (NH_4SCN) has been identified as an alternative to thiourea, although it is not yet prevalent in research. However, a 25-fold increase in hydrogen permeation current is reported using 3 g/L NH_4SCN compared to no recombination inhibitor [54]. Further, it was identified that ammonium thiocyanate decreased the absorption activation energy, while increasing the activation energy for adsorption. Using ammonium thiocyanate leads to slower adsorption of hydrogen from the electrolyte to the surface, but faster absorption into the sample once at the surface.

During electrochemical charging, the controlling factor is the current density, where a higher current density gives a greater driving force for absorption [42]. Furthermore, time and temperature influences the rate of absorption. Longer charging times will mean more hydrogen is absorbed. However, the sample will eventually saturate with hydrogen, as traps are getting filled. The surface conditions are an additional important parameter for electrochemical charging. As available surface sites are needed for the adsorption of hydrogen, the surface roughness can encourage or hinder the rate of hydrogen absorption [55]. In the work of Zhao et al. it was found that electrochemical charging of hydrogen causes a hardening of the sample [42]. The high concentration of hydrogen causes a segregation of dislocations, with a surrounding hydrogen atmosphere. Pinning of the dislocation then occurs, which increases the stress required for plastic deformation, hardening the material.

2.3.2 Measuring Hydrogen Content

Thermal desorption spectroscopy (TDS) is a technique to quantitatively measure the hydrogen trapping characteristics of bulk metal, schematically shown in Figure 12. The technique studies the desorption kinetics of hydrogen in a sample precharged sample using a non-isothermal measuring method [56].The sample is heated up causing the hydrogen within the material to desorb and recombine into a gas, which is then moved to a mass spectrometer using vacuum or a carrier gas. The mass spectrometer measures the hydrogen content of the flowing gas, which is then sent to the computer to generate a TDS spectrum. In addition to the total hydrogen content, the area under the TDS curve, peaks in the spectrum indicate hydrogen being released from traps at specific temperatures. Since various trapping sites are associated with different binding energy (trapping strength), distinct temperatures provide sufficient thermal energy for the hydrogen to leave the traps [57]. Therefore, it is possible to determine in which microstructural features the hydrogen is located.

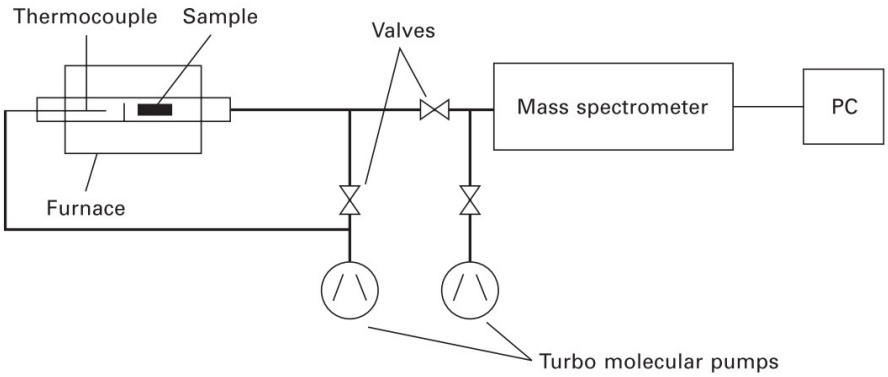

Figure 12: Schematic illustration of a thermal desorption spectroscopy apparatus, showing how the sample is heated and then the desorbed hydrogen goes through pipes and values to the mass spectrometer, where the amount of hydrogen is detected. [56]

An important drawback of the TDS technique and corresponding spectrum is that if an overlap between hydrogen trapping energies and the hydrogen escape kinetics exist, the peaks will be non-distinguishable [57]. If the lattice hydrogen diffusion activation energy is high, then analyzing the trapping energy of traps will difficult. Additionally, since BCC steels are characterized by a high intrinsic lattice diffusion of hydrogen, analyzing weak traps becomes very time sensitive, as diffusion starts immediately after charging. This occurs even at cryogenic temperatures [57]. Therefore, the time between the hydrogen charging TDS analysis becomes vital. An example is seen in the results of Escobar et al., seen in Figure 13 [58]. In their investigation of the time between hydrogen charging and TDS measurements of a DP steel, there is a clear result that longer times decrease the amount of hydrogen present in the steel, as it has diffused out under ambient temperatures.

2.3.3 Mechanical Testing of Hydrogen Embrittlement

The mechanical characterization of hydrogen embrittlement is utilized to capture the HE effect on the mechanical properties of materials. This is determined from the embrittlement index (I), which is based on either the reduction in elongation of a sample or the reduction in cross-sectional area at fracture of a sample of a HE affected sample compared to a non-affected sample, during

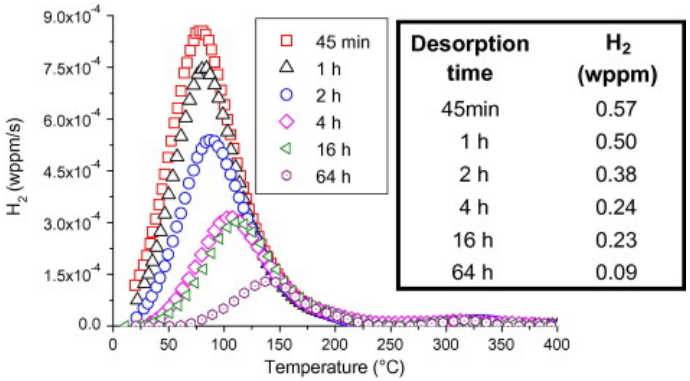

Figure 13: TDS spectrums obtained by Escobar et al. for a DP steel with different times between hydrogen charging and TDS measurement. [58]

tensile testing. The embrittlement index is defined in Equations 15 and 16 for, respectively, the reduction in elongation and reduction in cross-sectional area.

$$I_\varepsilon = \frac{\varepsilon_{ref} - \varepsilon_{HE}}{\varepsilon_{ref}} \cdot 100\% \tag{15}$$

$$I_{RA} = \frac{RA_{ref} - RA_{HE}}{RA_{ref}} \cdot 100\% \tag{16}$$

In the equations above, ε_{ref} and RA_{ref} are, respectively, the elongation $[m]$ and reduction in area at fracture $[m^2]$ of the unaffected reference sample. ε_{HE} and RA_{HE} are, respectively, the corresponding elongation $[m]$ and reduction in area at fracture $[m^2]$ of the HE affected sample.

The mechanical testing of specimens can occur in an ex-situ or in-situ charging environment. In the ex-situ case, hydrogen charging occurs prior to testing, meaning hydrogen will diffuse out of the sample in the time between charging and testing. Like for TDS, this can diminish the HE effect. An in-situ mechanical test involves continuous charging of a sample, while testing occurs. When comparing ex-situ and in-situ testing, ex-situ gives a comparatively smaller embrittlement index ($I \approx 2-3\,\%$) than the in-situ case ($I \approx 16\,\%$) [59]. Therefore, to maximize the investigation of the HE effect, in-situ charging would demonstrate a more detrimental situation, and is preferred over ex-situ testing.

For the evaluation of HE, tensile testing commonly occurs with slow strain-rate tensile (SSRT) tests. SSRT are tensile test where the strain rate is orders of magnitude lower than standard tensile test, typically reaching strain rates in the order of $10^{-6}\ s^{-1}$ [49]. A slower strain rate promotes the stress-induced diffusion of hydrogen, giving time for the diffusional process of hydrogen, causing hydrogen buildup depending on the stress concentrations in the sample. Furthermore, by keeping the strain rate low, the diffusion of hydrogen remains similar to dislocation movement [23]. With decreasing strain rate, a higher embrittlement index has been reported, $I \approx 16\,\%$ at a strain rate of $10^{-3}\ s^{-1}$ and $I \approx 43\,\%$ at a strain rate of $10^{-4}\ s^{-1}$ [59].

SSRT testing is less time-consuming and results in less scatter than other tensile testing methods, such as constant load testing [49]. Furthermore, in-situ SSRT is standardized in ASTM G129 and ASTM G142 [60, 61]. The former encompasses the in-situ SSRT testing of and environment that causes environmentally assisted cracking (EAC) (which includes HE), while the latter describes in-situ SSRT testing of a high pressure hydrogen gas atmosphere [62].

2.3.4 Investigating Fracture Micromechanisms

The investigation of the fracture micromechanisms primarily consists of fractography, the qualitative analysis of a fracture surface using microscopy techniques such as SEM. Material failure occurs either through cleavage, ductile, or quasi-cleavage fracture. Brittle metals generally fail by cleavage fracture. This is the quick crack growth along the highest packing density planes, with little to no plastic deformation [48]. For HE induced failure, cleavage-looking fracture may occur along non-cleavage planes, called quasi-cleavage fracture [63]. Both cleavage and quasi-cleavage fracture is characterized by river markings, running parallel to the crack propagation direction. However, in the work of Martin et al. it is demonstrated that quasi-cleavage fracture is caused through ductile processes, rather than a brittle cleavage-like mechanism, which are enhanced by the presence of hydrogen [63]. This is consistent with the HELP HE mechanism. In the work of Merson et al., it was found while both cleavage and quasi-cleavage fracture looks similar, that normal cleavage fracture strictly follow the crystallography orientation of the grains, while the quasi-cleavage surface had lower misorientation angle and roughness between quasi-cleavage facets [48]. Ductile fracture occurs when significant plastic deformation is present, and is characterized with the formation of dimples on the fracture surface [30]. Furthermore, dimples can be present in HE fracture, with shallow dimples indicative of the HELP and AIDE mechanisms.

Additionally, intergranular fracture along prior austenite grain boundaries is another common fracture mode for HE induced failure for high-strength steels [30]. Intergranular fracture is encouraged as hydrogen is transported from the grain interior to the grain boundaries through dislocation transport, thus decreasing the cohesion at the boundary. This fracture mode can occur for all the presented HE mechanisms (HEDE, HELP and AIDE), however there are distinguishing fracture characteristics. During SEM analysis, intergranular fracture surfaces are shown to be covered by well-defined dimples. This is indicative of the AIDE and HELP mechanisms, facilitating and localizing microvoid coalescence processes.

A new technique to investigate the fracture micromechanisms is the use of interrupted SSRT experiments coupled with ex-situ EBSD measurements. This was recently done in the work of Li et al. [36]. By straining samples to 2.5 % engineering strain during SSRT testing, ex-situ EBSD was used to obtain Kernel Average Misorientation (KAM) maps, investigating the strain distribution during deformation under hydrogen attack. Areas of high deformation will have higher KAM values, and thus indicate the nucleation locations for voids, leading to cracks [64]. As interrupted SSRT with ex-situ EBSD is only recently applied to HE fracture investigations, the potential of the technique helping in elucidating the underlying fracture micromechanisms of HE induced fracture is high.

2.4 Hydrogen Embrittlement of DP Steel

The effect of hydrogen on the mechanical properties of DP steel has extensively been researched. In the work of Drexler et al., the mechanical properties and hydrogen absorption of three different DP steels were investigated [26]. Their results are presented in Table 4. The three DP steels had different martensite content, influencing the mechanical properties, as well as the hydrogen content. As the martensite content increases, so does the absorbed hydrogen content, while the fracture strain decreases. This is seen in the TDS curves obtained by Drexler et al., shown in Figure 14, where there is a higher area under the curve for higher martensite content steel, indicating greater

absorbed hydrogen content. The decrease in fracture strain can be attributed both to the increase in martensite content and to a HE effect. Furthermore, it was reported that increasing ultimate tensile strength (UTS) leads to increased work hardening, significantly affecting the HE susceptibility [65]. The increase in hydrogen content with increasing martensite content was attributed to the main trapping sites for hydrogen being dislocations in the martensite, lath martensite boundaries and the ferrite/martensite interface. Any effect of carbon content in the martensite is not considered. However, in the work of Rodoni et al., it was concluded that the amount of martensite is the main controlling variable for hydrogen diffusion, rather than the martensite carbon content [28].

Table 4: Martensite content, mechanical properties and hydrogen uptake content of the three DP steels investigated by Drexler et al. [26]

Steel	Martensite Content [%]	Yield Strength [MPa]	Ultimate Tensile Strength [MPa]	Fracture Strain [%]	H Content [wppm]
DP600	25	366	659	25	2.07
DP800	44	518	834	19	2.20
DP1000	59	732	1087	13	2.67

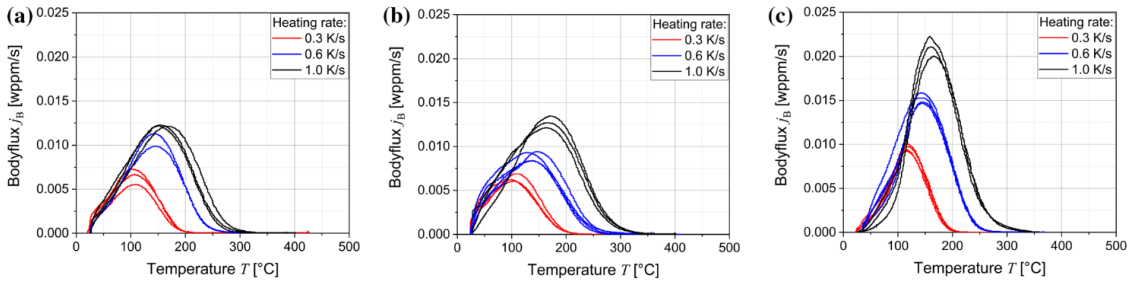

Figure 14: TDS spectrums obtained by Drexler et al. for three different DP steels: a) DP600, b) DP800, c) DP1000. In the spectrums, there is a shift towards the right with higher heating rates. [26]

In the work of Reddy et al., first discussed in Section 2.1.3, the hydrogen permeation properties with increasing martensite contents were investigated [18]. The permeation of hydrogen decreased as martensite content increased. This indicated that the number and types of trapping sites increase with increasing martensite content, supporting the statement that the total martensite content is the controlling variable for hydrogen diffusion. Hydrogen trapping is favored, reducing the permeation and diffusion of hydrogen in through the lattice. Additionally, hydrogen can more easily diffuse through ferrite channels in the microstructure.

Similarly, in the work of Wang et al. (2020) [23], first mentioned in Section 2.1.3, it was found that the hydrogen trapping density increases with increasing martensite content. At low martensite contents, the interface between ferrite and martensite acts as the main trapping site for hydrogen atoms. The diffusion coefficient of hydrogen decreases with increasing martensite content, as more hydrogen is trapped in the martensite. However, for martensite contents above 68.3 % the hydrogen diffusion coefficient stabilizes. A continuous network of martensite in the microstructure is observed at high martensite contents, causing decreased ferrite/martensite interfacial area, easing the diffusion of hydrogen. Another important conclusion of this research is the importance of martensite distribution in the DP steel on the hydrogen diffusion characteristics. If the martensite phase is isolated, diffusion occurs through the ferrite phase, and the ferrite/martensite interface acts as the main trapping site.

The role of the ferrite/martensite interface on the HE behavior of ultra-high strength DP steel (UTS above 1200 MPa), with tempering, was investigated by Takashima et al. [66]. As for Wang et al. (2020), the interface between ferrite and martensite are vital for the HE behavior of the steel. The coherency between the martensite and ferrite phase increases with tempering, decreasing the available trapping sites. Cracks primarily nucleate at the interface between or in the martensite phase, and propagate through both the ferrite and martensite phases. A decrease in crack propagation resistance through the ferrite phase is attributed to a lower coherency in the ferrite/martensite interface, although the HE is not severely increased due to the low coherency. This research does, however, not relate the HE of the steel to the ferrite and martensite phase size and distribution, which in other research is found to be important.

The effect of three different intercritical annealing times (30, 45 and 60 mins) on the HE of DP steels was investigated by Li et al. [36]. Their results indicated that as intercritical annealing time increases, the hydrogen embrittlement first decreases before increasing again. This is attributed to the change in morphology of the martensite phase with increasing annealing times. Interrupted SSRT with ex-situ EBSD test show that, at the lowest annealing time (30 min), there is a higher strain localization (higher KAM values), creating the most secondary cracks, increasing the HE effect. At the longest annealing time (60 min) despite having the lowest strain distribution (lowest KAM values) a chain-network distribution developed, encouraging crack propagation, thus increasing the HE effect. This research indicates that annealing time has an effect on the martensite morphology in the sample, which affects the HE effect. However, as previously established from the work of Khorasani et al. (Section 2.1.3) [20], the intercritical annealing temperature has a greater effect on the martensite content than the intercritical annealing time and thus more influential on the HE effect of the heat treatment on DP steel. Regardless, interrupted SSRT tests with EBSD analysis are shown to be a method of investigating the underlying fracture micromechanisms, by finding strain localizations within a sample.

2.5 Conclusions and Research Objectives

This literature review, which presents relevant state-of-the-art findings on the effect of heat treatment on the microstructure and subsequent HE of DP steels, acts as the fundamental framework for the experimental work of the thesis project. The main conclusion from this work is first presented. Following this, the determined research objectives for this thesis are designated, before some final comments on how the research objectives were approached.

2.5.1 Conclusions

1. DP steels are AHSS that offer a desirable combination of strength and ductility, being used in ~ 30 % of the BiW of a vehicle, reducing weight and emissions to meet politically set climate goals, as well upholding passenger safety. The steel consist of martensite islands within a ferrite matrix, where increasing martensite content increase the strength of the steel, at the expense of ductility. However, DP steels are susceptible to hydrogen embrittlement, lowering the ductility, causing significant safety concerns.

2. Multiple heat treatment routes for DP steels have been developed, all involving intercritical annealing. The annealing temperature rather than time has a greater influence on the final

martensite content of the steel, and martensite content increases with increasing intercritical annealing temperature.

3. Critical transformation temperatures must be determined to obtain the intercritical region for annealing. In literature, these are primarily found using equations or computational software. However, dilatometry gives a more accurate characterization of phase transformation in a steel, although this is not found in any relevant literature.

4. Martensite contents from 18.5 % to 96.3 % were obtained through varying the annealing temperature from the lower to the upper bounds of the intercritical region. At higher martensite contents, a continuous network of martensite is formed. This has a significant effect on the diffusion of hydrogen in the steel with an initial decrease, followed by a plateauing of the diffusion coefficient.

5. The effect of hydrogen embrittlement of DP steel is primarily influenced by the ferrite/-martensite interface acting as trapping sites. Overall, increasing martensite contents lead to higher hydrogen contents and more embrittlement, due to the presence of more trapping sites in the martensite and a larger interface area. This decreases the diffusion of hydrogen in the steel.

6. Multiple mechanisms for the fracture of metals due to HE have been proposed; HEDE, HELP and AIDE being the most common. The exact nature of the HE fracture mechanism is still debated in literature, where multiple mechanisms are reported with a synergetic effect causing HE induced fracture.

7. Electrochemical charging of hydrogen is more effective than gaseous charging, with considerable more absorbed hydrogen (3.49 wppm vs. 0.24 wppm) charged into the steel. Sodium chloride is a useful electrolyte for hydrogen charging, as it has a neutral pH, rather than the more commonly used alkaline sodium hydroxide and acidic sulfuric acid.

8. Ammonium thiocyanate should replace the more commonly used *thiourea* as a recombination inhibitor. *Thiourea* oxidizes at an OCP of -1650 mV vs. SCE and bubble formation is reported at an OCP of 1.5 V vs. a saturated Ag/AgCl reference electrode, indicating that *thiourea* becomes ineffective as a recombination inhibitor at certain OCP values.

9. TDS allows for the determination of the quantification of the total absorbed hydrogen contents and the investigation of the nature of the traps in the steel microstructure. The time between charging and TDS measurement is a critical factor, as hydrogen desorption begins immediately.

10. SSRT tests are commonly used to characterize the mechanical change due to hydrogen embrittlement. Lowering the strain rate from 10^{-3} s^{-1} to 10^{-4} s^{-1} increases the embrittlement index from 16 % to 43 %. Using strain rates as low as 10^{-6} s^{-1} gives similar diffusion of hydrogen and dislocation movement. For mechanical testing, an in-situ environment ensures no desorption of hydrogen during the test, accurately capturing the HE of the steel. Interrupted SSRT tests, coupled with ex-situ EBSD, can provide further insight into the fracture micromechanisms.

2.5.2 Research Objectives

From the investigated literature, it is evident that there exist clear research gaps in the investigation of the role of heat treatment on the HE of DP steels. Based on these research gaps, the main research objective for this thesis is developed and formulated:

Evaluating the effect of martensite content on the microstructure and the hydrogen embrittlement of dual-phase steel.

To address and answer the main research objective, it is further divided into four clearly defined sub-objectives:

1. Designing and experimentally validating heat treatment profiles with varying intercritical annealing temperature, resulting in distinct martensite phase fractions of 20 %, 50 %, and 80 %.
2. Quantifying the effect of the obtained microstructure on the absorbed hydrogen content and the nature of traps within the microstructure.
3. Determining the change in the static mechanical properties as a result of both heat treatment and HE in an in-situ environment.
4. Identifying the underlying HE fracture micromechanisms.

2.5.3 Approach

To answer the defined research objectives, consisting wholly of experimental work and analysis, the experimental work was divided into two main experimental work sections. The first consisted of dilatometry experiments and microstructural analysis, to investigate the effect of intercritical annealing temperature on the microstructure and martensite content. Based on these results, three different heat treatment routes were defined, with different martensite contents, for the second experimental section. This section involved the investigation of the HE effect on samples with the three different heat treatments, using TDS, SSRT, fractography and interrupted SSRT with EBSD.

3 Materials and Methods

This section describes the procedure and data analysis of all parts of the experimental work done in this thesis. First the specimen preparation techniques from the as-received material, the design of the tensile specimen and the two heat treatment methods are explained. Then the techniques for the characterization of the material throughout the project work is presented. This includes the initial DP1000 material, the determination of the critical transformation temperatures and the microstructural characterization techniques used. Quantifying the hydrogen content with TDS is then described, followed by the characterization of the static mechanical properties of the specimen with and without a hydrogen embrittlement (HE) environment during slow strain-rate testing. The method for evaluating the underlying HE fracture micromechanisms, using fractography and interrupted SSRT is then defined. Finally, an overview of the produced tensile specimen and a flowchart over the various HE tests and characterization techniques done for the dilatometry and tensile specimens are provided for clarity.

3.1 Specimen Preparation Methods

The specimen preparation method includes the dezincing of the as-received material, the design and machining of tensile specimen and the heat treatment of specimens using dilatometry and tensile specimen heat treatment. The heat treatment using dilatometry was to obtain distinct microstructures with varying martensite contents, while the heat treatment of tensile specimen was used for the quantification of the absorbed hydrogen content and the change in the static mechanical properties in a HE environment. While the same heat treatment procedure was applied with the two methods, there were some difference in the heat treatment methodology.

3.1.1 As-Received Material

The as-received material was a 1000 x 1000 mm rolled sheet of DP1000 steel, produced by *Tata Steel Ijmuiden*. All tensile specimens were cut from this sheet, with the tensile specimen length perpendicular to the rolling direction. The composition of the steel, which was obtained in previous works using X-ray fluorescence (XRF) analysis combined with LECO carbon/sulfur melt analysis is given in Table 5.

Table 5: Composition of the DP steel obtain using XRF analysis combined with LECO carbon/-sulfur melt analysis in previous works in wt. %.

Fe	C	Mn	Cr	Si	Al	Nb	Ti	P	S
96.98	0.14	2.15	0.54	0.13	0.02	0.02	0.01	0.01	0.01

The as-received material was coated with a zinc layer to inhibit corrosion, which was removed before cutting and testing of specimens. Dezincing was done by immersing the specimens in a solution of 18.5 % fuming hydrochloric acid (HCl) and 20 g/L hexamethylenetetramine ($(CH_2)_6N_4$) for 30 s. After dezincing, the specimen was rinsed with water and isopropanol, before drying and storing in a desiccator.

3.1.2 Tensile Specimen Design

The preparation of double-necked tensile specimens was done in multiple stages, as schematically described in Figure 15. First rectangles measuring 134 *mm* by 24 *mm* were cut using a metal shearing machine. These were then laser-cut into a single-neck tensile specimen using a *Lion Laser LionAlpha Metal* laser cutting machine. The single-neck tensile specimens were heat treated to obtain a specific martensite content, the process of which is described in Section 3.1.4. The heat treated specimens were sanded with P400 grit to remove any oxidation layer, remnants of thermocouples and ensure a flat surface. Following this, the heat treated specimens were electrical discharged machined (EDM) with a double-neck in the heat treated region to produce the final tensile specimen. This was to ensure tensile testing occurred in the heat treated area of the tensile sample. These specimens were then used to investigate the HE effect in the heat treated zone using TDS and SSRT testing, described in Sections 3.3 and 3.4 respectively. EDM was conducted by *MF Vonkverspanning B.V.*

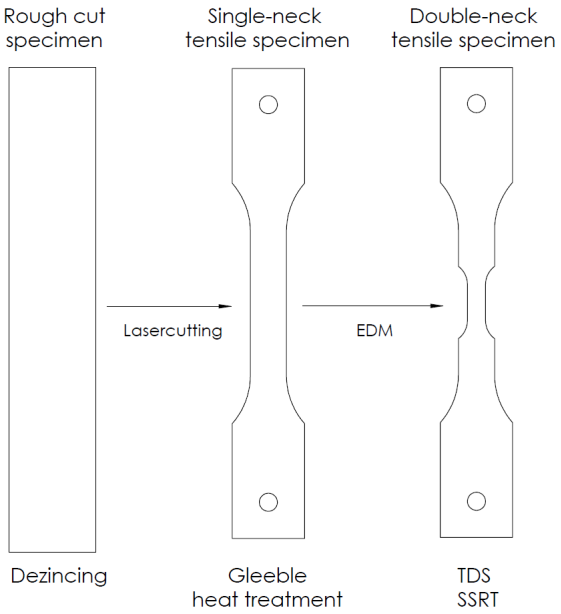

Figure 15: Schematic illustration of the preparation of double-necked tensile specimens from the rough cut from the DP1000 metal sheet.

Engineering drawings of the final double-necked EDM cut specimen are given in Figure 16. For future reference to the orientation of the specimen, a coordinate system is defined for the specimen. The design of tensile specimen were inspired by the ASTM E8/E8M standard [67]. However, due to space limitation in existing tensile grips, all specimen dimensions were reduced in size by 20 %. Furthermore, a 5 *mm* hole was added to the grips of the tensile specimens to allow for clamping during heat treatment.

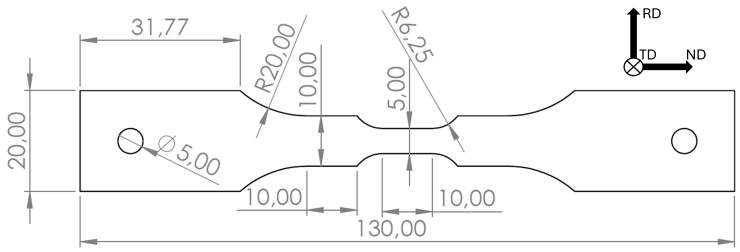

Figure 16: Schematic diagram of the double-necked tensile specimen with all dimensions in *mm*. The rolling (RD), transverse (TD) and normal (ND) directions of the specimen are defined for future reference.

3.1.3 Heat Treatment in Dilatometer

The heat treatment of dilatometry specimens was done using the *Bähr FIL805A/D* quenching and deformation dilatometer, capturing the change in length of the specimen during heating and cooling. Specimens were cut to 4 *mm* length pieces, from tensile specimens with a 10 *mm* gauge width and thickness 1 *mm*. Before dilatometry experiments started, specimens were first sanded with P320 grit SiC sanding paper to remove any oxide layer, and rinsed with isopropanol. The different programmed heat treatment cycles are given in Table 6. Within the A_r temperature range five intercritical annealing temperatures were selected to evaluate the effect of temperature on the martensite content and microstructure. To evaluate the effect of time, three different annealing times were selected for one specific temperature range. After intercritical annealing the specimen was quenched to room temperature using helium gas.

Table 6: Different thermal treatment cycles for the heat treatment of specimens in dilatometry

Heat rate $[°C/s]$	Austenization temp. $[°C]$	Austenization time [min]	Cool rate $[°C/s]$	Annealing temp. $[°C]$	Annealing time [min]
				590	10
				610	10
				630	10
10	900	3	1	650	10
				670	10
				630	5
				630	15

Following the heat treatment of specimen using dilatometry, OM, SEM and EBSD were conducted to estimate the martensite content of the specimens at different intercritical annealing temperatures and times. Hardness measurements were obtained to compare with the heat treated tensile specimens.

3.1.4 Heat Treatment in Gleeble 3800-GTC

The intercritical annealing of tensile specimens occurred in a (*DSI*) *Gleeble 3800-GTC* thermo-mechanical simulator, hereafter only called Gleeble. This method was chosen from multiple alternatives, which are compared in Appendix B. In comparison with the heat treatment using dilato-

metry, only three intercritical annealing temperatures were chosen (590°C, 630°C, and 670°C). The same heating and cooling rates, and holding time as used with dilatometry were applied. The selected intercritical annealing temperatures were chosen to result in a low, equal, and high martensite to ferrite content.

For initial trial specimens, three thermocouples were placed on the specimen, in the center of the specimen, 5 mm from the center of the specimen and 10 mm from the center of the specimen. For the specimens prepared for TDS and SSRT testing, only one thermocouple was welded in the center, to control the temperature development during the annealing. The specimen was then threaded on the holding clamps, which were placed into the Gleeble and tightened, see Figure 17. The heat treatment was initiated once the chamber pressure reached below $4.8 \cdot 10^{-1}$ $torr$. The controlling program is given in Table 7.

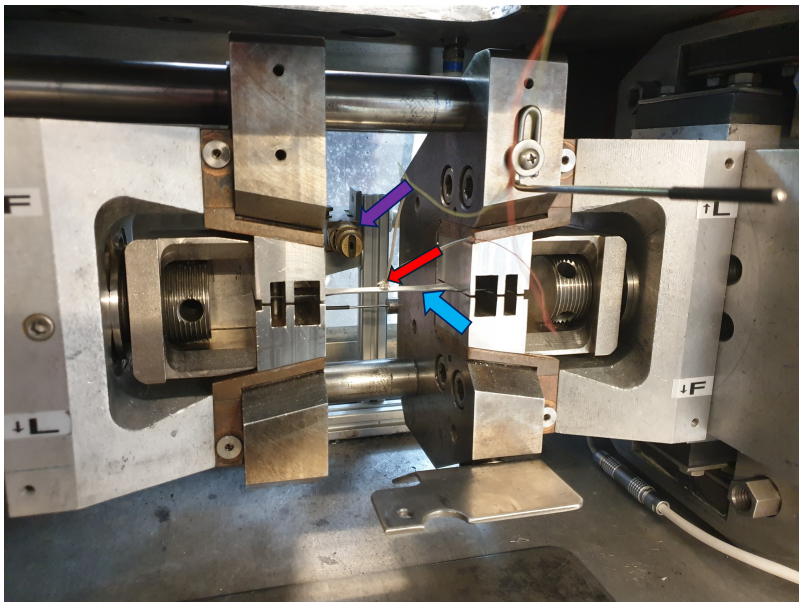

Figure 17: Holding and clamping tensile specimen in the Gleeble. The image shows the holding clamps, holding the specimen (blue arrow) in place, the thermocouple (red arrow) welded to the center of the specimen, and the air quenching nozzle (purple arrow) in the back, facing the specimen.

Table 7: Programmed heat treatment procedure for the Gleeble. The force was kept constant, allowing for thermal expansion of the specimen during the heat treatment.

Step	Force [kN]	Time [min:sec]	Temperature [°C]	Comment
1	0.5	00:10	20	Initiation
2	0.5	01:28	900	10 °C/s heating rate
3	0.5	03:00	900	Austenization
4	0.5	05:10	590	1 °C/s cooling rate
	0.5	04:30	630	
	0.5	03:50	670	
5	0.5	10:00	590	Intercritical Annealing
	0.5	10:00	630	
	0.5	10:00	670	
6	0.5	00:01	20	Air Quenching
7	0.0	00:30	20	Finalization

As seen in the table above, after the initiation of the program, all specimens had an identical initial heating and austenization step. The cooling rate was kept constant, same as for dilatometry, at 1 $°C/s$ the desired intercritical annealing temperature. All specimens were held at the intercritical temperature for 10 minutes, before air quenching to room temperature. The air quenching step had a short programmed time, forcing the system to cool down as quick as possible. The finalization step was present to allow the specimen to completely cool down to room temperature and remove the force holding the specimen. The entire heat treatment procedure was conducted with constant force, avoiding the generation of thermal stresses by accommodating thermal expansion. The initiation and finalization steps were present due to the age of the Gleeble (from 1998), to allow for the system to accurately initiate and correctly respond to the programmed heat treatment.

To compare with the specimens heat treated using the dilatometer, the hardness along the tensile specimen length was obtained. This was supported by obtaining images of the microstructure with SEM. Furthermore, hardness values across the width of the specimen were obtained to ensure the same microstructure is present across the double-necked area of the tensile specimens. SEM and hardness measurements were also obtained in the specimen cross-section to compare with the obtained fracture surfaces after SSRT, to evaluate the effect of the rolling of the as-received steel sheet on the specimens.

3.2 Materials Characterization

The characterization of materials includes the determination of the critical transformation temperatures using dilatometry, the microscopical estimation of martensite content and microstructure analysis using SEM, OM and EBSD, and hardness measurements.

3.2.1 Critical Transformation Temperature Determination

The determination of the critical transformation temperatures was done using a *Bähr FIL805A/D* quenching and deformation dilatometer, with the same specimen preparation as described in Section 3.1.3. The heat treatment procedure is summarized in Table 8. To capture all relevant critical transformation temperatures, this included both the slow heating and cooling of the specimen and the slow cooling and rapid quenching of the specimen to room temperature. Furthermore, two different austenization temperatures and times were evaluated. During the dilatometry procedure, helium was used as a quenching gas.

Table 8: Different heat treatment cycles done during dilatometry for the determination of the critical transformation temperatures.

Heat rate $[°C/s]$	Austenization temp. $[°C]$	Austenization time [min]	Cool rate $[°C/s]$
1	1000	1	1
10	1000	1	Quench
10	900	3	1

The obtained dilatometry data was processed using *Python*, estimating the relevant critical transformation temperatures for all specimens. The code used was adapted from [68], and is given in Appendix A. The critical transformation temperatures were estimated using the *offset method*,

where the critical transformation temperature is the point at which the dilatometry curve deviates from the linear path, indicating the start/finish of the occurring phase transformation.

3.2.2 Microstructure Characterization

Before microstructural characterization, all specimens were prepared in the same manner. Specimens were embedded and sanded to P2000 EU SiC grit, before being polished at 3 μm and 1 μm. For EBSD analysis, specimens were additionally polished with OPS. For specimens analyzed in OM and SEM, specimens were etched using a 5 % nital solution for 8 seconds. This made the microstructure of the specimens visible for microscopy, highlighting the difference between the ferrite and martensite phases in the microstructure.

Optical microscopy (OM) was conduced using a *Keyence VHX-7000* digital microscope, where the surface was captured, and the martensite content estimated using the controlling software. All images were taken at a magnification of 2000x, analyzing three locations per specimen.

The martensite content was estimated using the inherent *auto area measurement* function of the controlling software. The brightness of the surface, which was different for the martensite and ferrite phases, acted as a delimiter. The threshold was moved as to only select ferrite grains, brighter than the martensite ones. After automatically determining the ferrite grain, the image was manually examined, eliminating any mismatched grains. Once complete, the ratio of the area of ferrite to the total area was calculated in the software, with the martensite area ratio being calculated manually by subtracting the ferrite area fraction from the total surface area.

Scanning electron microscopy (SEM) images were captured using a *JEOL JST-IT100* compact SEM. For each specimen, three different locations were investigated, with pictures taken at magnifications of 300x, 1000x and 2000x. Contrast and brightness settings were adjusted to obtain images with distinct differences between the martensite and ferrite phases of the sample. Martensite phases were distinctly brighter than the ferrite phase.

Image post-processing to estimate the martensite content was conduced using the *ImageJ* software using SEM images obtained with a 1000x magnification. First, the contrast was adjusted, to further highlight the difference between the ferrite and martensite phases. The threshold was then adjusted, selecting pixels of a certain grayscale, indicative of the martensite phase. The selected pixels were constructed into particles, with single pixel or small identified particles being disregarded as mismatches. Finally, the ratio of particle area to the total area of the image was calculated, estimating the martensite content. Furthermore, the ratio of particle perimeter to the particle area was estimated, as the ratio of the ferrite/martensite interface to the martensite grain area. The average martensite grain size was estimated by measuring the average diameter of 20 randomly selected martensite grains for each investigated location and intercritical annealing condition.

The underlying fracture micromechanisms were investigated with the fractographic analysis of the obtained fracture surfaces with SEM. The entire fracture surface was investigated with magnification 30x and 100x, with selected areas of interest being investigated at magnifications of 1000x and 2000x.

Electron backscatter diffraction (EBSD) measurements were obtained with a *Thermo-Fisher Helios G4 PFIB UXe* Scanning Electron Microscope, equipped with an *EDAX Technology APED* EBSD

system. EBSD images were obtained to estimate the martensite content and investigate strain localization of interrupted SSRT and fractured specimens. To analyze the obtained data, the *EDAX OIM* software was utilized. Specimens were prior to EBSD, after specimen preparation, throughout cleaned and ungassed, removing any OPS residue. The specimen working distance was set to 10 mm, and rotated to 58°. The SEM image, with 2500x magnification, was focused with an accelerating voltage of 15 kV and a current of 6.4 nA. In the EBSD controlling software, the gain was set to 116 with an exposure time of 8 ms. The step size for each scan was set to 0.1 μm. The EBSD scan was then initiated.

In the *EDAX OIM* software, various maps were generated for each specimen. Image quality maps were used to distinguish between ferrite and martensite, by selecting a threshold value for the ferrite and martensite phases. For most specimens, the threshold value was selected at around 58 %. For the specimens intercritically annealed at the lowest temperature (590 $°C$), the threshold value was decreased to around 50 % as higher values resulted in the mismatching of grains. Similarly, for the specimens intercritically annealed at the highest temperature (670 $°C$), the threshold value was increased to around 70 %. In addition to image quality maps, Kernel Average Misorientation (KAM) maps were generated to indicate the local misorientation in the specimen. This indicated the extent of strain in the crystal structure. For all specimens the KAM maps were generated using the 1st nearest neighbor.

Hardness measurements were conducted using a *Struers Durascan* microhardness tester. HV1 hardness was selected, with an automatic magnification of 20x. Test points were defined across the specimen, at 1 mm intervals. Once the results were obtained, all indents were manually checked to ensure accurate Vickers hardness values were obtained.

3.3 Thermal Desorption Spectroscopy

The measurement of the hydrogen absorption of specimens with thermal desorption spectroscopy (TDS) involved two mains steps, hydrogen charging and hydrogen measuring. Hydrogen charging was conduced using a 3.5% $NaCl$ + 3 g/L ammonium thiocyanate (NH_4SCN) charging solution. A concentration of 3.5% $NaCl$ was chosen to provide a high conductivity with a neutral solution, making the decomposition of water occur at a low voltage, providing H^+ ions for the hydrogen adsorption. Furthermore, it is often used in corrosion research as it resembles seawater salt concentrations. 3 g/L ammonium thiocyanate was used as it has been shown in research as an effective recombination inhibitor.

Charging was done using an electrochemical cell, where the specimen acted as the working electrode. A *BioLogic VSP-300* potentiostat was utilized, using *Chronopotentiometry*, a current controlled electrochemical process, avoiding the need for an external reference electrode. The working electrode was attached to the specimen, while the counter and reference electrodes were attached to an inert platinum electrode. A current density of 1 mA/cm^2 was applied, coinciding with other research. Specimens were charged for two hours, immediately before TDS measurements. The charging time started when the bubbles surrounding the specimens were visually observed, indicating the start of hydrogen formation. The long charging time was to ensure complete saturation of H in the specimen, based on previous research. This coincided with a stable recorded voltage between -1.5 V and -1.6 V. One batch of charging solution were used for three TDS specimen measurements before being discarded in dedicated waste containers.

The total hydrogen content was measured by completely melting the specimen in a carbon crucible within an electrode furnace of a *Bruker G8 Galileo + IR oven* device with N_2 acting as a carrier gas. The electrode furnace is given in Figure 18, and was used due to a small specimen size. First, the TDS specimens were cut from tensile specimens, resulting in rectangular specimens measuring 8 mm by 5 mm from the double-necked area, and charged. Once charging was completed, the specimen was removed from the charging cell, and cleaned using distilled water and isopropanol, before being dried with compressed air. The specimen was weighed, placed in a holding chamber above the electrode furnace, and the TDS device was initiated. A power fraction of 40 % was applied, reaching a temperature of about 1800 $°C$, melting the specimen and releasing all absorbed hydrogen. The high power fraction and crucible temperature, resulted in the rapid and complete melting of the specimens, while allowing all the hydrogen gas to escape the crucible (not being trapped in the liquid steel) and to be detected in the mass spectrometer. For all specimens, a start delay of 20 s and start compensation of 15 s was applied to heat up the carbon crucible and burn any residue. This was followed by the specimen insertion from the holding chamber to the graphite crucible and an analysis duration of 100 s. The measurement was completed with an end compensation of 10 s and a 20 s cooling time. During the TDS measurement, the hydrogen desorption rate was measured as a function of time. After the measurement was completed, the specimen was removed from the electrode furnace. The obtained data was analyzed using python, with the relevant used code given in Appendix A. In the python code, the total hydrogen content was found as the area under the desorption curve.

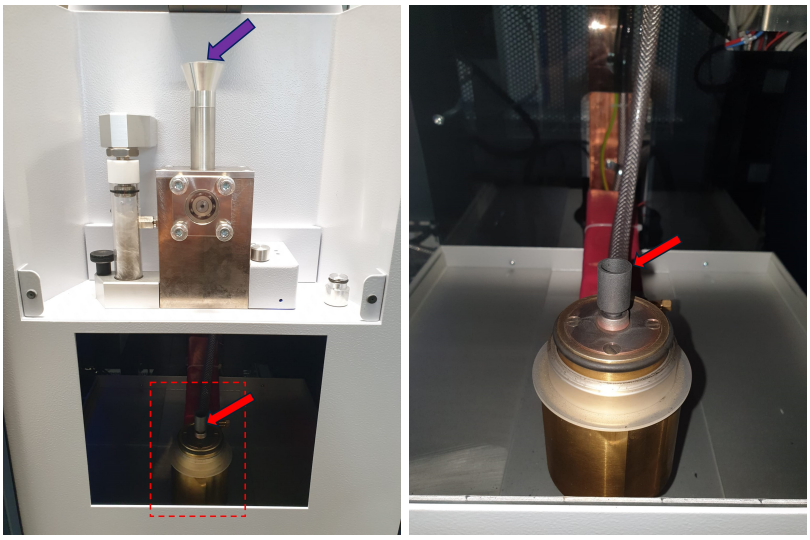

(a) (b)

Figure 18: Images of the electrode oven used in the *Bruker G8 Galileo + IR oven* device for TDS measurements. a) shows the entire setup, while the red box magnified in b) shows inside the oven chamber, with the graphite crucible (red arrow). The purple arrow indicates where the specimen was inserted.

3.4 Slow Strain-Rate Tensile Testing

The mechanical testing of tensile specimen included the slow strain-rate tensile (SSRT) testing and comparison of tensile specimen in an ambient and in an HE environment. Testing was done according to *ASTM G129-21*, the *Standard Practice for Slow Strain Rate Testing to Evaluate the Susceptibility of Metallic Materials to Environmentally Assisted Cracking* [60]. First, benchmark-

ing experiments were done to characterize the unaffected mechanical properties of the material. Then the HE environment was introduced, and HE testing occurred. After these tests data post-processing of the obtained curves was done, alongside fractographic analysis of the fracture surface. For both benchmarking and HE tests three successful specimen experiments were used in the estimation of the embrittlement effect. Finally, interrupted SSRT was conducted by straining to a specific strain for EBSD measurements.

Benchmarking and HE testing of the mechanical properties of tensile specimens was conducted with a *Zwick Roell Z100* tensile testing machine. The tensile setup consisted of a 100 kN load-cell, with the specimen gripped with custom-made grips. The custom-made grips were used for both benchmarking and HE environment in-situ testing. These were developed and used in previous research to provide an insulating layer between the specimen and the rest of the machine, allowing the electrochemical charging of the specimen alone. The grips consisted of aluminum grip holding rods, which held the outer stainless steel grip sleeves. Between the outer stainless steel grip sleeves and the specimens, a kepton tape layer, a *Formlabs rigid resin* grip holder and the final stainless steel grip piece painted with metal protective paint was present. The final stainless steel grip piece was painted with *Parkside* charcoal metal protective paint applied according to producer specifications. The specimen was kept in place with another *rigid resin* piece, which was held by a steel arm barrier, fastened with steel screws.

Benchmarking of mechanical properties

Tensile specimens were first manually sanded in the gauge area with grit P1200 SiC sand paper, to remove EDM residue and any remaining residue from the heat treatment. Then, the dimensions of the double-necked gauge were measured with an electronic caliper, and the specimen placed into the grips of the machine, see Figure 19a. For the benchmarking specimens, a *Zwick Roell* digital clip-on extensometer was placed on the specimen. This was to distinguish between the strain in the specimen and the nominal strain of the tensile tester. The extensometer had a modified (reduced) gauge width of 9.88 mm, to fit within the double-necked gauge, see Figure 19b. During benchmarking testing, a crosshead movement rate of 5.625 mm/hr was applied to the double-necked gauge (gauge-length of 10 mm). This corresponds to a strain $1.563 \cdot 10^{-4}\ s^{-1}$, five times higher than the strain rate for HE environment testing. The increased strain rate was chosen to reduce testing time, while negating any significant effect of increased strain rate on the tensile properties. Furthermore, the strain-rate remained in the region of slow strain-rate testing determined by the *ASTM G129-21* standard. During the tensile benchmarking tests, the engineering (extensometer) and nominal strains were measured as a function of applied force.

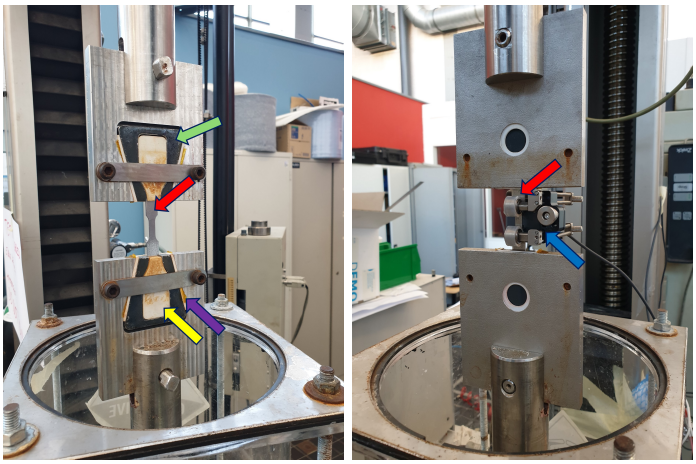

(a) (b)

Figure 19: Images of the tensile specimens (red arrow), a) clamped in the tensile tester with the custom grips (the outer stainless steel grip sleeve, the polymer insulating layer (purple and yellow arrows) and the painted inner stainless steel grips (green arrow)), and b) showing the extenosmeter (blue) placed across the double-necked gauge of the specimen.

Hydrogen Embrittlement Testing

For the SSRT testing in a HE environment an electrochemical bath was present to hold the charging solution, in addition to the same equipment used for the benchmarking SSRT described above. The used SSRT setup for HE testing is seen in Figure 20. After the sanding, measuring and mounting of the specimen in the grips, electrochemical wires were attached to the specimen and the Pt counter electrode was placed close to the specimen. The charging solution bath was raised to submerge the specimen. An aquarium heater was placed in the bath, ensuring a constant testing temperature of 25 $°C$. This was done as the ambient temperature varied greatly with changing seasons, having a possible influence on the HE effect. The charging conditions were the same as applied to TDS specimen, described in Section 3.3.

After the two hour pre-charging, SSRT testing was commenced with a crosshead movement rate of 1.125 mm/hr, corresponding to a strain of $3.125 \cdot 10^{-5}$ s^{-1}. The strain rate was selected as it is within the ranges given by *ASTM G129-21*. Furthermore, it coincided with previous works, being low enough to encourage the diffusion of hydrogen, with strain rates in the same order of magnitude seen in other research. Since the specimens were submerged in a bath, an extensometer could not be utilized, and during the measurement the nominal strain was measured as a function of force. Following the fracture of the specimens, the specimens were carefully removed, rinsed with distilled water and isopropanol, and dried before storing in a desiccator. Fractography of the fracture surface was done using SEM, and the strain localization close to the fracture edge was analyzed with EBSD with the preparation procedure described in Section 3.4.1.

During the benchmarking experiments, both the engineering (only specimen gauge) and the nominal (entire tensile tester) stress-strain curves were captured. For the case of HE testing, as no submersible extensometer was available, only the nominal stress-strain curves were obtained. During post-processing of the obtained data, a method was developed to account for the elongation of the tensile tester and estimate the engineering stress-strain curve of the heat-treated region of the specimens in HE conditions. This method, with the python code shown in Appendix A, was based

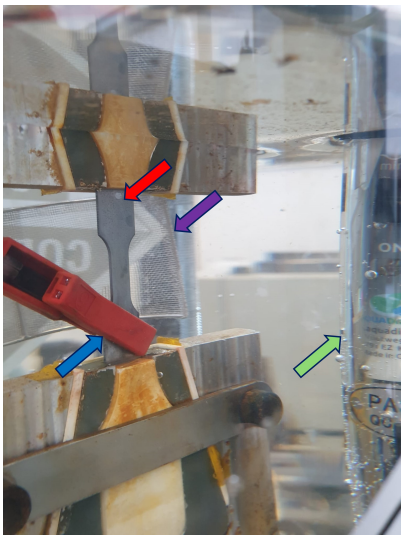

Figure 20: Image showing the setup for SSRT in a HE aqueous environment. The working electrode (blue arrow) is attached to the specimen (red arrow), completely submerged in the charging solution. The green and purple arrows indicates the heating element, and the Pt counter-electrode respectively.

on a similar method used in other research. The underlying principle was that the loading system of the tensile machine could be seen as two springs in series, one being the tensile tester and the other the specimen. The deformation in the tensile tester was assumed constant, and not dependent on the specimen conditions. The nominal strain, was therefore the sum of the deformation in the load train and the specimen. In the elastic region, the load-train displacement could be found by subtracting the engineering strain from the nominal strain. The load-train displacement as a function of force was plotted and a third order polynomial trend line was fitted. The trend line was found based on the average benchmarking specimen data for each of the different intercritical annealing temperature conditions.

For the HE affected tensile specimen, the load-train displacement curve was reconstructed based on the recorded force. The load-train displacement curve was then subtracted from the nominal strain curve, giving an estimated HE engineering tensile curve. Furthermore, it was observed that there was some deviation between the nominal engineering stress-strain curves of the benchmarking and HE specimen. This resulted from hysteresis in the load-train, as a result of the *rigid resin* and painted parts of the tensile setup. As this impacts the estimated HE engineering stress-strain curve, the difference between the benchmarking and HE nominal engineering stress-strain curves was found. This difference was then applied to the estimated HE engineering stress-strain curve.

3.4.1 Interrupted SSRT with EBSD

Interrupted SSRT was conducted to investigate the strain localization during deformation in a HE environment. This was accomplished by stopping the tensile test once a nominal strain reached 12.5 % in the in-situ HE environment. This value was selected to provide plastic deformation of the specimen, without going to fracture, based on the results obtained during benchmarking and HE environment SSRT. One specimen for each of the intercritical annealing conditions (590 $^{\circ}C$, 630 $^{\circ}C$, and 670 $^{\circ}C$) was investigated in an HE environment. Once the correct strain was achieved, the specimen was carefully removed from the tensile tester. The edges of the specimen were cut

off, leaving only an area of the double-necked gauge. The double-necked gauge was embedded, and the specimen carefully sanded with grit P1200 and P2000 to remove the surface layer. Following this the specimen was extensively polished with 3 μm and 1 μm particles. Finally, the specimen was polished with OPS, before being cleaned in isopropanol in an ultrasonic bath, and placed in vacuum to remove any remaining OPS residue.

EBSD was conducted with the same equipment and EBSD conditions as described in Section 3.2.2, except an applied step size of 0.07 μm instead of 0.1 μm. This was done to obtain a better resolution in the ferrite/martensite interface.

3.5 Overview of Specimen Tests

Table 9 shows the testing matrix for the testing with tensile specimens. 75 samples were produced in total, 25 for each intercritical annealing temperature. The calibration included calibrating the tensile testing setup and test speed, as well as the initial testing for the TDS measurements.

Table 9: Overview of specimens needed to complete planned experiments

Test	Sub-test	590°C	630°C	670°C	Comment
Microstructure Analysis		2	2	2	SEM and Hardness
TDS		3	3	3	Total hydrogen content
SSRT	Benchmarking HE environment	3 3	3 3	3 3	Ambient environment In-situ aqueous charging
Interrupted SSRT		1	1	1	In HE environment for EBSD analysis
Calibration		3	3	3	Tensile and TDS calibration
Additional		10	10	10	Extra specimen
Total		25	25	25	75 Samples in total

An overview of the various test and analysis techniques used for the dilatometry and tensile specimen is given in Figure 21, to provide clarity of the experimental work done during the duration of the thesis project.

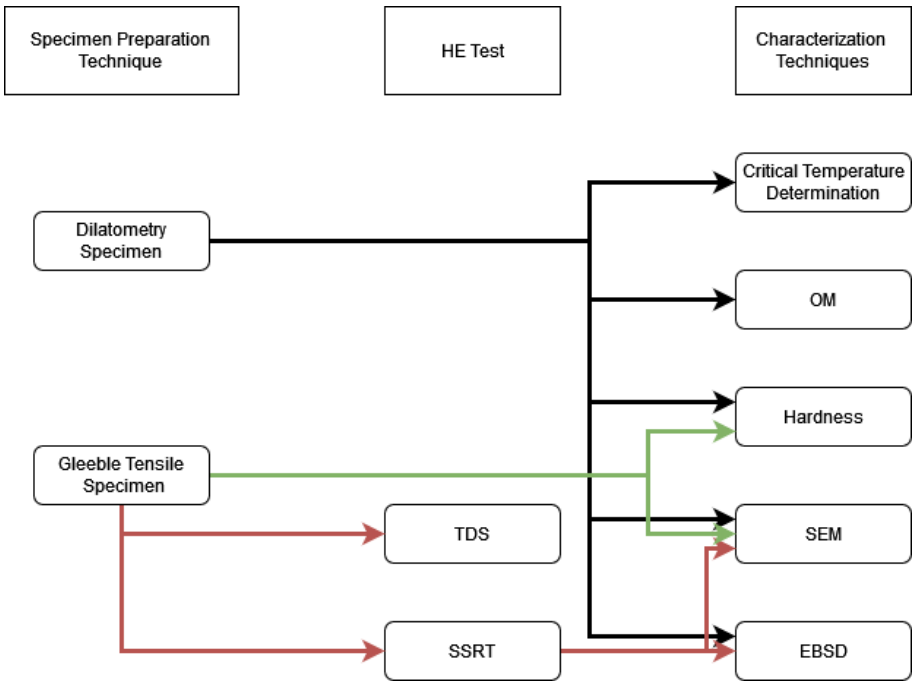

Figure 21: Flowchart of the various HE tests and characterization techniques conducted on dilatometry and Gleeble tensile specimens, during the project work.

4 Results and Discussions

This section presents and discusses the results from the different experiments done in this thesis project. First the determined critical transformation temperatures are shown, before the quantitative and qualitative characterization of the obtained microstructure from the dilatometry heat treatments, comparing them with the as-received material, the tensile specimens heat treated in the Gleeble and microstructures obtained in literature. Following this, the absorbed hydrogen content for the different intercritical annealing conditions is presented, measured with TDS. The change in the static mechanical properties is then given, for the different intercritical annealing conditions in an HE environment. An overview of all quantified results are then given in Section 4.5 for clarity and ease of comparison. Finally, the investigation of the underlying fracture micromechanisms, investigated with fractography and EBSD of interrupted SSRT and fractured specimen is presented and discussed. Due to the volume of significant results obtained during this thesis project, only the main results are presented in this section. Supplementary figures and tables are presented in the appendices. These will be referenced where relevant.

4.1 Determination of Critical Transformation Temperatures

Figure 22 shows the dilatometry curves obtained to determine the critical transformation temperatures, with the heat treatment profile defined in Table 8. An example for the determination of each individual critical transformation temperature of a specific curve is given in Appendix C. Furthermore, the appendix shows the identified critical transformation temperatures for all specimens not shown in this section, but contribute to the critical transformation temperatures given in Table 10.

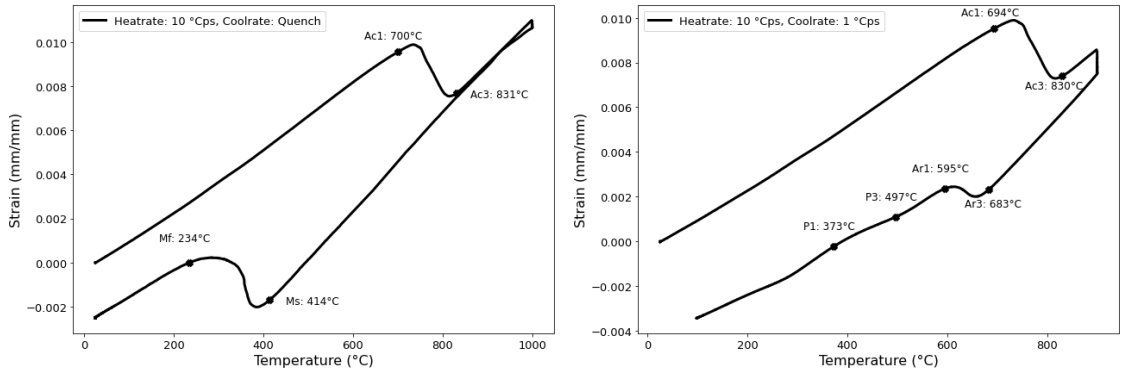

(a) (b)

Figure 22: Dilatometry curves showing the strain of the sample as a function of temperature indicating the critical transformation temperatures of the material.

For all samples, the A_c critical transformation temperatures remain almost identical, indicating that there is a negligible effect of varying heating rate (10 $°C/s$ or 1 $°C/s$ or) on the start and end of the critical transformation temperatures during heating. However, with increasing austenization temperature, there is a downward shift in the A_r critical transformation temperatures. For the specimen with a slow cooling rate (1 $°C/s$) (Figure 22b) two different phase transformations are present. The first necking of the curve is the ferrite formation range, while the second indicated the formation of pearlite in the specimen. At an austenization temperature of 1000 $°C$ there is

an overlap between the first and second neck in the cooling curve, seen in Appendix C. Due to this, it is not possible to accurately determine the end of the ferrite formation reaction and the start of the pearlite formation temperatures. As pearlite should not be present in the final DP microstructure, this overlap is unwanted. By decreasing the austenization temperature from 1000 $°C$ to 900 $°C$ there is a distinguishable increase in the A_r region, being separated from the pearlite formation region. Increasing the austenization temperature creates larger and more stable austenite grains, which required a higher undercooling before the ferrite formation (A_r3) begins. In Figure 22a, the martensite formation is captured, indicating the M_s and M_f temperatures. The martensite formation range is distinguishably lower than the A_r, while the M_f temperature (243 $°C$) remains much higher than room temperature. This indicates that during the quenching to room temperature of subsequent heat treatments, the undercooling is sufficient that all remaining austenite is transformed to martensite, creating the DP microstructure.

In addition to determining the critical transformation temperatures using the heat treatment profiles in Table 8, some critical transformation temperatures are found during the heat treatment of the specimen with dilatometry. The specific dilatometry curves are given in Appendix C. The relevant transformation temperatures across all dilatometry specimens are summarized in Table 10.

Table 10: Critical transformation temperatures [$°C$] determined from the dilatometry specimens with different austenization temperatures and time, with standard deviation. N/A: Critical transformation temperature not found.

	A_c1	A_c3	A_r3	A_r1	M_s	M_f
	900 $°C$, 3 min					
Avg.	707	828	686	571	333	188
σ	8	2	1	10	32	12
	1000 $°C$, 1 min					
Avg.	702	830	661	N/A	405	208
σ	2	2	0	N/A	14	26

As austenization temperature decreases, with increasing austenization time, the A_c range remains stable, while the A_r range increases slightly. Furthermore, there is a decrease in the M_s and M_f indicating the martensite formation starts and ends at a lower temperature. The A_r intercritical range is most relevant for the intercritical annealing of dilatometry and tensile specimens, with an austenization temperature of 900$°C$ for 3 min. A_r3, the start of the ferrite formation is found to be 686 ± 1 $°C$, while A_r1, the end of the ferrite forming reaction is found to be 571 ± 10 $°C$. To stay within this range during the heat treatment of dilatometry and tensile specimen, accounting for the standard deviation, the highest intercritical annealing temperature is chosen at 670 $°C$, and the lowest at 590 $°C$, to obtain distinct martensite contents.

As mentioned in Section 2.1.2, the use of dilatometry to determine the critical transformation temperatures for heat treatment of DP steels is extremely limited. All investigated literature use either Thermo-calc or Andrews' equations. However, these methods are limited in their accuracy and extent of critical transformation temperatures obtained. Dilatometry, however, is shown to be a quick and versatile method in accurately determining the relevant critical transformation temperatures to develop heat treatments for DP steels. With two dilatometry experiments all relevant critical transformation temperatures, the A_c, A_r, M_s and M_f temperatures are found for a specific steel.

During heat treatments with the dilatometry at varying intercritical annealing temperatures, it

is possible to qualitative assess the obtained martensite content. As seen in Figure 23, there is a distinct decrease in the intensity of the deviation in the curve between M_s and M_f when the intercritical annealing temperature increases from 590 $°C$ to 670 $°C$. This indicates more martensite is transformed, causing a greater shift in the strain of the specimen. While this gives dilatometry an added value in the characterization of development of heat treatments to produce a DP microstructure, quantification of obtained martensite content through heat treatment with dilatometry must be done using other techniques.

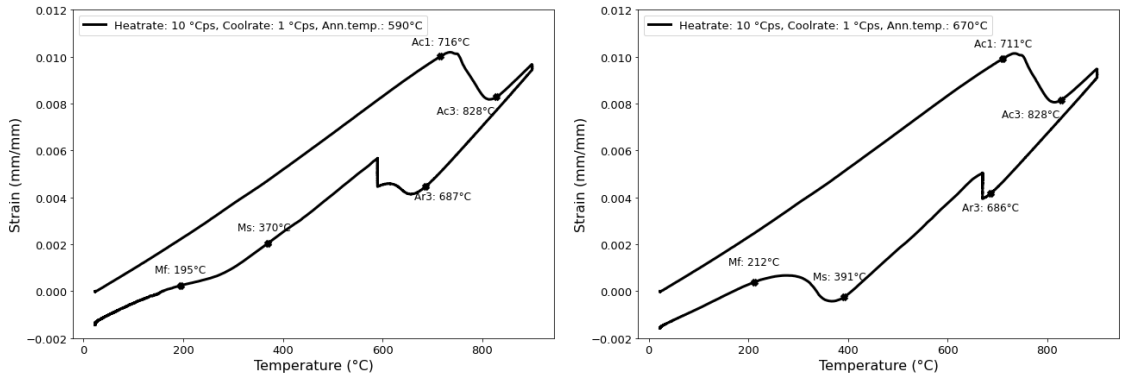

(a) (b)

Figure 23: Dilatometry curves for the specimens heat treated with dilatometry, at intercritical annealing temperature of a) 590 $°C$ and b) 670 $°C$, showing the identified critical transformation temperatures and change in martensite formation slope.

4.2 Microstructure Characterization

The microstructure characterization includes the quantification of the martensite content for the different intercritical annealing conditions, the qualitative investigation of the microstructure of the specimen, and the comparative analysis of dilatometry and Gleeble tensile specimen.

4.2.1 Quantification of Martensite Content

The martensite content for the heat treatment of different intercritical annealing temperatures was estimated using SEM, OM and EBSD. Figure 24 shows examples of the estimation of martensite content for the specimens intercritically annealed at the lowest (590 $°C$) and the highest (670 $°C$) temperatures, showing the clear difference in martensite content for all three characterization techniques. For the specimen intercritically annealed at other temperatures, the estimation images are given in Appendix D. For all specimens three locations (two for EBSD) were investigated, with one representative image being presented per specimen for all characterization methods.

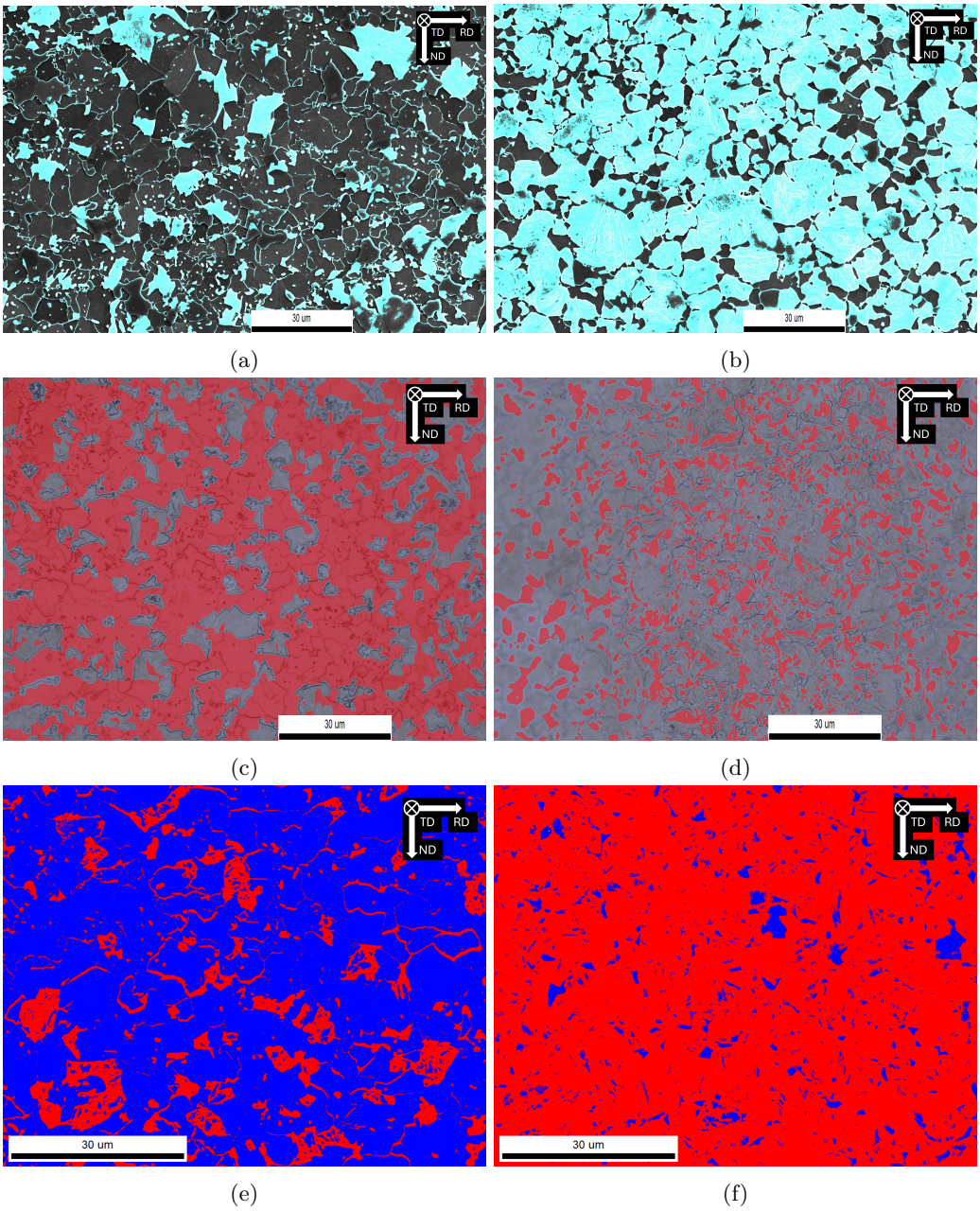

Figure 24: Estimated martensite content for dilatometry specimens intercritical annealed at a), c), e) 590 $°C$ and b), d), f) 670 $°C$ using a), b) SEM, c), d) OM, and e), f) EBSD. For SEM martensite is depicted as the cyan phase, while in OM the ferrite phase is depicted as red. For EBSD, the red phase indicates martensite, while the blue indicate ferrite.

In the comparison between the specimens intercritically annealed at the lowest and highest temperature, there is a clear contrast in the estimated martensite content. This indicates that as the intercritical annealing temperature increases, so does the martensite content. Less ferrite is formed at higher temperatures and more austenite remains after the intercritical annealing, which is transformed to martensite during quenching. The estimated martensite content for each of the different characterization techniques with increasing intercritical annealing temperature, as well as the average across all techniques is given in Table 11. The total estimated martensite content is plotted against the intercritical annealing temperature in Figure 25.

Table 11: Estimated martensite content (in volume %) depending on the microscopy technique for specimens with different intercritical annealing temperatures (Temp.).

	OM		SEM		EBSD		Total	
Temp. [$°C$]	Avg.	σ	Avg.	σ	Avg.	σ	Avg.	σ
590	25	5	23	1	29	10	25	5
610	50	4	45	6	55	7	49	7
630	51	1	48	3	53	6	50	4
650	65	4	66	2	64	6	65	4
670	75	3	73	1	88	5	78	7

Based on Table 11 and Figure 25, there is a linear increase in martensite content as the intercritical annealing temperature increases. Martensite contents of 25 ± 5 %, 50 ± 4 % and 78 ± 7 %, are obtained with the annealing at 590 $°C$, 630 $°C$, and 670 $°C$ respectively, which are close to the desired 20 %, 50 % and 80 % martensite contents. It is seen in the table that EBSD estimates martensite contents higher than the average, while SEM estimates lower martensite contents, except for intercritical annealing at 650 $°C$ where EBSD estimates higher than average and SEM lower. OM is between the EBSD and SEM and thus becomes closest with the total average. Additionally, there is a greater standard deviation and spread for areas estimated with EBSD than those of OM and SEM. The total standard deviation remains similar for all specimens, indicating that the investigated areas have similar ferrite and martensite contents.

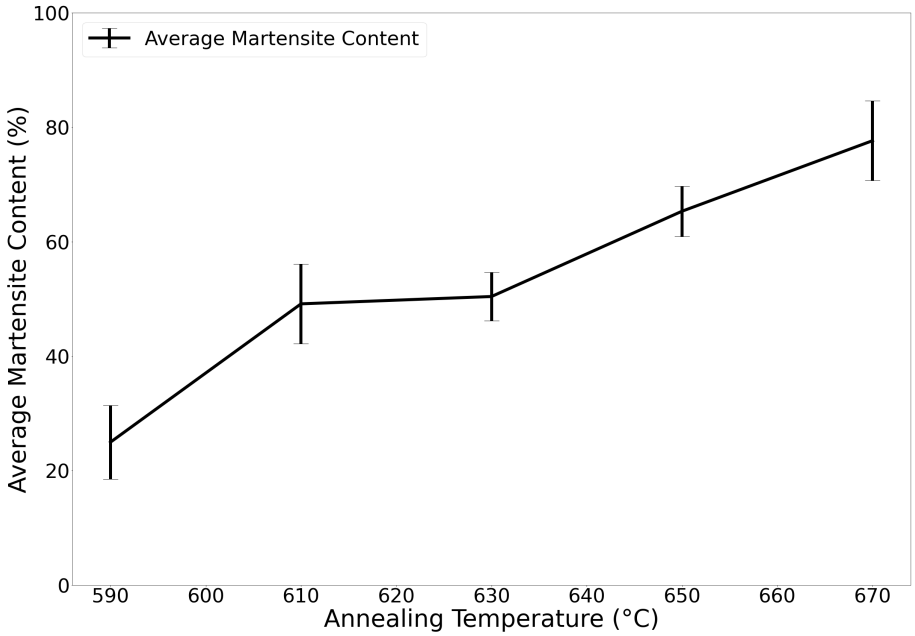

Figure 25: Martensite content development with increasing annealing temperatures, investigated with OM, SEM and EBSD.

The effect of intercritical annealing time on the martensite content is given in Figure 26, quantified for each specimen and characterization technique in Table 12. In the figure, there is a small decrease in martensite content with an increase in intercritical annealing time from 5 to 10 minutes. Increasing the intercritical annealing time does not significantly change the intercritical annealing time, as it is within the standard deviation of 10 minutes.

Table 12: Estimated martensite content (in volume %) depending on the microscopy technique for specimens with different intercritical annealing times. N/A: specimens were not tested with EBSD.

	OM		SEM		EBSD		Total	
Time $[min]$	Avg.	σ	Avg.	σ	Avg.	σ	Avg.	σ
5	58	2	52	9	N/A	N/A	55	7
10	45	2	40	7	N/A	N/A	42	5
15	51	1	48	3	53	6.	50	4

Comparing the SEM and OM values in Table 12 show that OM results in a higher estimated martensite content than SEM, for all specimens. Furthermore, the standard deviation for SEM is significantly higher than for OM, indicating a larger spread and variance in the investigated areas. As intercritical annealing time increases the standard deviation decreases, indicating the investigated areas becoming more similar with longer annealing times.

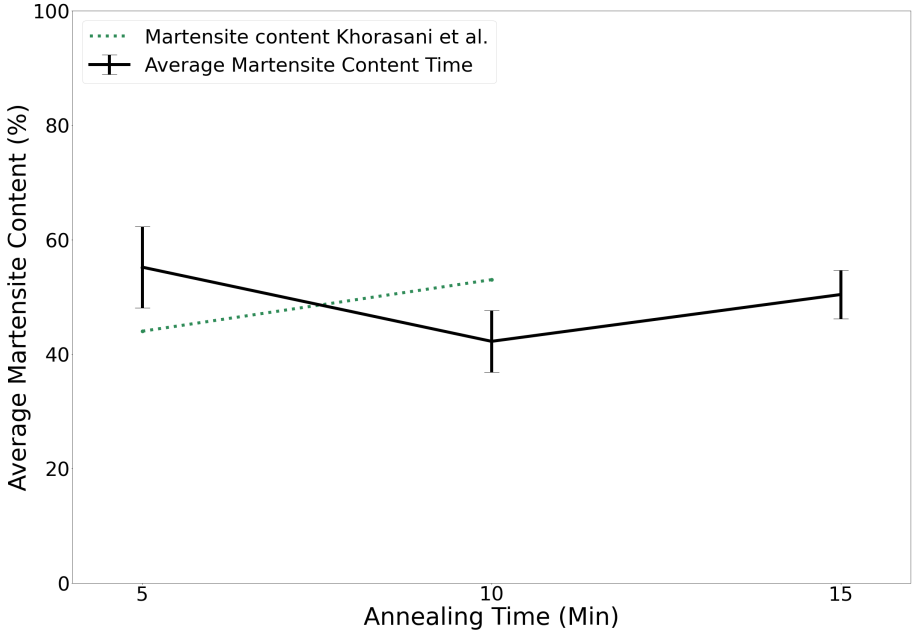

Figure 26: Estimated martensite content at annealing temperature of 630 $°C$ for 5, 10 and 15 min, compared to the result obtained for Khorasani et al [20].

As intercritical annealing using the A_r temperature range is not common in literature, the comparison of obtained martensite contents becomes limited. However, comparison to the martensite contents obtained using intercritical annealing in the A_c range is possible. Within the A_c and A_r ranges there is respectively the formation of austenite from ferrite and the formation of ferrite from austenite. It follows for both that at higher intercritical annealing temperature more austenite is present, which during quenching becomes martensite. Comparing to the results of Wang et al. (2020), intercritical annealing at the lower and upper critical transformation temperatures result in a very low and high martensite content respectively [23]. However, this intercritical annealing changes the as-received material, and does not include austenitization to create a new DP microstructure. Therefore, it can be assumed the obtained martensite content in Wang et al. (2020) depend heavily on the as-received martensite content.

Comparing the effect of time with that obtained by Khorasani et al., the opposite effect is found,

as seen in Figure 26 [20]. With increasing intercritical annealing temperature, Khorasani et al. reports an increase in martensite content, while it is found here to slightly decrease. However, as Khorasani et al. conduct intercritical annealing using the A_c temperatures, this is expected. Since in the A_c range austenite is formed from ferrite, increasing intercritical annealing time allows for more formation of austenite. Oppositely, when using the A_r range, ferrite is formed from austenite, and longer times allow for more ferrite formation, giving lower martensite contents. Furthermore, Khorasani et al. investigates intercritical annealing times as low as one minute, which gives a more extreme short intercritical annealing condition than at five minutes, investigated here. This would explain the greater change in martensite content as time increases. However, as obtained here, Khorasani et al. are unable to create vastly different martensite contents by changing the intercritical annealing time.

Overall, the heat treatments done through dilatometry in the A_r intercritical range, show that with intercritical annealing of 590 $°C$, 630 $°C$ and 670 $°C$, it is possible to obtain a martensite content close to 20 %, 50 %, and 80 %. The effect of time on the martensite content is negligible as it varies little and stabilized after 10 minutes intercritical annealing.

4.2.2 Qualitative Analysis of Microstructure

The qualitative analysis of the dilatometry specimen microstructure aims to investigate and compare the nature of the martensite and ferrite phases within the microstructure of the different annealing conditions. Additionally, it is compared to the microstructure of the as-received steel sheet. Figure 27 shows overview SEM images showing the microstructure of the specimen's intercritical annealed closest to the edges of the A_r region determined from the dilatometry curves. Here it is clear that intercritical annealing at 590 $°C$ close to A_r1 results in much less martensite than intercritical annealing at 670 $°C$, close to the upper A_r3 boundary. Further overview images showing the specimens intercritically annealed at 610 $°C$, 630 $°C$, and 650 $°C$ are seen in Appendix D.

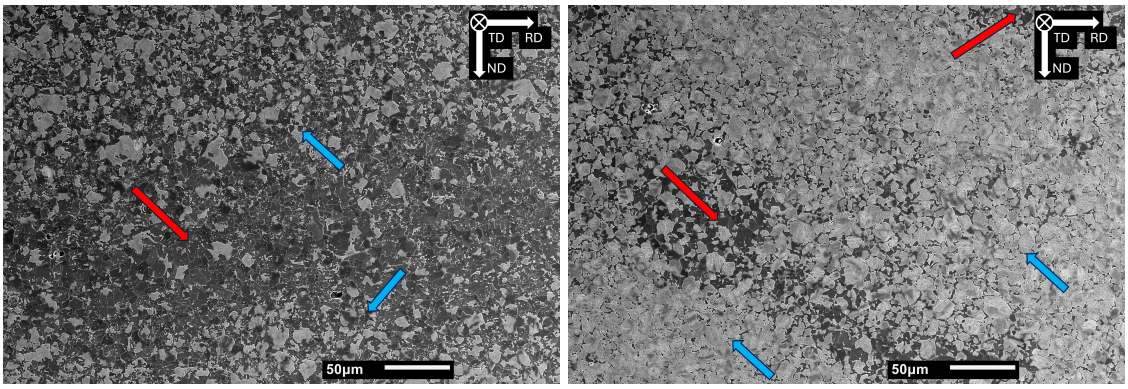

(a) (b)

Figure 27: Overview SEM images at magnification 300x of specimens intercritically annealed at a) 590 $°C$ and b) 670 $°C$. The lighter phase indicates martensite, while the dark phase indicates ferrite. Blue and red arrows indicate regions of high martensite and ferrite content respectively.

As seen in Figure 27 the martensite and ferrite phases are not homogeneously distributed throughout the specimen. Rather, there exist a banding structure consisting of areas of high martensite content (blue arrows) and of high ferrite contents (red arrow). However, for the 590 $°C$ specimen,

more ferrite exist within the martensite band than in the martensite band of the 670 $°C$ specimen. Similarly, the ferrite band of the 670 $°C$ specimen is smaller and contains more martensite than for the 590 specimen. This impacts the estimation of martensite content, as different investigated locations in the specimen can give differences in the obtained martensite phase fraction. However, as seen in Table 11, the estimated martensite content has a low standard deviation indicating a similar structure is obtained at multiple locations on the specimen.

To further investigate the difference in martensite grains and martensite islands (inclusions), SEM images have been captured at 2000x magnification. Figure 28 shows these images at the intercritical annealing temperatures of 590 $°C$ and 670 $°C$, at the lower and upper extremes of the A_r region. In the figure, there is a difference in the martensite grain size, with much larger martensite grains present at 670 $°C$. This is quantified in Table 13. As there is less ferrite forming during the annealing and a higher driving force for martensite formation, due to a higher annealing temperature causing higher undercooling, there is more and larger remaining austenite grains transforming to martensite after annealing. While at 590 $°C$ the martensite grains are smaller, there exist within the ferrite grain martensite islands, which are not present at 670 $°C$. However, the variation in the average grain size remains very large. This is due to many different sized grains present in the microstructure. At higher intercritical annealing temperature larger grains are more prevalent, increasing the average grain size.

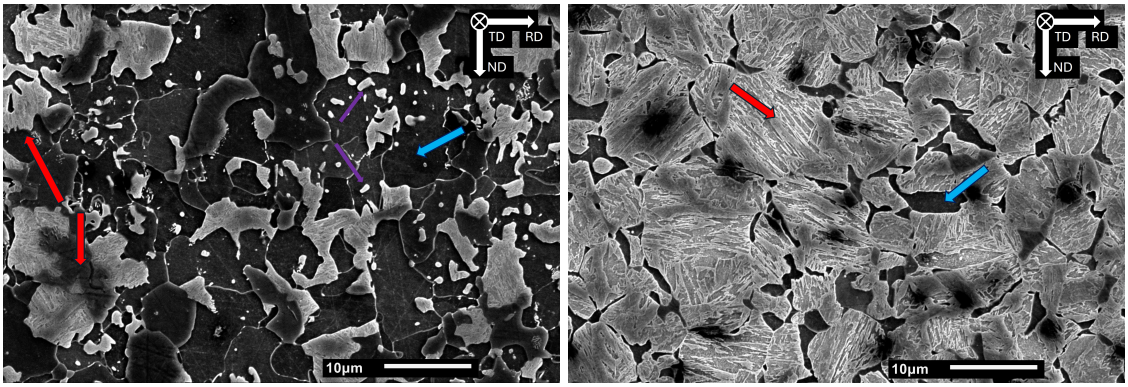

(a) (b)

Figure 28: Close-up SEM images at magnification 2000x of specimens intercritically annealed at a) 590 $°C$ and b) 670 $°C$. The lighter phase indicates martensite, while the dark phase indicates ferrite. Blue, red, and purple arrows indicate regions of high martensite and ferrite content, and martensite islands respectively.

As seen in Figure 28, at an intercritical annealing temperature of 590 $°C$ martensite is distributed in a discontinuous style, broken into singular grains surrounded by ferrite. When the intercritical annealing temperature increases to 670 $°C$ the martensite becomes a continuous network. In both cases the martensite grains are in the form of lath martensite, seen by the substructure lath boundaries within the martensite grains. This type of structure is common with the quenching of low carbon content steel from high temperatures.

Table 13: Average martensite grain size diameter with increasing intercritical annealing temperature, measured from 20 martensite grains in SEM microstructure images.

Annealing Temperature [$°C$]	Avg. martensite grain size (Std.) [μm]
590	3.9 (2.6)
630	5.9 (3.2)
670	7.4 (3.4)

Similar microstructures are found when comparing the obtained microstructure to literature. In the work of Reddy et al., with intercritical annealing a continuous martensite network is formed with larger martensite grains, when compared to the as-received material [18]. Furthermore, in the work of Wang et al. (2020), the martensite goes from a semicontinuous network to a continuous network with increasing martensite contents. The continuous martensite network was present at a martensite content of 68.3 %. Therefore, observing continuous martensite with intercritical annealing at 670 $°C$ with a martensite content of 78 ± 7 % is expected.

Compared to the as-received material, seen in Figure 29, a semicontinuous network is present. The microstructure is finer, with smaller interdispersed ferrite and martensite grains. However, there are locations in the microstructure with higher local ferrite and martensite content similar to what is obtained in dilatometry. Therefore, the as-received microstructure can impact the formation of austenite during austenization. This impacts the formation of ferrite and martensite during intercritical annealing and quenching which gives regions in the microstructure of locally increased ferrite and martensite content. This indicates that the utilized austenization time is insufficient in fully homogenizing the specimens. Since the as-received steel sheet was rolled, the rolling structure is prevalent, influencing the nucleation of austenite and ferrite.

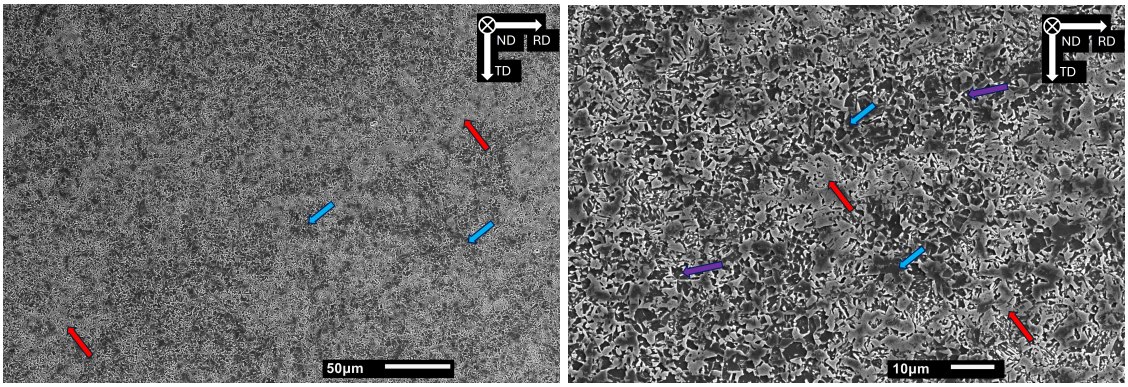

(a) (b)

Figure 29: SEM images of the as-received material, at magnifications of a) 300x and b) 1000x. The martensite grains (red arrows) are depicted with lighter color than the ferrite grains (blue arrows). The purple arrows in b) show some martensite islands identified in the microstructure.

4.2.3 Comparative Analysis of Microstructure

The comparison of the hardness values of the dilatometry and tensile specimens as a function of intercritical annealing temperature is given in Figure 30, and is quantified in Table 14. Furthermore, in the table, the hardness for the as received material is given. The hardness profiles for the different specimens, and SEM images comparing the microstructures of the dilatometry and tensile specimen heat treated in the Gleeble are given in Appendix E. Additional characterization of the tensile specimen heat treated in the Gleeble are given in Appendix F. This includes the temperature development during heat treatment and hardness across the entire specimen gauge outside the heat treated zone.

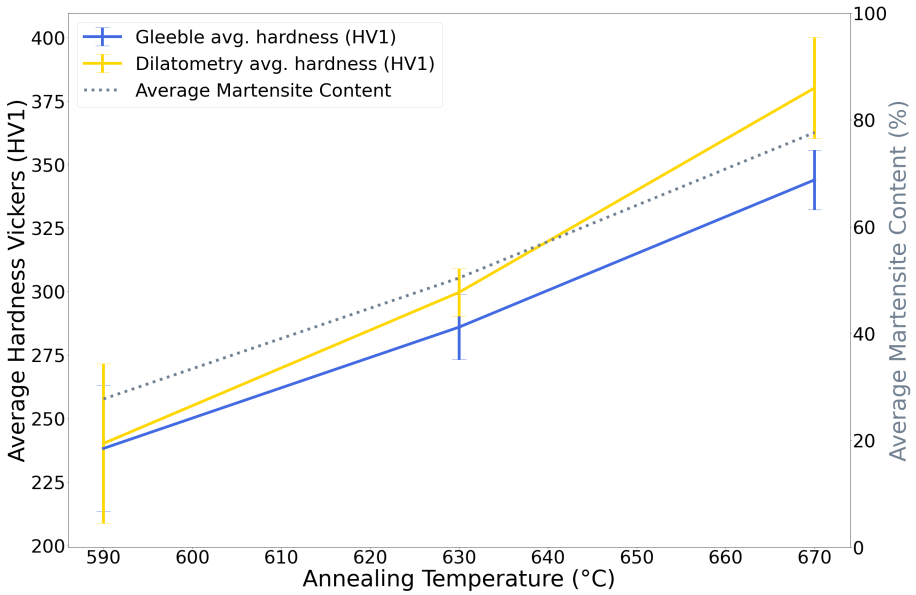

Figure 30: Comparison of the HV1 hardness obtained from specimens heat treated with dilatometry (yellow) and the Gleeble (blue), as a function of intercritical annealing temperature. The dashed line shows the estimated martensite content as a function of intercritical annealing temperature.

Table 14: Comparison of the HV1 hardness (Std.) of the as-received materials and specimens heat treated using dilatometry and the Gleeble.

Annealing Temperature	As-received $[HV1]$	Dilatometry $[HV1]$	Gleeble $[HV1]$
590 $°C$	324 (6)	240 (31)	238 (25)
630 $°C$		300 (9)	286 (13)
670 $°C$		380 (20)	344 (12)

The purpose of the hardness investigation is to provide a quick method for the validation that a microstructure similar to that obtained during dilatometry is obtained when using the Gleeble. The results obtained here, show that although there is a difference in the absolute value of the hardness, the trend and development with temperature remains similar. Differences in heat treatment technique are evident to be more distinct at higher intercritical annealing temperatures. However,

these differences, while unavoidable, have a negligible impact on the subsequent investigation of the HE effect, which primarily relates to the comparison of the different intercritical annealing temperature. As seen with the estimated martensite content trend line, the slope of the curve for both all three curves are similar. This indicates hardness is a good method to quickly estimate the martensite content of an unknown DP steel. To do this, the hardness of a fully ferritic and martensitic material must be known to extrapolate the trend line between them.

4.3 Thermal Desorption Spectroscopy

During TDS the total hydrogen content is measured and quantified. For all specimens one significant peak was obtained during the TDS measurement. An initial increase in the desorbed hydrogen rate was recorded immediately after measurement started. As there is some time between the hydrogen desorption from the specimen and it being detected by the *Bruker G8 Galileo + IR Oven* device ($\sim 30\ s$), the initial increase does not come from the specimen. Rather, the initial increase is a result of the graphite crucible. To estimate the absorbed hydrogen content, the baseline is adjusted accordingly. Appendix G contains the full TDS curves for all specimens and the measured desorption from the crucible alone. Figure 31 show the desorption curves of the significant peak, comparing the intercritical annealing conditions.

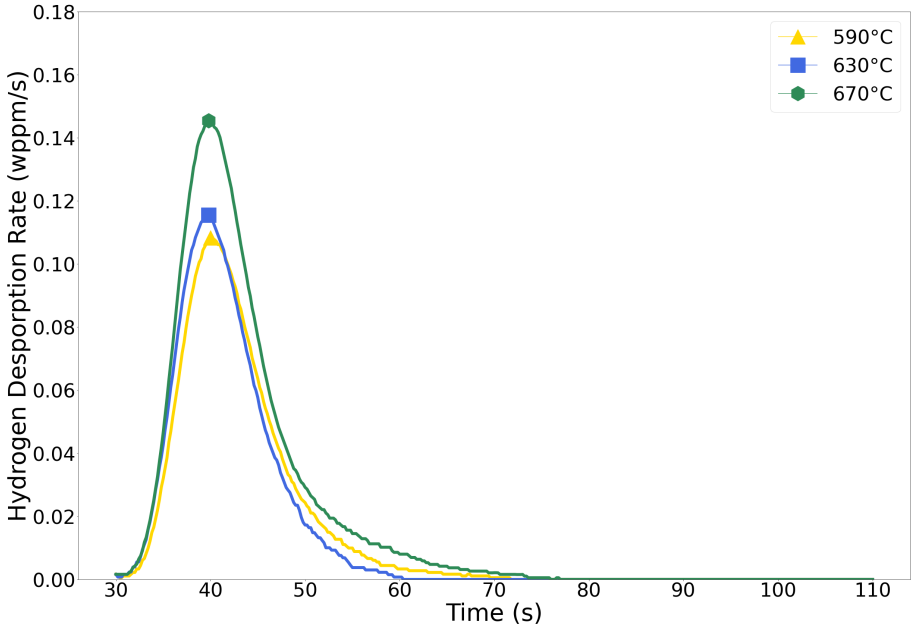

Figure 31: Adapted TDS curves showing the desorbed hydrogen content per second as a function of time for the different intercritical annealing temperatures.

As seen in Figure 31 all curves are similar. Particularly, the 590 $°C$ and 630 $°C$ specimens have similar peaks, although the 630 $°C$ peak is slightly higher. The 670 $°C$ specimen has the highest and largest peak. The similarity is caused by the small specimen sizes, diminishing the effect of the difference in microstructure, making it harder to identify. Integrating under the curve gives the total absorbed hydrogen content, since the specimen is fully melted and has released all present hydrogen. The total absorbed hydrogen content is given in Table 15. Furthermore, the total hydrogen content is shown as a function of the intercritical annealing temperature in Figure 32, compared to the estimated ferrite/martensite interface to martensite area ratio. This ratio is given

in Table 16.

Table 15: Total absorbed hydrogen content from TDS measurements for the different intercritical annealing temperatures.

Annealing Temperature [$°C$]	Total H (Std.) [$wppm$]
590	1.16 (0.11)
630	1.29 (0.13)
670	1.58 (0.27)

In Table 15, the total absorbed hydrogen content increases slightly from 1.16 ± 0.11 $wppm$ to 1.29 ± 0.13 $wppm$ with an increase in intercritical annealing temperature from 590 $°C$ to 630 $°C$, before a larger increase in the total hydrogen content to 1.58 ± 0.27 $wppm$ at 670 $°C$. The same is depicted in Figure 32. In addition, due to the difference in obtain TDS curves, the standard deviation remains large for all intercritical annealing temperatures. However, there is a clear increasing trend in the total absorbed hydrogen content. Since increasing the specimen size is not possible, due to limitations in the electrode furnace and the limited homogenous heat treated zone during heat treatment in the Gleeble, decreasing the deviation is difficult.

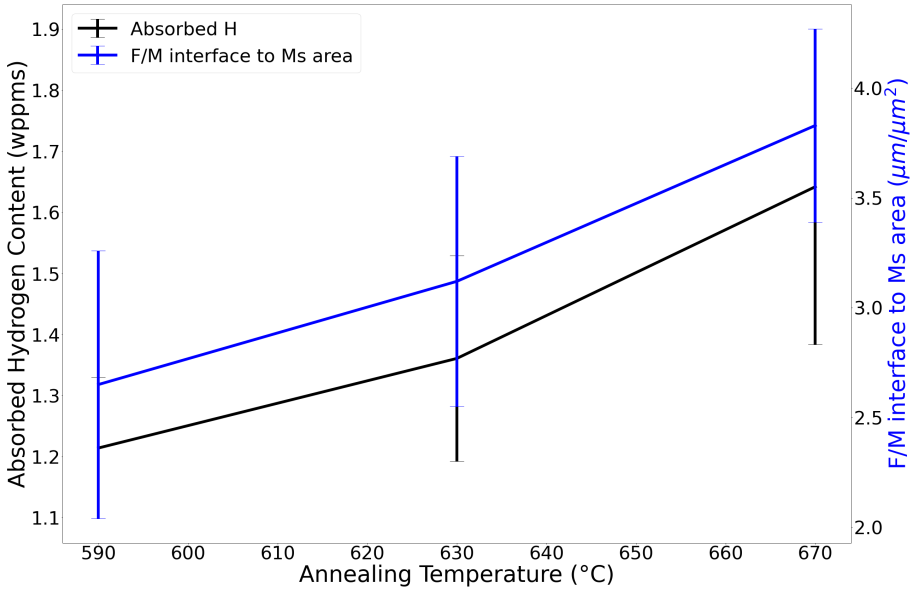

Figure 32: Total absorbed hydrogen content as a function of intercritical annealing temperature, compared to the increase in the F/M interface length to martensite area ratio.

It is expected that the hydrogen content would increase with an increase in martensite content. When comparing hydrogen contents obtained in literature, a low increase in hydrogen content with a large standard deviation with increasing martensite content is similarly reported. In the work of Drexler et al., the hydrogen contents of a DP600, DP800, and DP1000 steel are reported as 2.07 ± 0.31 $wppm$ 2.20 ± 0.12 $wppm$, and 2.67 ± 0.19 $wppm$ respectively [26]. While the absolute value of the total hydrogen content is not comparable, since the steel is different in composition,

microstructure, and specimen size, the increase in hydrogen content with increasing martensite content similarly seen here. This is similarly seen in the work of Rodoni et al. [28].

In literature, the ferrite/martensite interface is identified as the main trapping site for hydrogen in DP steel [24]. Table 16 shows the ferrite/martensite length to martensite grain area ratio, estimated on the SEM images of dilatometry specimen using the *ImageJ* software. This ratio gives an indication in how the ferrite/martensite interface increases with increasing intercritical annealing temperature. Since the ratio increases steadily from $2.65 \pm 0.61 \cdot 10^{-2}$ $\mu m/\mu m^2$ to $3.12 \pm 0.57 \cdot 10^{-2}$ $\mu m/\mu m^2$ and $3.86 \pm 0.44 \cdot 10^{-2}$ $\mu m/\mu m^2$ with intercritical annealing at 590 $°C$, 630 $°C$, and 670 $°C$ respectively, an increase in martensite content leads to an increase in the ferrite/martensite interface area.

Table 16: Ratio of the ferrite/martensite interface length to the martensite grain area ratio from SEM images of the specimen microstructure.

Annealing Temperature [$°C$]	F/M to Ms Area Ratio (Std.) [$\mu m/\mu m^2 \cdot 10^{-2}$]
590	2.65 (0.61)
630	3.12 (0.57)
670	3.83 (0.44)

When comparing the total absorbed hydrogen to the ferrite/martensite interface to martensite area ratio, there is a similar increasing trend with increasing intercritical annealing temperature. This indicates that more hydrogen can be accommodated and trapped at higher intercritical annealing temperatures, due to an increase in the ferrite/martensite interface.

Overall, from TDS an increase in the total absorbed hydrogen content is found with increasing intercritical annealing temperature. There is variance in the obtained data, although similar development and variance is seen in literature. The increase in the total absorbed hydrogen content is attributed to the increasing martensite content and increasing ferrite/martensite area, providing more trapping sites for hydrogen.

4.4 Slow Strain-Rate Tensile Testing

During SSRT testing both nominal and engineering (extensometer) stress-strain curves were obtained for benchmarking the mechanical properties, while only nominal strain curves in an HE environment. The nominal strain curves for both benchmarking and HE specimens are given in Appendix H. As they give the deformation of the entire tensile setup, it does not accurately capture the response of the material in the heat treated double-necked region. Furthermore, the measured load-train displacement curves from the benchmarking specimens is also presented there. The engineering stress-strain curves of the benchmarking specimens are given in Figure 33.

The highest UTS value is found for the 670 $°C$ specimen (1115 ± 15 MPa), and the lowest for the 590 $°C$ specimen (756 ± 20 MPa), due to the specimens respectively contain the highest (78 ± 7

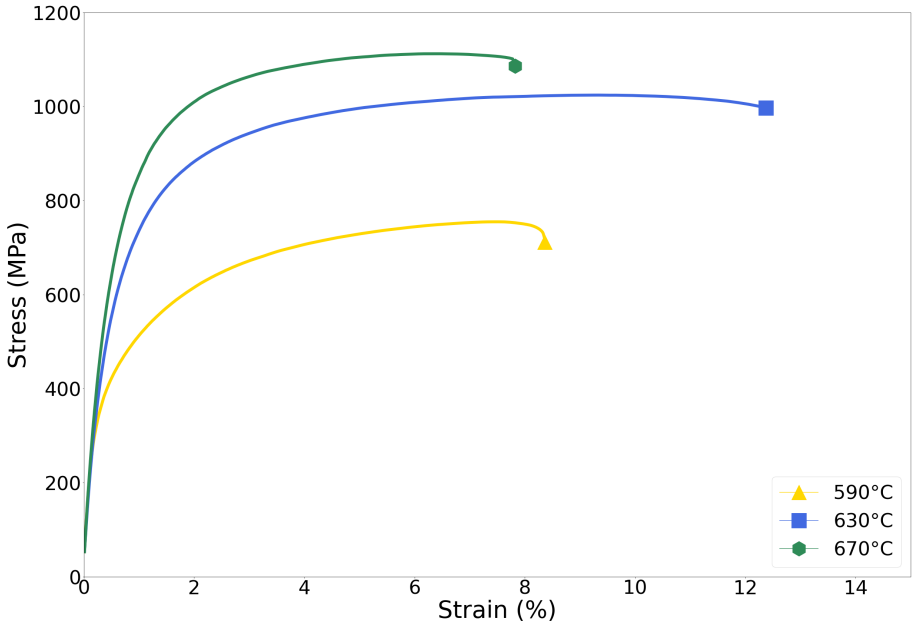

Figure 33: Engineering stress-strain curves for the specimens intercritically annealed at 590 $°C$ (yellow), 630 $°C$ (blue) and 670 $°C$ (green).

%) and lowest martensite contents (25 ± 6 %). Similarly, the 630 $°C$ specimens have an UTS between these points (1025 ± 8 MPa), with a martensite content of 50 ± 4 %. The UTS increases with increasing martensite content, as it is the stronger phase. Since, the UTS is used to designate the obtained DP steel, intercritical annealing at 590 $°C$, 630 $°C$, and 670 $°C$ results in a DP800, DP1000, and DP1100 steel respectively.

Regarding the elongation at fracture, it would be expected to decrease with increasing martensite content. However, with the benchmarking results obtained, the elongation at fracture increases from 8.4 ± 1.7 % to 12.6 ± 0.6 % when the intercritical annealing temperature increases from 590 $°C$ to 630 $°C$, before decreasing to 8.2 ± 0.8 % at 670 $°C$. This can be explained by the higher martensite phase fraction providing greater strength to the steel, without diminishing the ferrite content sufficiently to decrease the accommodation of strain in the ductile ferrite phase. At the lower martensite contents there is a continuous network of ferrite, which can accommodate the strain. When the martensite content increases and becomes dominant in the microstructure ($\sim 78 \pm 7$ %) a continuous network of martensite begins to form, which significantly diminished the ability of ferrite to accommodate strain. Hence, the optimal mechanical properties for lightweight applications, both high strength and ductility, are present with an equal phase fraction of ferrite and martensite. Table 17 show relevant mechanical properties for the benchmarking specimens quantifying the UTS and the elongation at fracture from the stress-strain curves.

Table 17: The UTS and fracture strain obtained from the SSRT engineering stress-strain curves for the benchmarking specimens.

Annealing Temperature [$°C$]	σ_{uts} (Std.) [MPa]	ε_{frac} (Std.) [%]
590	756 (20)	8.4 (1.7)
630	1025 (8)	12.6 (0.6)
670	1115 (15)	8.2 (0.8)

During the SSRT of HE affected specimen, the engineering strain is estimated based on the load-train displacement from the benchmarking specimens. The method for this is depicted in Figure 34. For capturing of the HE effect, only the estimated stress-strain curves are depicted in this section. The obtained nominal stress-strain curves are given in Appendix H, as previously mentioned.

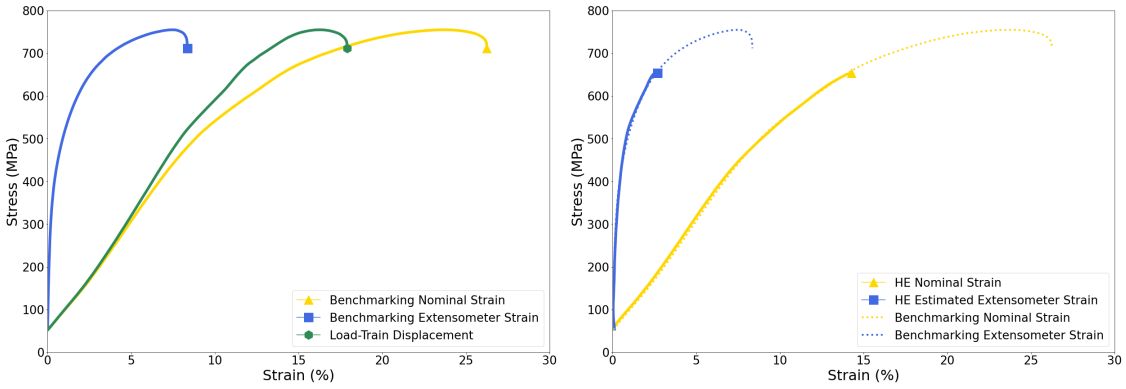

(a) (b)

Figure 34: Estimation of the engineering strain in an HE environment, a) load-train deformation as a function of force (green), the engineering strain (blue), and nominal strain (yellow) in benchmarking case, applied to the b) HE curve with the recorded nominal strain (yellow) and the estimated engineering strain (blue).

As seen in Figure 34a the load-train displacement curve is found by subtracting the engineering (extensometer) curve from the nominal curve. The load-train displacement is then applied to the HE affected nominal strain curve in Figure 34b, producing the estimated engineering stress-strain curve. As seen in the figure, this follows both the engineering and nominal stress-strain curve of the benchmarking specimen (dashed), giving an accurate depiction of the reduction in ductility due to HE. Figure 35 shows the estimated engineering stress-strain curves of the HE affected specimens, compared to those of the benchmarking specimens.

In Figure 35, the HE effect for the different specimens becomes clear, with a clear reduction in ductility with HE. When comparing the HE environment engineering stress-strain curves to the benchmarking, the largest difference in the tensile curves is present for the specimen intercritically annealed at 630 $°C$, with a reduction from 12.6 ± 0.6 % to 1.8 ± 0.2 %. This is followed by the 670 $°C$ specimen, with a reduction from 8.2 ± 0.8 % to 1.6 ± 0.1 %. The least reduction of fracture

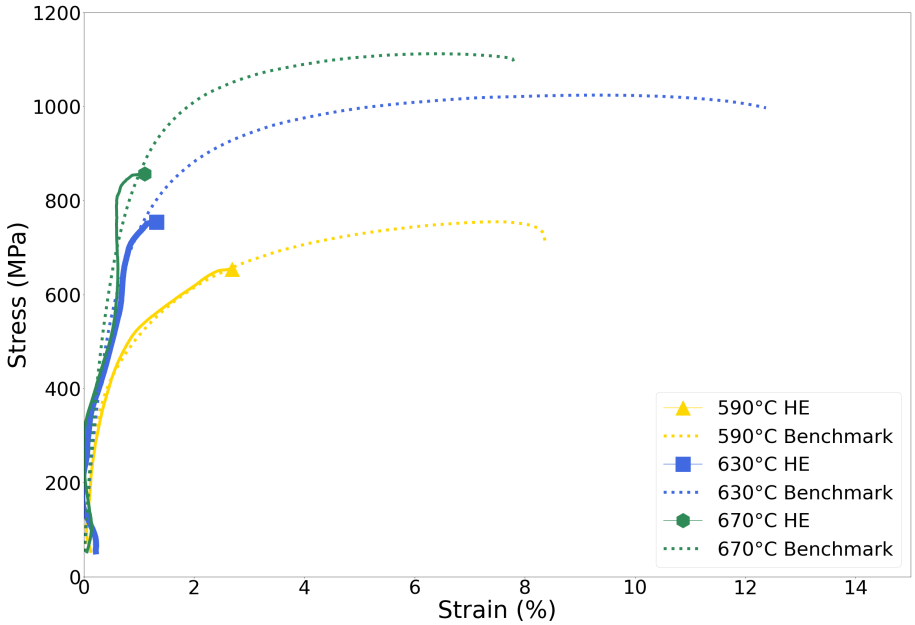

Figure 35: Engineering stress-strain curves for the specimens intercritically annealed at 590 $°C$ (yellow), 630 $°C$ (blue) and 670 $°C$ (green) showing the change in the engineering stress-strain curve due to HE, with the dashed benchmarking engineering stress-strain curves for comparison.

strain is for the 590 $°C$ specimen, from 8.4 ± 1.7 % to 4.1 ± 0.7 %.

The estimated engineering stress-strain curves does not have the exact same slope as the benchmarking stress-strain curve, although the fracture point lies on the curve. This is a result of observed hysteresis of the polymer components of the tensile setup, resulting in a deviation between the benchmarking and HE nominal strain curves. Furthermore, this can be the result of the presence of the charging solution in the bath, affecting the submerged components of the tensile testing setup. Additionally, it can be caused by the two-hour charging period in which the specimen experiences some tension (< 250 N), to ensure the specimen cannot move. This affects the hysteresis of the polymeric components, giving the elastic region of the benchmarking stress-strain curve a slight difference in slope compared to the HE stress-strain curves. However, in the estimation of the engineering stress-strain curves this is accounted for, causing the final fracture point to be accurate. Only the maximum stress and elongation at fracture can be quantified. This is given in Table 18.

Table 18: Relevant mechanical properties obtained from the SSRT engineering stress-strain curves from testing in a HE environment. This includes the maximum recorded stress and the estimated engineering strain at the maximum stress level.

Annealing Temperature [$°C$]	σ_{max} (Std.) [MPa]	ε_{frac} (Std.) [%]
590	677 (21)	4.1 (0.7)
630	798 (35)	1.8 (0.2)
670	877 (20)	1.6 (0.1)

As the intercritical annealing temperature increases, so does the maximum stress. The maximum stress is $677 \pm 21\ MPa$, $798 \pm 35\ MPa$, and $877 \pm 20\ MPa$ for the specimen intercritically annealed at 590 $°C$, 630 $°C$ and 670 $°C$ respectively. This is, as for the UTS, attributed to the increased martensite content providing a stiffness to the steel, increasing the stress at a given elongation. The fracture elongation of the estimated stress-strain curves, however, decreases with increasing intercritical annealing temperature. From this the embrittlement index is calculated, seen in Equation 17, which based on Equation 15 in Section 2.3.3. This is given in Table 19, with the embrittlement indexes based on the elongation at fracture of the benchmarking and estimated HE engineering stress-strain curves. The development of the embrittlement index based on the engineering stress-strain curves with increasing intercritical annealing temperature is also depicted in Figure 36.

$$I_\varepsilon = \frac{\varepsilon_{frac,\,bench} - \varepsilon_{frac,\,HE}}{\varepsilon_{frac,\,bench}} \cdot 100\% \tag{17}$$

Table 19: Calculated embrittlement index for the different intercritical annealing temperatures.

Annealing Temperature [$°C$]	I_ε (Std.) [%]
590	59 (7)
630	89 (1)
670	86 (3)

As seen in Table 19 and Figure 36, with an increase in the intercritical annealing temperature, there is first a significant increase in the embrittlement index from 59 ± 7 % to 89 ± 1 % when the intercritical annealing temperature increases from 590 $°C$ to 630 $°C$, before a slight decrease to 86 ± 3 % at 670 $°C$. This agrees with the observation in Figure 35, that the 630 $°C$ specimen has the lowest elongation at fracture in a HE environment, while having the longest elongation at fracture during the benchmarking.

It would be expected that increasing intercritical annealing temperatures causes a higher embrittlement index, due to a higher martensite content. However, there are multiple possible explanations of the obtained embrittlement index for the 630 $°C$ specimens, which are discussed in the following paragraphs.

Dislocation pile-up around the martensite islands can explain the similar mechanical behavior for the 630 $°C$ and 670 $°C$ specimens. For the 630 $°C$ specimen, dislocation pile-up around the martensite islands cause an increase in the overall brittleness which severely influenced by HE, with dislocation movement facilitated by the HELP mechanism. Furthermore, the increased ferrite content in the 630 $°C$, compared to the 670 $°C$ specimen, allow for easier diffusion of hydrogen, as the ferrite phase allows for easier diffusion of hydrogen. Since the 630 $°C$ contains a discontinuous martensite network, hydrogen can diffuse fast through ferrite channels towards deformation, increasing the HE effect. Further explanation of the similar mechanical behavior, can

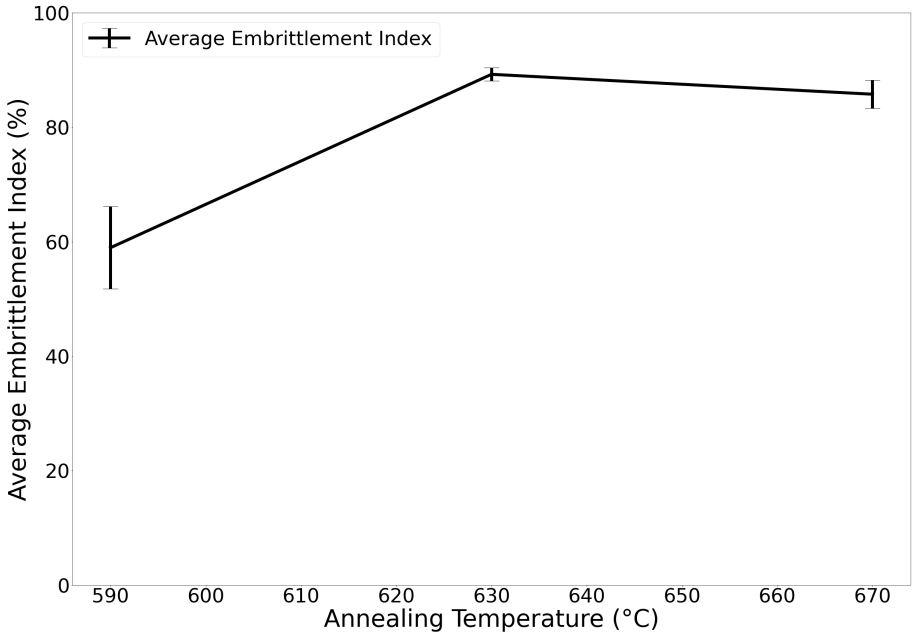

Figure 36: Embrittlement index calculated from the nominal and engineering strain depending on the intercritical annealing temperature.

be found in the investigation of the fracture surface.

The benchmarking properties, which show the mechanical properties as a result of heat treatment can be compared to those obtained by Drexler et al. and Adamczyk et al., where distinct martensite content have been obtained [19, 26]. In the work of Adamczyk et al., which was first seen in Table 2 in Section 2.1.3, a similar production route results in a DP1000 steel, with a UTS of 998 MPa, with a total elongation of 14.6 %. Similarly, in the work of Drexler et al., seen first in Table 4 in Section 2.4, the DP1000 steel obtained there has a UTS of 1087 MPa and a fracture strain of 13 %. Compared to the DP1000 steel obtained here, the specimen intercritically annealed at 630 $°C$, with an UTS of 1025 ± 8 MPa, has a similar fracture strain of 12.6 ± 0.6 %. This indicates the obtained mechanical properties of the 630 $°C$ specimen are similar to what is obtained in literature. However, comparing the 590 $°C$ specimen, a DP800 steel, is different. For the DP800 steel obtained by Drexler et al., a fracture strain of 19 % is obtained, while a fracture strain of 8.4 ± 1.7 % is obtained by the 590 $°C$ specimen. The difference is caused by the tensile specimen of Drexler et al. being obtained parallel to the rolling direction, while in this work they are perpendicular to the rolling direction. Since there is a presence of texture in the specimens, and a banding of the microstructure is obtained, the orientation of the specimen microstructure in the tensile specimen will have a significant effect. However, the similarity of the DP1000 steel to that of the 630 $°C$ specimen, is attributed to a less textured DP1000 specimen in the work of Drexler et al.

The embrittlement index as a function of martensite content can be compared to that of Rodoni et al. [28]. In their work, for their specimen with a martensite content of 50.7 %, they obtained an embrittlement index of 77 %. Similarly, for the 630 $°C$ specimen, with a martensite content of 50 ± 4 % a similar embrittlement index of 89 ± 1 % is calculated. In the work of Li et al., a DP800 steel is tested with different intercritical annealing times [36]. Their results indicate an embrittlement index of 60 %, 55 %, and 62 % with intercritical annealing times of 30, 45 and 60 minutes. Comparing to the 590 $°C$, which has a UTS of 756 ± 20 MPa, a similar embrittlement index of 59 ± 7 % is found. The martensite content of Li et al. is not reported. However, since it

has been found that the intercritical annealing time does not significantly change the martensite content, comparison is possible. Overall, this shows that the obtained embrittlement index is comparable to what is obtained in literature.

Overall, the main findings for the mechanical performance due to heat treatment and HE is that an optimal combination of UTS and maximum elongation ins found for the specimen with an intercritical annealing temperature of 630 $°C$. However, this specimen also experiences the highest embrittlement index. As martensite content increases from 25 ± 6 %, so does the HE. However, since it is highest at the specimen with 50 ± 4 % martensite, investigation into the fracture surface must be done to explain the extreme increase in embrittlement.

4.5 Overview of Quantified Results

Table 20 gives an overview of the quantified results obtained, to provide clarity and ease of comparison. As seen in the table, as intercritical annealing temperature increase, so does the martensite content. With increasing martensite content, there is an increase in the hardness and the grain size. Increasing grain size increases the ferrite/martensite interface to martensite area ratio, which influences the HE properties. There is an increase in the total absorbed hydrogen content, due to a larger ferrite/martensite ratio. However, while there is an increase in the embrittlement index with increased intercritical annealing temperature, the highest is found in the 630 $°C$ condition.

Table 20: Overview of the obtained quantified results (Std.) for the different intercritical annealing temperature (Ann. temp.).

Ann. temp. $[°C]$	Martensite content [%]	Hardness $[HV1]$	Grain size $[\mu m]$	F/M ratio $[\mu m/\mu m^2 \cdot 10^{-2}]$	Hydrogen content $[wppm]$	HE index [%]
590	25 (5)	238 (25)	3.9 (2.6)	2.65 (0.61)	1.16 (0.11)	59 (7)
630	50 (4)	286 (13)	5.9 (3.2)	3.12 (0.57)	1.29 (0.13)	89 (1)
670	78 (7)	344 (12)	7.4 (3.4)	3.83 (0.44)	1.58 (0.27)	86 (3)

4.6 Fractographic Analysis

SEM fractography of benchmarking and HE affected specimens, and EBSD of interrupted and fractured SSRT specimens are done to investigate the underlying fracture micromechanisms in a HE affected state. Figure 37 shows the SEM fractography images of the benchmarking specimens intercritically annealed at 670 $°C$, to investigate the fracture surface of an unaffected specimen. This includes an overview image with magnification 20x and specific investigated location with magnification 1000x. The SEM fractography images obtained for the specimens intercritically annealed at 590 $°C$ and 630 $°C$ are given in Appendix I.

Across the entire specimen there are ductile dimples (indicated by the green arrows) present in the fracture surface, indicating ductile fracture has occurred. Additionally, the ductile dimples are present on all locations investigated in the specimen. Figure 37c shows that the dimples and fracture surface are protracted in the horizontal direction, towards the centerline, indicating it is part of the final rupture of the specimen. The same fracture surface is present in the benchmarking specimens with intercritical annealing at 590 $°C$ and 630 $°C$, with no comparable difference. Comparing with the fracture surfaces obtained in the work of Wang et al. (2020), yield that for

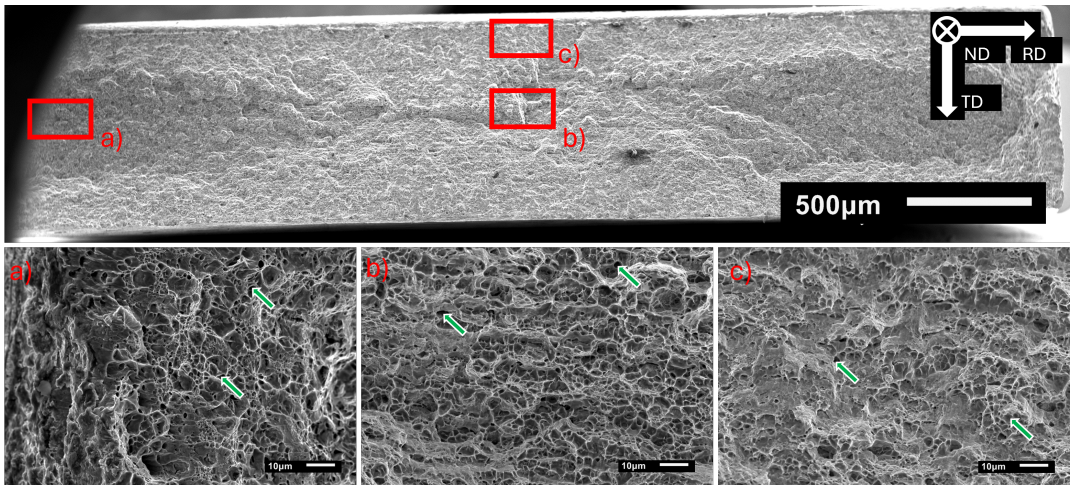

Figure 37: SEM fractography image of the benchmarking tensile specimen intercritically annealed at 670 $°C$ at magnifications 30x and 1000x showing an overview of the fracture surface and highlighted locations of interest. Green arrow indicate ductile dimples.

the non-charged condition, the same fracture surface is present at different martensite contents (18.5 % and 96.3 %) and to those obtained here [23].

The fracture surfaces of the HE affected specimens intercritically annealed at 590 $°C$, 630 $°C$, and 670 $°C$ are given in Figures 38-40, presented in the same manner as the benchmarking specimen.

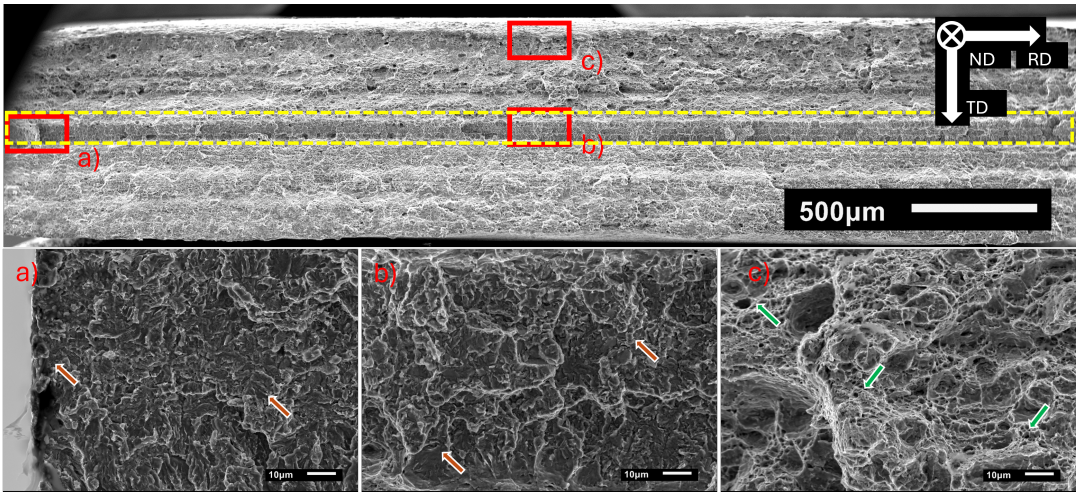

Figure 38: SEM fractography image of the HE tensile specimen intercritically annealed at 590 $°C$ at magnifications 30x and 1000x showing an overview of the fracture surface and highlighted (red) locations of interest. The identified quasi-cleavage bands are indicated by the yellow dashed area. Orange arrows show location giving evidence of quasi-cleavage fracture, and green indicate ductile dimples.

For the 590 $°C$ specimen, there is a quasi-cleavage band going across the centerline of the entire specimen cross-section, indicated by the yellow dashed box. This band, measuring 100 μm in diameter, does not change across the specimen entire specimen, indicated by the same fracture facets being present in Figures 38a, and b. As indicated by the orange arrows, clear quasi-cleavage facets are present, seen as cleavage-like fracture along the non-cleavage planes. Furthermore, outside this quasi-cleavage band at the edge of the specimen, in Figure 38c, the fracture surface consists of ductile dimples, indicating the final ductile failure. However, unlike the benchmarking

specimen there is no clear protraction of the ductile dimples. This can be caused by the decreased ductile elongation of the specimen in an HE environment, and a more violent final rupture.

In the 630 $°C$ specimen, seen in Figure 39 the multiple quasi-cleavage bands are present on the fracture surface, indicated by the yellow dashed boxes. These are less clearly defined as seen in the 590 $°C$ specimen, due to them being present on multiple levels, seen in Figure 39a. Each band has a diameter of approximately 50 μm. As annotated by the orange arrows in the Figure 39a, there are clear quasi-cleavage facets present. In the center of the specimen, Figure 39b, there is a mix of ductile dimples and some quasi-cleavage facets. The dimples are shallower than in the benchmarking case, indicating a more brittle fracture. At the center of the long side of the specimen, Figure 39c, the fracture surface exhibits the same ductile dimples as seen for the 590 $°C$ case (Figure 38c), with larger ductile dimples. The simultaneous occurrence of both ductile dimples and quasi-cleavage fracture facets in the center of the specimen is similarly reported in literature [23].

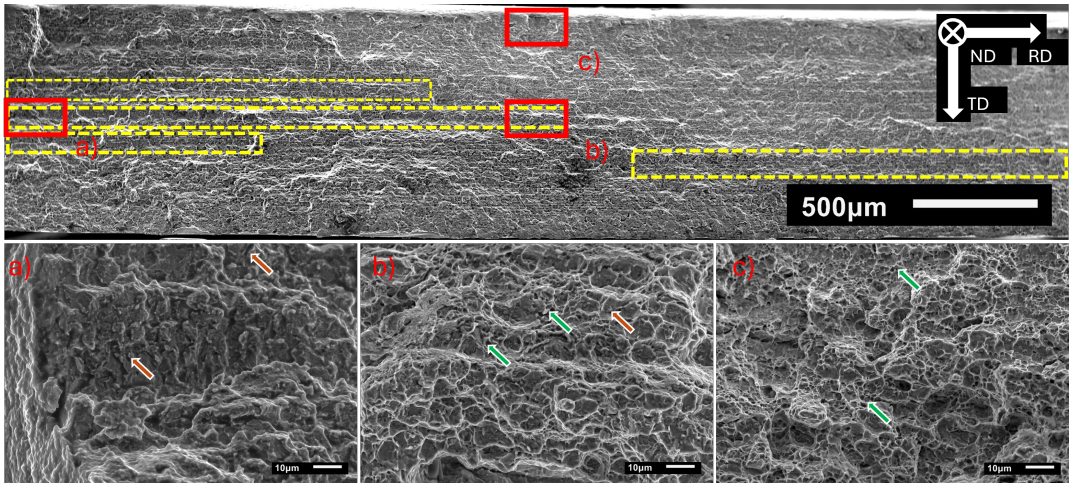

Figure 39: SEM fractography image of the HE tensile specimen intercritically annealed at 630 $°C$ at magnifications 30x and 1000x showing an overview of the fracture surface and highlighted (red) locations of interest. The identified quasi-cleavage bands are indicated by the yellow dashed area. Orange arrows show location giving evidence of quasi-cleavage fracture, and green indicate ductile dimples.

For the 670 $°C$ specimen, a large quasi-cleavage band is again present in the fracture surface, measuring 200 μm in the center. Additionally, the area increases towards the edges of the specimen, to 450 μm. At both the center and the edge of the quasi-cleavage band, Figures 40a and b, the quasi-cleavage facets are identified. Furthermore, some shallow dimples are identified at the edge, indicated by green arrows in Figure 40a. At the center of the long side edge of the specimen, the ductile dimples are predominant in the fracture surface, as seen and described for the other specimens. The predominant quasi-cleavage fracture in the 670 $°C$ specimen, with a martensite content of 78 ± 7 %, is seen in literature [23, 36].

For all three specimens the main fracture mode is transgranular, with quasi-cleavage fracture facets and some shallow ductile dimples. These are found in the HEDE and HELP mechanisms of HE. However, the presence of the quasi-cleavage fracture bands are not reported in literature. Rather, quasi-cleavage fracture is expected to initiate at the corners of the specimen, due to a build-up of hydrogen. Therefore, to find an explanation of the observed quasi-cleavage bands through the specimen, two questions must be answered. The first is: Why does the quasi-cleavage fracture

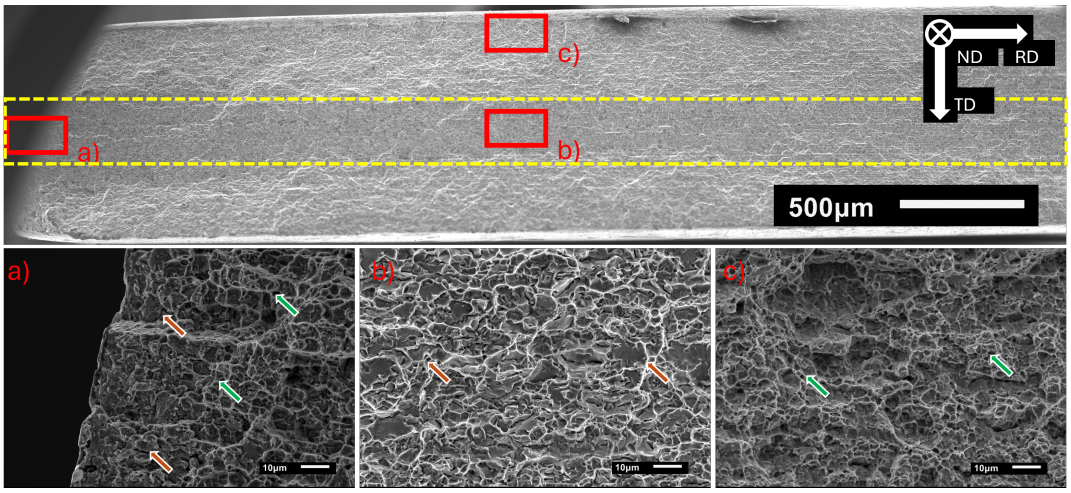

Figure 40: SEM fractography image of the HE tensile specimen intercritically annealed at 670 $°C$ at magnifications 30x and 1000x showing an overview of the fracture surface and highlighted (red) locations of interest. The identified quasi-cleavage bands are indicated by the yellow dashed area. Orange arrows show location giving evidence of quasi-cleavage fracture, and green indicate ductile dimples.

band form across the specimen cross-section? The second question is: Why do the quasi-cleavage fracture bands predominantly form in the center of the short side of the specimen and not at other locations? To answer these questions the cross-sectional microstructure of the Gleeble tensile specimens is investigated. These are seen in Figure 41.

For all intercritical annealing conditions, there is a clear texture and banding of the ferrite and martensite phases in the cross-sectional plane. There are bands in the microstructure consisting entirely of martensite and ferrite across the entire width of the specimen. This is a result of the hot-rolling process at which the as-received material is made. It is still present in the microstructure after heat treatment. However, this banding of the microstructure for DP steels is reported in literature [28, 65].

With the cross-sectional microstructure it is possible to answer the first question raised by the observed facture surface. Since there are clear bands of martensite and ferrite, with the martensite bands being larger than the ferrite ones, there is preferential crack growth along these bands, in the martensite phase. It is observed that the quasi-cleavage zone increases towards the short edge surface, indicting the crack nucleates there, in the martensite phase. From this the crack preferentially grows along the martensite band, since it is more brittle than the surrounding phase, achieving the quasi-cleavage fracture surface. This is seen with the limited elongation at fracture of the 630 $°C$ and 670 $°C$ specimens during HE SSRT (Figure 35), indicating little plasticity has occurred. The 590 $°C$ specimen has much higher elongation, seen by a larger ductile rupture area, and only one small quasi-cleavage band compared to the other two specimens.

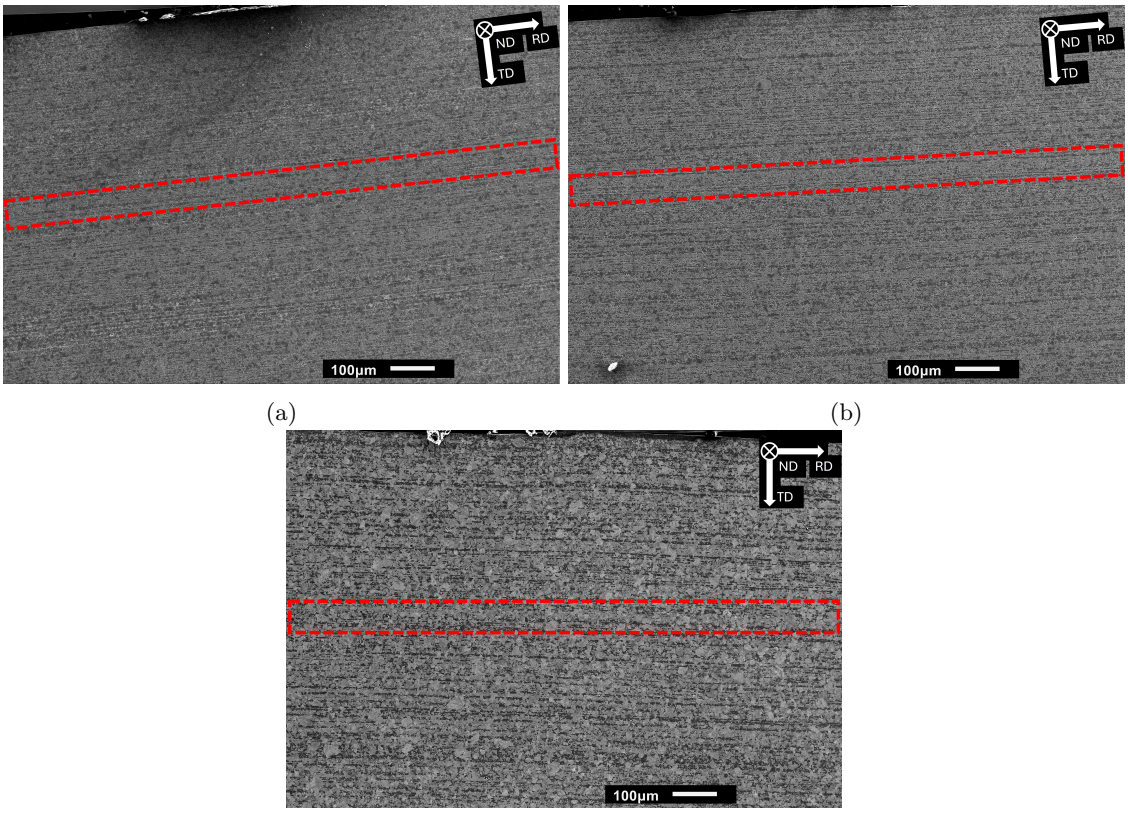

Figure 41: SEM images at magnification 100x of tensile specimens intercritically annealed at a) 590 $°C$, b) 630 $°C$, and c) 670 $°C$. The red dashed box indicate a martensite band present in the microstructure, across the horizontal distance of the specimen.

However, this does not answer the second question, and further analysis is required. This is done by the investigation of the surface layer of the specimen cross-section, comparing the long and short edges, and the corner of the specimen, seen in Figure 42.

When comparing the long and short side edges of the specimen, there is a difference in surface layer microstructure. On the long side edge surface layer consist almost of ferrite, while the short edge consists entirely of martensite. The ferrite layer is a result of the heat treatment procedure in the Gleeble, while the martensite layer is present due to EDM cutting after heat treatment. As the specimen is heat treated prior to cutting, EDM cuts through the martensite bands, exposing martensite as the surface layer. This means the short side surface layer is more susceptible to HE attack, since martensite is more susceptible than ferrite. Nucleation is encouraged in the short side of the specimen, because there is a higher accumulation of hydrogen in the surface layer than in at the long edge. The accumulation of hydrogen at the grain ferrite/martensite interface is attributed to contribute to the HEDE HE mechanism.

Furthermore, at the corner of the specimen it is clearly seen that a ferrite layer exists on the long side of the specimen, enveloping the corner. Meanwhile, the surface martensite is present ~ 20 μm from the long edge. Additionally, the upper ~ 70 μm of the specimen consist of discontinuous martensite grains, before developing into continuous martensite. Since martensite is not present at the surface, there is less hydrogen accumulation there than along the short edge of the specimen. Crack nucleation and propagation is discouraged, compared to the center of the specimen, where

surface martensite is present and continuous martensite bands are present. Furthermore, the high embrittlement index for the specimen can be attributed to the presence of surface martensite on the short edge, indicating that modifying the surface to avoid a martensite surface layer could reduce the hydrogen embrittlement of the specimen.

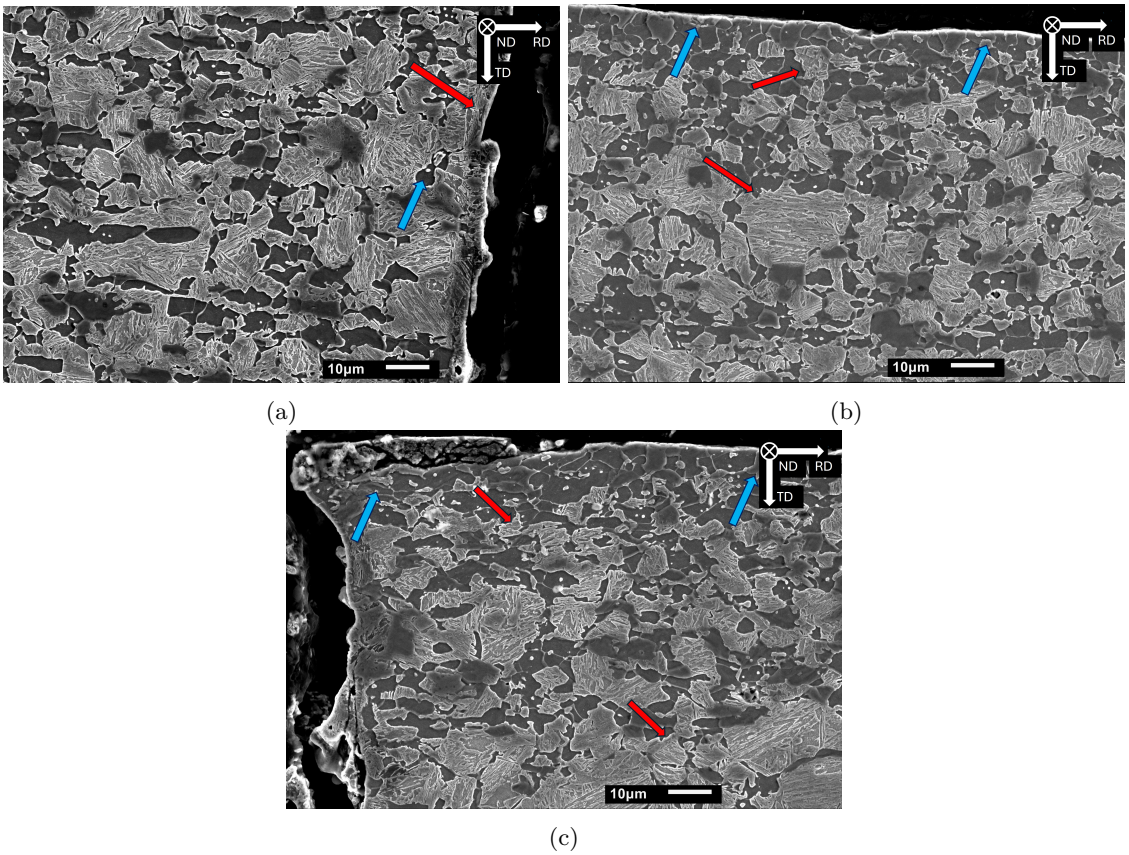

Figure 42: SEM images at magnification 1000x of tensile specimens intercritically annealed at 670 $°C$, comparing the a) short and b) long edges and c) corner of the specimen. Ferrite and martensite are respectively indicated by blue and red arrows.

Therefore, the occurrence of the quasi-cleavage bands can be explained by the preferential crack growth along the martensitic bands across the specimen cross-section. The quasi-cleavage bands originating at the short edge of the specimen, growing inward, can be explained by the martensitic surface layer at the short edge, providing preferred nucleation of cracks. This is observed at all intercritical annealing conditions. Images comparing the surface layer of the 590 $°C$ and 630 $°C$ specimens are given in Appendix I.

Comparing the different intercritical annealing conditions based on this, the occurrence of a single quasi-cleavage band in the 590 $°C$ specimen indicate the nucleation and growth of one crack in the center of the specimen. Due to the low martensite content (25 ± 5 %), simultaneous crack growth is hindered. For the 630 $°C$ specimen, with increased martensite content (50 ± 4 %), multiple quasi-cleavage bands are present, protruding at different lengths through the fracture surface, due to a nucleation of multiple cracks. Finally, for the 670 $°C$ specimen, with the highest martensite content (78 ± 7 %), there is a large quasi-cleavage area as the martensite is interconnected.

To further investigate the strain distribution during deformation, EBSD KAM maps of interrupted SSRT maps are obtained. These are given for the different intercritical annealing conditions,

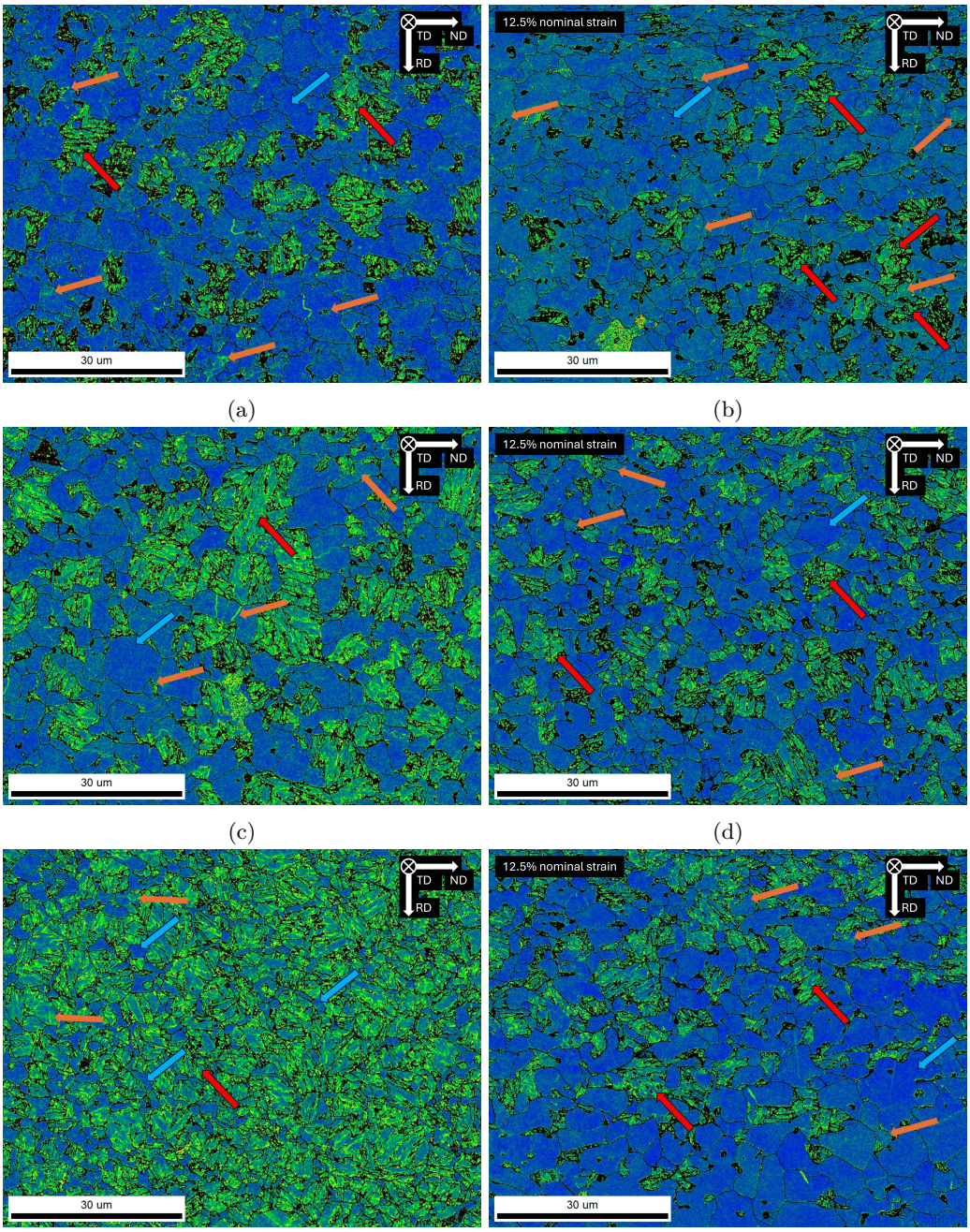

Figure 43: KAM images of a), c), e) unaffected dilatometry specimens and b), d), f) interrupted SSRT specimens strained 12.5 % nominal strain, intercritically annealed at a), b) 590 $°C$, c), d) 630 $°C$, and e), f) 670 $°C$. Blue indicates low KAM values, while green/yellow/red indicate increasing KAM. Blue arrows indicate the ferrite grains, red arrows the martensite grains, and the black lines show a rotation angle above 15° indicating grain boundaries. Orange arrows indicate locations on the specimens with increased KAM values.

comparing with unaffected dilatometry specimens in Figure 43.

It becomes clear that the comparison between unaffected and HE specimen yield little to no result. Only for the 590 $°C$ an increase in the KAM of indicated grains is found. For the 630 $°C$ specimens, while the microstructure is similar, there is no identified increase in KAM as a result of straining. There are different martensite contents for the locations analyzed for the 670 $°C$ specimen, making comparison difficult. The HE affected interrupted specimen, Figure 43f, is taken for a region of low martensite content. For the 630 $°C$ and 670 $°C$ specimens, there is not enough plastic deformation occurring in the specimen as the specimens fracture at low strains, which is seen in the engineering stress-strain curves, Figure 35. Even for the 590 $°C$ specimen, which has more elongation before fracture, has a low increase in KAM in some grains, compared to the unaffected specimen. Therefore, it is evident that using interrupted SSRT with EBSD to investigate the strain localization during deformation is only applicable when there is considerable plastic deformation (> 2.5 %).

As an alternative to the 630 $°C$ and 670 $°C$ interrupted SSRT specimens, which do not give any indication of strain localization during interrupted SSRT testing, EBSD is conducted using fractured specimen. By investigating a region ~ 150 μm from the fracture edge, the strain localization of the plastically deformed zone is seen. This is given in Figure 44a. At locations closer than 150 μm to the fracture surface there is grain refinement due to dislocation pile-up, therefore not giving an accurate a representation of the strain localization in the specimen microstructure.

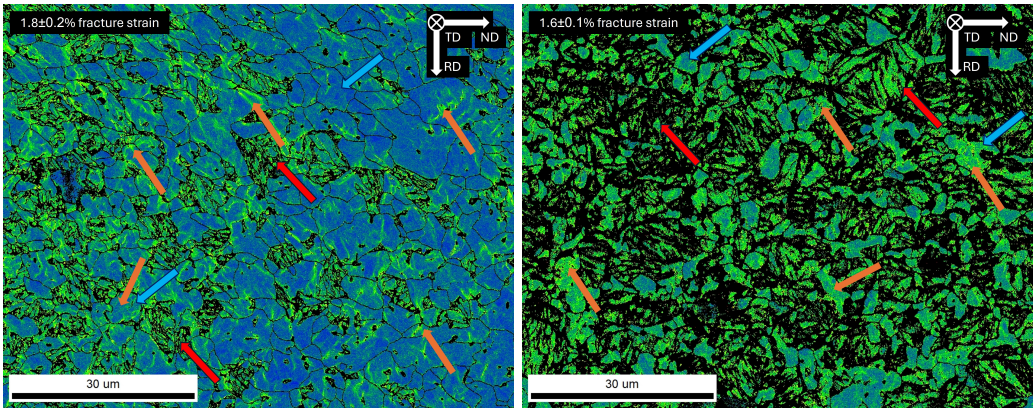

(a) (b)

Figure 44: KAM image obtained from EBSD of SSRT specimen intercritically annealed at a) 630 $°C$ and b) 670 $°C$, 150 μm from the fracture edge. Blue indicate low KAM values, while green/yellow/red indicate increasing KAM. Blue arrows indicate the ferrite grains, red arrows the martensite grains, and the black lines show a rotation angle above 15° indicating grain boundaries. Orange arrows indicate locations on the specimens with increased KAM values.

For the fractured 630 $°C$ specimen, there is a significant increase in KAM at multiple locations in the specimen. Particularly, the increase KAM is located close to the ferrite/martensite grain interfaces, and in ferrite grains surrounding martensite grains. Furthermore, there is an increase in KAM surrounding martensite islands, indicating they are important for the fracture of the specimen. The strain localization lies at an 45° angle to the tensile loading direction, at the angle of highest shear stress. It can be determined that the deformation is located at and surrounding the ferrite/martensite interface. Therefore, the fracture propagates surrounding and at the ferrite/martensite interface in the microstructure.

Similarly, in the 670 $°C$ specimen, there is an increase in the KAM within ferrite grains, particularly close to the ferrite/martensite interface. However, due to the majority of the specimen consisting of martensite, the KAM is inherently high. Compared to the unaffected specimen, Figure 43e, there is a higher KAM in the ferrite grains as a result of deformation. Furthermore, the larger boundary area, indicating martensite, show that there is more distortion within the martensite grains as well. The martensite/ferrite interface is identified as an important location for the fracture of the specimen.

The strain localization at and surrounding the ferrite/martensite interface can be explained by the strain controlled tensile loading. When the tensile loading is applied in a strain controlled manner, a same stress is experienced in the ferrite and martensite phases. In the ferrite phase, dislocations are generated due to this, which pile-up at the ferrite/martensite interface. Furthermore, hydrogen migrate towards the dislocations, increasing their movement and pile-up, causing embrittlement, which is according to the HELP mechanisms. This is further affected by the ferrite/martensite interface acting as a main trapping site, so hydrogen is readily available close to the dislocation pile-up, this increasing the HE. The transgranular quasi-cleavage fracture surface with shallow dimples is indicative of the HELP mechanism.

Overall, investigation of the fracture micromechanisms show that the fracture nucleate at the short edge surface, where surface layer martensite is present, before propagating across martensitic bands present in the microstructure, close to the ferrite/martensite interface. Furthermore, stress is accommodated by dislocation build-up close to the ferrite/martensite interface. A schematic overview of the proposed HE fracture mechanism is seen in Figure 45, where hydrogen is preferentially absorbed on the short edge of the specimen and is trapped in the ferrite/martensite interface. The presence of surface martensite and the accumulation of hydrogen facilitates the crack nucleation at the short surface edge of the specimen due to HEDE and HELP, which then propagates across the martensite band due to the hydrogen accumulation in the ferrite/martensite interface. This is also facilitated by the HEDE and HELP mechanisms, causing increased movement of dislocations and a weakening of the interatomic iron-bonds.

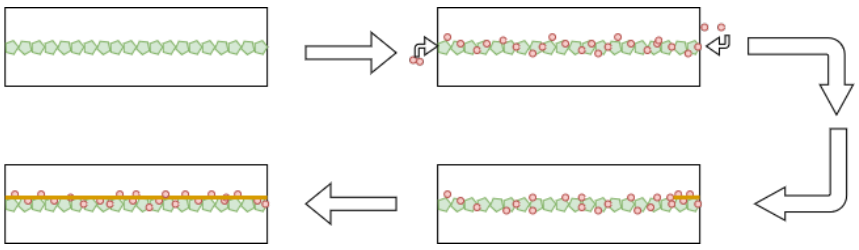

Figure 45: Schematic drawing of the proposed HE action, where the hydrogen (red) has preferential entry at the short edge of the specimen, and is trapped in the ferrite/martensite interface. The crack nucleates at the short edge martensite, and propagates along the martensite band (green).

Furthermore, interrupted SSRT with EBSD is shown to not be effective unless significant strain is applied to the specimen. While EBSD of fractured specimen close to the fracture edge is an alternative, it is only effective at low martensite contents ($<\sim 50$ %). At higher martensite contents, distinguishing between increasing KAM due to deformation or due to increased martensite content is difficult.

5 Conclusions

The overall aim of this thesis project is to *evaluate the effect of martensite content on the microstructure and the hydrogen embrittlement of dual-phase steel.* This was further divided into distinct sub-objectives. Based on the work presented the following conclusion relating to the distinct sub-objective can be made:

1. Designing and experimentally validating heat treatment profiles with varying intercritical annealing temperature, resulting in distinct martensite phase fractions of 20 %, 50 %, and 80 %.

   By intercritical annealing in the A_r intercritical region, determined to go from 571 ± 10 $°C$ to 686 ± 1 $°C$, distinct martensite phase fractions are obtained. By intercritical annealing at 590 $°C$, 630 $°C$ and 670 $°C$, respective martensite contents of 25 ± 6 %, 50 ± 4 %, and 78 ± 7 % are found. The intercritical annealing temperature is found to be more important than intercritical annealing time when obtaining distinct martensite contents. Hardness measurements are verified as a quick and accurate method to compare heat treatment methods and as an estimation of the martensite content.

   With intercritical annealing temperature the martensite distribution changes from a discontinuous network of martensite lath grains and martensite islands within the ferrite grain matrix at 590 $°C$, to a continuous network of martensite grains with interdispersed ferrite grains at 670 $°C$. The average martensite grain size increases from 3.9 ± 2.6 μm at 590 $°C$, to 5.9 ± 3.2 μm at 630 $°C$, and 7.4 ± 3.4 μm at 670 $°C$.

2. Quantifying the effect of the obtained microstructure on the absorbed hydrogen content and the nature of traps within the microstructure.

   An increase in the total absorbed hydrogen content is found with increasing martensite content, with hydrogen contents of 1.16 ± 0.11 $wppm$, 1.29 ± 0.13 $wppm$, and 1.58 ± 0.27 $wppm$ found for intercritical annealing temperatures of 590 $°C$, 630 $°C$ and 670 $°C$ respectively. This increase is attributed to the increase in the ferrite/martensite interface with increasing martensite content.

3. Determining the change in the static mechanical properties as a result of both heat treatment and HE in an in-situ environment.

   Through SSRT tests, the heat treatment of tensile specimens results in an increase in UTS from 756 ± 20 MPa to 1025 ± 8 MPa and 1115 ± 15 MPa with intercritical annealing at 590 $°C$, 630 $°C$, and 670 $°C$ respectively. The highest elongation at fracture is for the 630$°C$ specimen, at 12.6 ± 0.6 %, while it is distincly lower at 8.4 ± 1.7 % and 8.2 ± 0.8 % for the 590 $°C$ and 670 $°C$ specimens respectively. The optimal combination of stress-strain found for the 630 $°C$ specimen is caused by a non-continuous martensite distribution, with a higher martensite content than the 590 $°C$ specimen, providing greater strength and significant plastic deformation from the continuous ferrite network, not present in the 670 $°C$ specimen.

   Significant HE is present for all specimens during SSRT in an in-situ HE environment, highest for the 630 $°C$ at 89 ± 1 %. This is followed by the 670 $°C$ and 590 $°C$, with embrittlement indexes of 86 ± 3 % and 59 ± 7 % respectively. These embrittlement indexes are similarly reported in literature for similar martensite contents. The highest embrittlement index for the 630 $°C$ specimen is due to by an increase in available trapping sites at the ferrite/martensite

interface, due to a higher martensite content compared to the 590 $°C$ specimen, and easier diffusion of hydrogen through the continuous ferrite phase causing embrittlement, compared to the 670 $°C$ specimen.

4. Identifying the underlying HE fracture micromechanisms.

   Fractography investigation of the benchmarking surface show that there are ductile dimples present across the entire fracture surfaces, showing a typical ductile fracture surface, similarly seen in literature. For all specimens in an HE environment, quasi-cleavage fracture bands are seen across the specimens. With increasing intercritical annealing temperatures, these bands go from one single band at 590 $°C$, to multiple bands in the 630 $°C$ specimen, and one large consolidated band in the 670 $°C$ specimen. EBSD investigation of interrupted SSRT tests yield little to no comparabale results, due to low plastic deformation. However, EBSD of the plastically deformed zone 150 μm from the fracture edge, show that there is a stress localization at the ferrite/martensite interface, particularly surrounding martensite islands, indicating their importance for crack propagation. At higher martensite contents, finding the increase in KAM due to deformation is difficult.

   These unexpected fracture bands are found to be caused by preferential crack propagation along martensitic bands across the cross-section of the tensile specimens. They are located around the centerline of the specimen, originating at the short edge of the specimen. This is caused by the presence of martensite grains at the short edge surface layer due to EDM, compared to a ferrite surface layer present at the long edge, causing preferential nucleation in the martensite grains. The easier crack nucleation in and propagation along the martensitic grains are facilitated by the HEDE and HELP HE mechanisms.

From the research done in this thesis project new insights are gained on the nature of varying martensite contents on the microstructure and HE of DP steels. Dilatometry is proven as an effective method for the development of new heat treatment methods to create DP steels. Increasing martensite contents changes the microstructure from a distribution of martensite grains and islands within a ferrite matrix, to ferrite grains within a martensite matrix. This increase severely affects the HE behavior of the DP steel, with increasing martensite content causing increasing embrittlement. Furthermore, the importance of surface conditions on the nucleation of cracks in an HE environment is documented as crucial for the observed HE behavior.

The use of DP steels as safety critical components in vehicles highlight the importance of understanding the severe effect of HE when creating stronger DP steels to reduce material usage. Ensuring a ferritic surface layer can make crack nucleation at the surface harder, and avoiding the creation of martensitic bands can decrease crack propagation, thus reducing the HE.

In addition to the main conclusions relating to the research objective, the following conclusions are made from this thesis project:

1. Heat treatment involving high austenization temperatures (1000 $°C$), cause a decrease in the A_r intercritical range, causing an unwanted overlap between the ferrite and pearlite formation ranges. This limits the possible austenization temperatures to create a homogeneous austenite distribution.

2. When estimating the martensite content, SEM tends to overestimate the martensite content, while EBSD underestimates it, OM lies between these two and is closest to the average.

3. During SSRT there is hysteresis of the polymer components of the tensile setup, which is different in the benchmarking and HE case. This affects the estimation of the engineering stress-strain curve. However, during estimation this is accounted for resulting in an accurate fracture point on the curve.

4. Interrupted SSRT is only viable when there is significant plastic deformation across the specimen, and not possible when embrittlement is too high. EBSD of an area close to the fracture surface can be used as an alternative to see stress localization in the material. However, there is an upper bound on the martensite content for effective characterization of strain localization due to deformation rather than the presence of martensite.

6 Outlook and Recommendations

To further investigate this research topic, the following outlooks on the next steps for the further development of the work initiated in this thesis are made:

1. Investigate the diffusion of hydrogen through the material, using a permeation cell. However, care must be given to the microstructure and orientation, since ferrite acts as fast diffusion channels, and the banding of the microstructure can affect this.
2. Increasing the austenization time for experiments to further investigate the effect of austenization time on the rolled microstructure. Increasing the austenization temperature is not recommended.
3. Investigating heat treatments developed from the A_c region, to compare with the microstructure obtained in the A_r region.
4. Further investigate the effect of surface microstructure conditions on crack initiation and growth, due to HE. It is shown to be vital for the fracture of the specimen in HE, and therefore requires more attention. Evaluate whether the martensite surface layer can be removed with localized heat treatment. Heat treatment after creating the double neck is not recommended, as it was seen to have a large thermal gradient and limited homogenous zone in the appendix.
5. SSRT HE testing with a submersible extensometer should be carried out to verify the validity of the estimation method of the extensometer stress-strain curves of the HE affected specimens.
6. TDS should be attempted with larger specimens, to verify the obtained total hydrogen contents.

In addition to the outlook, the following recommendations are made for the practical aspects of investigating the effect of heat treatment on the microstructure and HE of steels:

1. A dedicated heat treatment setup for tensile specimens should be developed and built, able to heat treat entire tensile specimens, avoiding the need for a double-neck and increasing the heat-treated zone. This could be accomplished by creating a custom design based on the dilatometry, using induction coils to heat the entire specimen in an atmosphere controlled chamber able to hold vacuum and quench the specimen.
2. Interrupted SSRT does not give any comparable results when the specimen does not achieve significant plastic deformation. Investigation of fractured specimens some distance to the fracture edge could be used as an alternative when there is no significant plastic deformation across the entire specimen gauge, although with a too high martensite content strain localization due to deformation becomes indistinguishable from that of the martensite grains.

References

[1] United Nations Environment Programme. (2015). *Paris Agreement*. Retrieved 9th January 2024, from https://wedocs.unep.org/20.500.11822/20830

[2] GroenvermogenNL. (2023). *What we do*. Retrieved 15th December 2023, from https://groenvermogennl.org/en/about-groenvermogennl/what-we-do/

[3] De Rijksoverheid. (2023). *GroenvermogenII (onderdeel van GroenvermogenNL)*. Retrieved 15th December 2023, from https://www.nationaalgroeifonds.nl/overzicht-lopende-projecten/thema-energie-en-duurzame-ontwikkeling/groenvermogen-ll

[4] European Parliament. (2023). *CO2 emissions from cars: facts and figures (infographics)*. Retrieved 9th January 2024, from https://www.europarl.europa.eu/news/en/headlines/society/20190313STO31218/co2-emissions-from-cars-facts-and-figures-infographics

[5] Tisza, M., & Lukács, Z. (2018). High strength aluminum alloys in car manufacturing. *IOP Conference Series: Materials Science and Engineering*, *418*.

[6] Hilditch, T. B., de Souza, T., & Hodgson, P. D. (2015). Properties and automotive applications of advanced high-strength steels (AHSS). In M. Shome & M. Tumuluru (Eds.), *Welding and Joining of Advanced High Strength Steels (AHSS)* (pp. 9–28).

[7] Daimler, J. W., Heibel, S., Winzer, J., Hilpert, B., Gao, Q., Dettinger, T., & Wortberg, D. (2017). Lightweight car body construction with new high strength steels. *SCT2017 5th International Conference on Steels in Cars and Trucks*.

[8] Sezgin, C. T., & Hayat, F. (2020). The Microstructure and Mechanical Behavior of TRIP 800 and DP 1000 Steels Welded by Electron Beam Welding Method. *Soldagem & Inspeção*, *25*, e2526.

[9] Horvath, C. D. (2020). Advanced steels for lightweight automotive structures. *Materials, Design and Manufacturing for Lightweight Vehicles*, 39–95.

[10] Lovicu, G., Bottazzi, M., D'aiuto, F., Sanctis, M. D., Dimatteo, A., Santus, C., & Valentini, R. (2012). Hydrogen embrittlement of automotive advanced high-strength steels. *Metallurgical and Materials Transactions A: Physical Metallurgy and Materials Science*, *43*, 4075–4087.

[11] Johnson, W. H. (1875). On Some Remarkable Changes Produced in Iron and Steel by the Action of Hydrogen and Acids. *Proceedings of the Royal Society of London*, *23*, 168–179.

[12] Cora, Ö. N., & Koç, M. (2014). Promises and Problems of Ultra/Advanced High Strength Steel (U/AHSS) Utilization in Auto Industry. *7th Automotive Technologies Congress*.

[13] Tisza, M. (2021). Three Generations of Advanced High Strength Steels in the Automotive Industry. *Lecture Notes in Mechanical Engineering*, *22*, 81–94.

[14] Dhaher, N. (2019). The Iron–Carbon System. In *Materials Science and Engineering* (pp. 163–178).

[15] Bhadeshia, H. K. D. H., & Honeycombe, R. W. K. (2017a). Iron-Carbon Equilibrium and Plain Carbon Steels. In *Steels: Microstructure and Properties* (4th ed., pp. 59–100).

[16] Bhadeshia, H. K. D. H., & Honeycombe, R. W. K. (2017b). Formation of Martensite. In *Steels: Microstructure and Properties* (4th ed., pp. 135–177).

[17] Koistinen, D., & Marburger, R. (1959). A General Equation Prescribing the Extent of the Austenite-Martensite Transformation in Pure Iron-Carbon Alloys and Plain Carbon Steels. *Acta Metallurgica*, *7*, 59–60.

[18] Reddy, K. S., Govindaraj, Y., & Neelakantan, L. (2022). Influence of microstructure on the hydrogen diffusion behavior in dual-phase steels: an electrochemical permeation study. *Journal of Materials Science*, *57*, 19592–19611.

[19] Adamczyk, J., & Grajcar, A. (2006). Effect of heat treatment conditions on the structure and mechanical properties of DP-type steel Manufacturing and processing. *Journal of Achievments in Materials and Manufacturing Engineering*, *17*, 305–308.

[20] Khorasani, F., Jamaati, R., & Jamshidi Aval, H. (2023). Effect of Intercritical Annealing Time on the Microstructure and Mechanical Properties of Dual-Phase Steel Processed by Large-Strain Asymmetric Cold-Rolling. *Steel research international*, *94*(9), 2300086.

[21] Andrews, K. W. (1965). Heat Treatment for Improvement in Low Temperature Mechanical Properties of 0.40 pct C-Cr Steels. *The Journal of the Iron and Steel Institute*, *207*, 721–727.

[22] Bilir, O., & Erisir, E. (2014). Effect of austenization temperature and time on dual phase microstructure for a medium carbon dual phase steel. *VIth International Metallurgical Congress*.

[23] Wang, Z., Liu, J., Huang, F., Bi, Y. J., & Zhang, S. Q. (2020). Hydrogen Diffusion and Its Effect on Hydrogen Embrittlement in DP Steels With Different Martensite Content. *Frontiers in Materials*, *7*.

[24] Rudomilova, D., Prošek, T., Salvetr, P., Knaislová, A., Novák, P., Kodým, R., Schimo-Aichhorn, G., Muhr, A., Duchaczek, H., & Luckeneder, G. (2020). The effect of microstructure on hydrogen permeability of high strength steels. *Materials and Corrosion*, *71*, 909–917.

[25] Wasim, M., Djukic, M. B., & Ngo, T. D. (2021). Influence of hydrogen-enhanced plasticity and decohesion mechanisms of hydrogen embrittlement on the fracture resistance of steel. *Engineering Failure Analysis*, *123*.

[26] Drexler, A., Helic, B., Silvayeh, Z., Mraczek, K., Sommitsch, C., & Domitner, J. (2022). The role of hydrogen diffusion, trapping and desorption in dual phase steels. *Journal of Materials Science*, *57*, 4789–4805.

[27] Schwartz, A. J., Kumar, M., Adams, B. L., & Field, D. P. (2009). Present State of Electron Backscatter Diffraction and Prospective Developments. In *Electron Backscatter Diffraction in Materials Science* (2nd ed., pp. 1–20).

[28] Rodoni, E., Verbeken, K., Depover, T., & Iannuzzi, M. (2023). Effect of microstructure on the hydrogen embrittlement, diffusion, and uptake of dual-phase low alloy steels with varying ferrite-martensite ratios. *International Journal of Hydrogen Energy*.

[29] Barrera, O., Bombac, D., Chen, Y., Daff, T. D., Galindo-Nava, E., Gong, P., Haley, D., Horton, R., Katzarov, I., Kermode, J. R., Liverani, C., Stopher, M., & Sweeney, F. (2018). Understanding and mitigating hydrogen embrittlement of steels: a review of experimental, modelling and design progress from atomistic to continuum. *Journal of Materials Science*, *53*, 6251–6290.

[30] Lynch, S. P. (2011). Hydrogen embrittlement (HE) phenomena and mechanisms. In V. S. Raja & T. Shoji (Eds.), *Stress corrosion cracking: Theory and practice* (pp. 90–130).

[31] Truschner, M., Trautmann, A., & Mori, G. (2021). The Basics of Hydrogen Uptake in Iron and Steel. *BHM Berg- und Hüttenmännische Monatshefte*, *166*, 443–449.

[32] Marcus, P. (2011). *Corrosion Mechanisms in Theory and Practice* (3rd ed.).

[33] Turnbull, A. (2012). Hydrogen diffusion and trapping in metals. In R. P. Gangloff & B. P. Somerday (Eds.), *Gaseous Hydrogen Embrittlement of Materials in Energy Technologies* (pp. 89–128, Vol. 1).

[34] Mehrer, H. (2007). Diffusion in Solids. In *Springer Series in Solid-State Sciences* (pp. 28–53, 127–149).

[35] Djukic, M. B., Zeravcic, V. S., Bakic, G. M., Sedmak, A., & Rajicic, B. (2015). Hydrogen damage of steels: A case study and hydrogen embrittlement model. *Engineering Failure Analysis*, *58*, 485–498.

[36] Li, Z., Shi, J., Fan, Y., Ma, C., Dong, X., Guo, C., & Zhao, H. (2024). The effect of intercritical annealing time on the hydrogen embrittlement of dual-phase steel. *Materials Today Communications*, *38*, 108328.

[37] Pfeil, L. B. (1926). The Effect of Occluded Hydrogen on the Tensile Strength of Iron. *Proceedings of the Royal Society of London Series A*, *112*(760), 182–195.

[38] Troiano, A. (1959). The role of hydrogen and other interstitials in the mechanical behavior of metals. *Trans ASM*, *52*, 147–157.

[39] Beachem, C. D. (1972). New model for hydrogen-assisted cracking (hydrogen embrittlement). *Metallurgical and Materials Transactions A*, *3*.

[40] Lynch, S. P. (2003). Mechanisms of hydrogen assisted cracking – a review. In N. Moody, A. Thompson, R. Ricker, G. Was & R. Jones (Eds.), *Hydrogen effects on materials behavior and corrosion deformation interactions* (pp. 449–466).

[41] Clum, J. A. (1975). The role of hydrogen in dislocation generation in iron alloys. *Scripta Metallurgica*, *9*(1), 51–58.

[42] Zhao, Y., Seok, M. Y., Choi, I. C., Lee, Y. H., Park, S. J., Ramamurty, U., Suh, J. Y., & Jang, J. I. (2015). The role of hydrogen in hardening/softening steel: Influence of the charging process. *Scripta Materialia*, *107*, 46–49.

[43] Carrillo-Bucio, J. L., Tena-Garcia, J. R., Armenta-Garcia, E. P., Hernandez-Silva, O., Cabañas-Moreno, J. G., & Suárez-Alcántara, K. (2018). Low-cost Sieverts-type apparatus for the study of hydriding/dehydriding reactions. *HardwareX*, *4*, e00036.

[44] Ehrlin, N., Bjerkén, C., & Fisk, M. (2016). Cathodic hydrogen charging of Inconel 718. *AIMS Materials Science*, *3*, 1350–1364.

[45] Faucon, L. E., Boot, T., Riemslag, T., Scott, S. P., Liu, P., & Popovich, V. (2023). Hydrogen-Accelerated Fatigue of API X60 Pipeline Steel and Its Weld. *Metals*, *13*.

[46] Wang, M., Akiyama, E., & Tsuzaki, K. (2005a). Crosshead speed dependence of the notch tensile strength of a high strength steel in the presence of hydrogen. *Scripta Materialia*, *53*, 713–718.

[47] Wang, M., Akiyama, E., & Tsuzaki, K. (2005b). Effect of hydrogen and stress concentration on the notch tensile strength of AISI 4135 steel. *Materials Science and Engineering: A*, *398*, 37–46.

[48] Merson, E., Kudrya, A. V., Trachenko, V. A., Merson, D., Danilov, V., & Vinogradov, A. (2016). Quantitative characterization of cleavage and hydrogen-assisted quasi-cleavage fracture surfaces with the use of confocal laser scanning microscopy. *Materials Science and Engineering: A*, *665*, 35–46.

[49] Rudomilova, D., Prošek, T., & Luckeneder, G. (2018). Techniques for investigation of hydrogen embrittlement of advanced high strength steels. *Corrosion Reviews*, *36*, 413–434.

[50] Vucko, F., Ootsuka, S., Rioual, S., Diler, E., Nazarov, A., & Thierry, D. (2022). Hydrogen detection in high strength dual phase steel using scanning Kelvin probe technique and XPS analyses. *Corrosion Science*, *197*.

[51] Zhao, T., Liu, Z., Hu, S., Du, C., & Li, X. (2017). Effect of Hydrogen Charging on the Stress Corrosion Behaviour of 2205 Duplex Stainless Steel Under 3.5 wt.% NaCl Thin Electrolyte Layer. *Journal of Materials Engineering and Performance*, *26*, 2837–2846.

[52] Ozdirik, B., Baert, K., Depover, T., Vereecken, J., Verbeken, K., Terryn, H., & Graeve, I. D. (2017). Development of an Electrochemical Procedure for Monitoring Hydrogen Sorption/Desorption in Steel. *Journal of The Electrochemical Society*, *164*, C747–C757.

[53] Maixent, M., & Bercot, P. (2011). Electrochemical Analysis of Thiourea on Platinum in Non-Aqueous Electrolyte. *International journal of electrochemical science*, *6*, 1007–1013.

[54] Fuji, H., Fujishiro, T., & Hara, T. (2021). Effect of Ammonium Thiocyanate on Hydrogen Entry Behavior of Low Alloy Steel under Galvanostatic Cathode Charging. *ISIJ International*, *61*, 1151–1158.

[55] Queiroga, L. R., Marcolino, G. F., Santos, M., Rodrigues, G., Eduardo dos Santos, C., & Brito, P. (2019). Influence of machining parameters on surface roughness and susceptibility to hydrogen embrittlement of austenitic stainless steels. *International Journal of Hydrogen Energy*, *44*(54), 29027–29033.

[56] Verbeken, K. (2012). Analysing hydrogen in metals: bulk thermal desorption spectroscopy (TDS) methods. In R. P. Gangloff & B. P. Somerday (Eds.), *Gaseous Hydrogen Embrittlement of Materials in Energy Technologies* (pp. 27–55, Vol. 1).

[57] Koyama, M., Rohwerder, M., Tasan, C. C., Bashir, A., Akiyama, E., Takai, K., Raabe, D., & Tsuzaki, K. (2017). Recent progress in microstructural hydrogen mapping in steels: quantification, kinetic analysis, and multi-scale characterisation. *Materials Science and Technology (United Kingdom)*, *33*, 1481–1496.

[58] Escobar, P., Duprez, L., Atrens, A., & Verbeken, K. (2014). Influence of experimental parameters on thermal desorption spectroscopy measurements during evaluation of hydrogen trapping. *Journal of Nuclear Materials*, *450*(1), 32–41.

[59] Wang, D., Hagen, A. B., Fathi, P. U., Lin, M., Johnsen, R., & Lu, X. (2022). Investigation of hydrogen embrittlement behavior in X65 pipeline steel under different hydrogen charging conditions. *Materials Science and Engineering: A*, *860*.

[60] ASTM International. (2021). *Standard Practice for Slow Strain Rate Testing to Evaluate the Susceptibility of Metallic Materials to Environmentally Assisted Cracking* (Standard No. G129-21). American Society for Testing and Materials.

[61] ASTM International. (2022a). *Standard Test Method for Determination of Susceptibility of Metals to Embrittlement in Hydrogen Containing Environments at High Pressure, High Temperature, or Both* (Standard No. G142-98(2022)). American Society for Testing and Materials.

[62] Boot, T., Riemslag, T. A., Reinton, E. T., Liu, P., Walters, C. L., & Popovich, V. (2021). In-situ hollow sample setup design for mechanical characterisation of gaseous hydrogen embrittlement of pipeline steels and welds. *Metals*, *11*.

[63] Martin, M. L., Fenske, J. A., Liu, G. S., Sofronis, P., & Robertson, I. M. (2011). On the formation and nature of quasi-cleavage fracture surfaces in hydrogen embrittled steels. *Acta Materialia*, *59*(4), 1601–1606.

[64] Ashrafi, H., Shamanian, M., Emadi, R., & Ghassemali, E. (2020). Void Formation and Plastic Deformation Mechanism of a Cold-Rolled Dual-Phase Steel During Tension. *Acta Metall. Sin. (Engl. Lett.)*, *33*, 209–306.

[65] Drexler, A., Domitner, J., & Sommitsch, C. (2021). Modeling of hydrogen diffusion in slow strain rate (SSR) testing of notched samples. In V. A. Polyanskiy & A. K. Belyaev (Eds.), *Advances in hydrogen embrittlement study* (143rd ed., pp. 87–111).

[66] Takashima, K., Nishimura, T., Yokoyama, K., & Funakawa, Y. (2019). Role of Interface between Ferrite and Martensite in Hydrogen Embrittlement Behavior of Ultra-high Strength Dual-phase Steel Sheets. *ISIJ International*, *59*(9), 1676–1682.

[67] ASTM International. (2022b). *Standard Test Methods for Tension Testing of Metallic Materials* (Standard No. E8/E8M-22). American Society for Testing and Materials.

[68] Collins, J., Stavrina & Pickering, E. (2023). Steel Dilatometry Analysis (v2.0). https://doi.org/10.5281/zenodo.7763330

Appendices

A Supporting Python Code - All Data Analysis

This appendix includes all the python code used for data analysis, including the analysis of the dilatometry curves to find the critical transformation temperatures, estimation of the HE extensometer SSRT stress-strain curve and calculation of the total absorbed hydrogen content for TDS.

Dilatometry Curve Analysis

```
###Dilatometry Curve Creator###
###This progamme can be used to create and analyse curves created for dilatometry based on the .asc source file###

import numpy as np
import pandas as pd
import matplotlib.pyplot as plt

###Inputs###

###Function Definition###

##Estimating the critical transformation temperature##
def line_fitting(file,L0,N,M,label_name,critical_T,T1,T2,tol,section,state):
    # file = Input filepath with / instead of \ to indicate path
    # L0 = Input initial length of sample in meters
    # N = Input starting row index to isolate parts of the curve for specialized plots (0 indicate start at begining)
    # M = Input end row index to isloate parts of the curve for specialiazed plots (-1 indicate all points)
    # label_name = Input indicated label name
    # T1 = Input lower temperature value for creation of the fitted line
    # T2 = Input upper temperature value for the creation of the fitted line (T2>T1)
    # tol = Input tolerance value determining at which point fitted line deviates from dilatometry curve
    # section = 'upper' or 'lower' Input which section of plot to be considered in the specified section
    # state = 'heating' or 'cooling' Input which state the experiment is in, in the specified section

    # read data in file
    data = pd.read_csv(file, delimiter = r"\s+", header = None, skiprows=4, engine='python',encoding= 'unicode_escape')
    # isolate the colums related to 'Temperature' & 'Change in Length'
    for n in range(len(data.columns)):
        if n == 2 or n == 3:
            pass
        else:
            del data[n]
    data.columns = ['T', 'x']

    # calculate strain using initial length (L0)
    data['e'] = (data['x']*10**(-6))/L0
    # isolate curve from data
    rds = data[N:M] #rds = relevant data set

    #Find index of the specified temperatured
    dx1 = (np.zeros(len(rds)-1))
```

```
    dx2 = (np.zeros(len(rds)-1))

    for i in range(len(rds)-1):
        dx1[i] = abs((rds.iat[i,0]-T1))
        dx2[i] = abs((rds.iat[i,0]-T2))

    i1 = np.argmin(dx1)
    i2 = np.argmin(dx2)

    #Create extrapolation line

    X1 = (rds.iat[i2,1]-rds.iat[i1,1])/(rds.iat[i2,0]-rds.iat[i1,0])
    Y1 = (rds.iat[i1,0]*X1)

    line = np.zeros(len(rds))

    for i in range(len(rds)):
        x = (rds.iat[i,0]*X1)-(Y1-rds.iat[i1,1])
        line[i] = x

    # calculate strain using initial length (L0)
    line_e = (line*10**(-6))/L0

    ###Determination of critical temperature
    ic=0

    if section == 'upper' and state == 'heating':
        #only selecting section greater than T2 temperature during cooling
        dev = np.zeros(len(rds)-i2)
        rds_section = rds[i2:]
        line_e_section = line_e[i2:]

        dev = (line_e_section-rds_section['e'])
        deviation = dev.to_numpy() #convert from dataframe to array
        #finding critical index
        for i in range(len(deviation)):
            if deviation[i]>tol:
                ic=i+i2
                break


    if section == 'lower'and state == 'heating':
        #only selecting section lower than T1 temperature during heating
        dev = np.zeros(i1)
        rds_section = rds[:i1]
        line_e_section = line_e[:i1]

        dev = (rds_section['e']-line_e_section)
        deviation = dev.to_numpy() #convert from dataframe to array
        #finding critical index
        for i in range(len(deviation)):
            if deviation[i]<tol:
                ic=i
                break

    if section == 'lower' and state == 'cooling':
        #only selecting section lower than T1 temperature during cooling
        dev = np.zeros(i1)
        rds_section = rds[i1:]
        line_e_section = line_e[i1:]

        dev = (rds_section['e']-line_e_section)
        deviation = dev.to_numpy() #convert from dataframe to array
```

```
        #finding critical index
        for i in range(len(deviation)):
            if deviation[i]>tol:
                ic=i+i1
                break

    if section == 'upper' and state == 'cooling':
        #only selecting section greater than T2 temperature during cooling
        dev = np.zeros(len(rds)-i2)
        rds_section = rds[:i2]
        line_e_section = line_e[:i2]

        dev = (line_e_section-rds_section['e'])
        deviation = dev.to_numpy() #convert from dataframe to array
        #finding critical index
        for i in range(len(deviation)):
            if deviation[i]<tol:
                ic=i
                break

    Tc = rds.iat[ic,0]
    ec = rds.iat[ic,2]

    return Tc,ec
```

SSRT HE Extensometer Stress-Strain Estimation

```
### SSRT Tensile Curves ###
### This code estimated the extensometer stress-strain curve for the SSRT HE specimens
import numpy as np
import matplotlib.pyplot as plt
import pandas as pd
import sympy as sp
from scipy.stats import linregress
pd.options.mode.chained_assignment = None  # default='warn'

### Basic Curve Creation ###
### This funtion reads the input .csv datafile and calculates the stress, extenosmeter and nominal strains, as well as the difference between the latter, storing it all in a dataframe for further processing
def SSRT_file_reader(file, label, width, thickness, gauge_length_extenso):
    # file = Input filepath with / instead of \ to indicate path
    # label_name = Input sample label name

    # read data in file
    data = pd.read_csv(file, delimiter = r";", header = None, engine='python', encoding= 'unicode_escape', skiprows=3)
    data.columns = ['Time','Force','Strain','Standard_travel','Nominal_strain']

    cross_section = width * thickness

    data['Stress'] = np.nan
    data['Strain_extenso'] = np.nan
    data['Strain_nominal'] = np.nan
    data['Strain_diff'] = np.nan

    data['Stress'] = data['Force']/cross_section

    data['Strain_extenso'] = data['Strain']/gauge_length_extenso

```

```
    data['Strain_nominal'] = data['Nominal_strain']/10 ##Nominal Strain of entire gauge length is 10 in the double-necked area

    data['Strain_diff'] = data['Strain_nominal'] - data['Strain_extenso']

    return data

### Third order polynomial fitting ###
### This funtion uses the fitted third order polynomial (from Excel) and applies it to a HE curve, estimating the HE extensometer stress-strain curve.
def apply_third_order_polynomial(df, a, b, c, d, benchmark_df):
    """
    Applies a third-order polynomial transformation to a specified column in the DataFrame.

    Parameters:
    df (pd.DataFrame): The input DataFrame.
    column_name (str): The name of the column to be transformed.
    a (float): The coefficient for the x^3 term.
    b (float): The coefficient for the x^2 term.
    c (float): The coefficient for the x term.
    d (float): The constant term.

    Returns:
    pd.DataFrame: The DataFrame with the transformed values in the specified column.
    """
    df['real_root'] = a * df['Force']**3 + b * df['Force']**2 + c * df['Force'] + d
    df['adjusted_root'] =  df['Strain_nominal'] - df['real_root']

    diff = []
    for i in range(len(df)):
        change = benchmark_df['Strain_nominal'].iloc[i]-df['Strain_nominal'].iloc[i]
        diff.append(change)

    df_diff = pd.DataFrame(diff, columns=['Diff'])

    df['adjusted_root'] = df['adjusted_root']+ df_diff['Diff']

    # Find the index of the maximum value in the specified column
    max_index = df['Force'].idxmax()

    # Calculate the index to truncate at (max_index + 2)
    truncate_index = max_index + 4

    # Truncate the DataFrame
    df = df.iloc[:truncate_index + 1]

    return df

### Calculating the Embrittlement Index ###
### This function calculates the embrittlement index of the benchmarking and HE stress-strain curves.
def calculate_embrittlement_index(benchmark_df, embrittlement_dfs):
    """
    Calculates the embrittlement index for three embrittlement-affected DataFrames compared to a benchmarking DataFrame.

    Parameters:
    benchmark_df (pd.DataFrame): The benchmarking DataFrame.
    embrittlement_dfs (list of pd.DataFrame): List containing three embrittlement-affected DataFrames.
```

```
    Returns:
    list of float: The embrittlement indices for the three affected DataFrames.
    """
    # Get the last value of the benchmarking DataFrame
    index_B = benchmark_df.index[-1]
    benchmark_value = benchmark_df.loc[index_B, 'Strain_extenso']

    embrittlement_indices = []

    # Calculate the embrittlement index for each affected DataFrame
    for embrittlement_df in embrittlement_dfs:
        index_df = embrittlement_df['Stress'].idxmax() ##Takes the strain value at the highest stress value as it fractures instantly
        affected_value = embrittlement_df.loc[index_df, 'adjusted_root']
        embrittlement_index = (benchmark_value - affected_value) / benchmark_value
        embrittlement_indices.append(embrittlement_index)

    return embrittlement_indices
```

TDS H Content Calculation

```
### TDS Plotter ###
### This code inputs a .csv data file containing the desorbed hydrogen per second, outputting a dataframe with timestamps and the calculated total hydrogen content
import numpy as np
import matplotlib.pyplot as plt
import pandas as pd
pd.options.mode.chained_assignment = None  # default='warn'

###
def process_dataframe(file, mass, cal_factor, label):
    """
    Calculates the total hydrogen content

    Parameters:
    file: Inputted .csv datafile containing TDS data
    mass: Recorded mass of specimen in g
    cal_factor: Calibration factor from the TDS device
    label: Specimen label

    Returns:
    data: The processed DataFrame with added timestamps for plotting
    ppm: The total H content in wppm
    """

    # read data in file
    data = pd.read_csv(file, delimiter = r";", header = None, skiprows=15, engine='python',encoding= 'unicode_escape')

    # isolate colums related to 'Time' and 'Temperature'
    for n in range(len(data.columns)):
        if n == 1 or n == 6:
            pass
        else:
            del data[n]
    data.columns = ['Temperature', 'Hydrogen (low)']

    # Remove rows with any NaN values in the original DataFrame
    data.dropna(inplace=True)

```

```
    # Add new 'Time' column with 0.2 seconds increment
    data['Time'] = [(0.2 * (i + 1))-0.2 for i in range(len(data))]
    min_value = data['Hydrogen (low)'].min()
    data['Baseline'] = min_value

    # Perform difference calculation
    # Start with constants
    SampleMass = mass
    Adoption = 20000000 #This is for the hydrogen low sensor only. Other adoption factors are in the manual.

    # Calculate the Difference and Integral
    data['Difference'] = data['Hydrogen (low)'] - data['Baseline']
    data['Difference'] = data['Difference'].apply(lambda x: x if x >= 0 else 0)  # Replace negative values with 0
    Integral = data['Difference'].sum()  # Sum of the positive differences
    print(Integral)

    # Calculate the total Hwppm of Difference
    ppm = (Integral * cal_factor) / (Adoption * SampleMass)
#    print(label,"ppm:", ppm)

    # Calculate the H wppmps column
    data['H_wppmps'] = (data['Difference'] * cal_factor * 5) / (Adoption * SampleMass)

    return data, ppm
```

B Case study - Tensile Specimen Heat-Treatment Selection

This short case study highlights the selection procedure to decide the heat treatment method for the tensile specimen. Three options were possible, a Nabertherm oven, the Bruker G8 Galileo IR furnace, and the Gleeble 3800-GTC, thus promoting the comparison and selection of the ideal one. Based on the initial comparison, the Gleeble was chosen as the optimal method. Following this multiple possible tensile specimen designs were examined in the Gleeble to find the optimal one used in this thesis project. A list of requirements that must be met by the technique was defined The table used for the initial comparison of the three heat treatment options is given in Figure B.1.

Nabertherm N11/HR/B400	Bruker G8 Galileo IR Oven	Gleeble 3800-GTC
• Can heat-treat entire specimen • Multiple samples at one time • Use retort or metals bags - Flush with N or Ar	• Can heat-treat entire specimen • Control of atmosphere using N gas • Can mimic dilatometry heating rates • Can plot thermal data	• Control of atmosphere using vacuum • Complete control of thermal cycle (heating, cooling, quenching) • Can mimic dilatometry heat and cooling rates • Can plot thermal data
• Dilatometry heating/cooling rates not achievable • Thermocouple placed next to heating element, not on specimen • Limited control over quenching process	• One specimen at the time • Cannot have control cooling • Thermocouple distanced from specimen • Limited possibility of quenching	• One specimen at the time • Limited homogenous heat-treated zone (10 mm)

Figure B.1: Table of the initial comparison between the three heat treatment methods, comparing their benefits (upper row) and drawbacks (lower row).

From the comparison table, it is clear that the Nabertherm oven and Bruker IR furnace are less ideal than the Gleeble, as they lack the same control of the heat treatment process, with different heating, cooling and quenching possibilities. However, for further testing both the Bruker IR furnace and the Gleeble were selected and tested with trial specimens. For all these trial experiments the obtained data consisted of heat treatments, measuring the recorded temperature of the specimen as a function of time. Two trials were conducted for the Bruker IR furnace trials, one with the controlling thermocouple above the specimen, and one below the thermocouple, close to the heating element. An external thermocouple was placed on the specimen to record the actual temperature experienced by the specimen and verify the correct temperatures are reached in the heat treatment. These are given in Figure B.2.

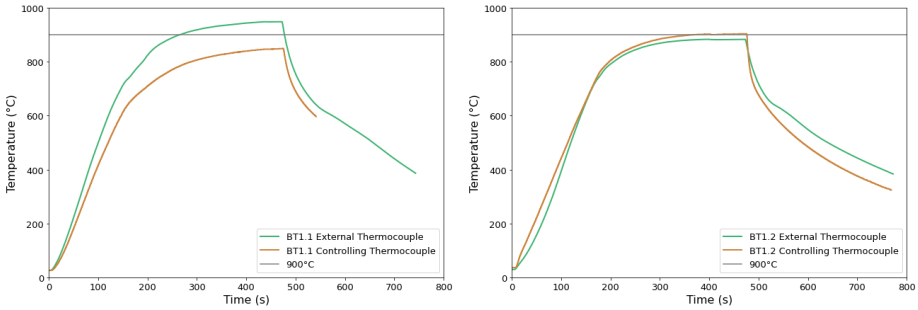

(a) (b)

Figure B.2: Temperature development during trial heat treatment of specimens in the Bruker IR furnace when a) the thermocouple is above the specimen and b) the thermocouple is below the specimen, close to the heating element.

As clearly seen in the figure, there is a mismatch between the controlling and external thermocouple. For the case where the thermocouple is placed above the specimen, Figure B.2a, the furnace does not reach the temperature set, 900 $°C$, to austenize the steel. However, the recorded thermocouple records temperature exceeding the 900 $°C$ austenization temperature. For the case the controlling thermocouple is paced under the specimen, close to the heating element, the 900 $°C$ temperature is reached. Here, the external thermocouple on the specimen reports slightly lower temperatures than the controlling thermocouple, but with a much lower difference. For both specimens, however, there is a non-linear heating rate, and uncontrolled cooling after heat treatment. These observations make the Bruker IR furnace not applicable for the controlled heat treatment of tensile specimen, and the Gleeble becomes the only remaining options. To find the optimal specimen design multiple specimens were made and heat treated in the gleeble. These specimens are shown in Figure B.3, with the corresponding temperature development given in Figure B.4.



(a) (b) (c) (d) (e)

Figure B.3: Various Designs for Gleeble Trial Specimens, were a), b) has a double-neck to localize the heat treated zone, c), d) has protrusions outside the double-necked area to increase the change in cross-section area, and e) increase the cross-section areas, providing heat from multiple sources.

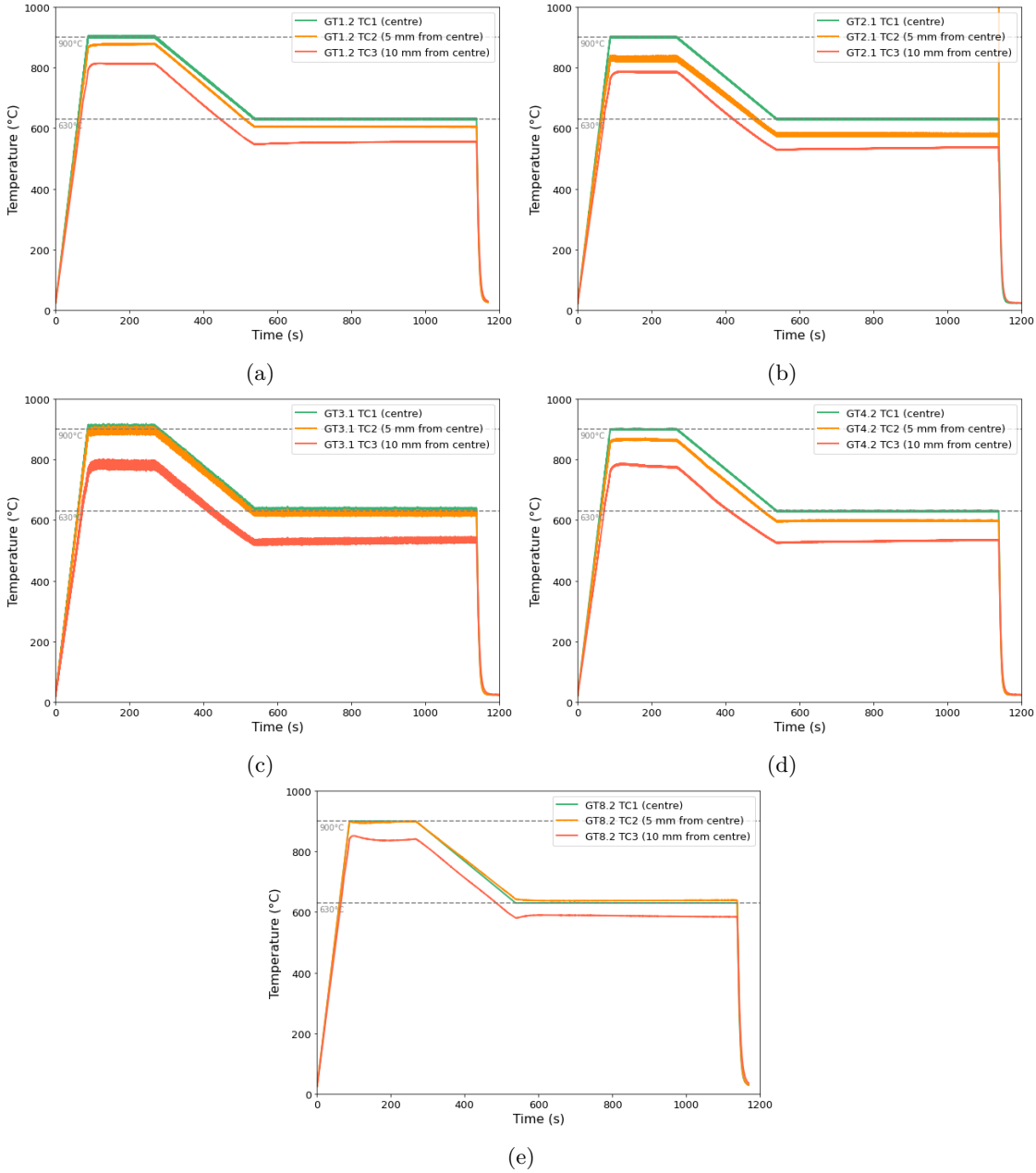

Figure B.4: Temperature development during trial heat treatment of specimens in the Gleeble, evaluating different specimen designs. a), b), c), d) and e) correspond to Figure B.3 a), b), c), d), and e) respectively.

As seen in the figures, the following conclusions can be drawn. Comparing Figures B.4a) and b), a larger cross-section area in the center results in a reduced temperature drop, when comparing the thermocouple placed in the center of the specimen and 5 *mm* from the center of the specimen. The same is seen in Figures B.4c) and e). Based on these observations, the final specimen design of a single necked and the post heat treatment EDM to create a double neck was chosen. The temperature development for the trial specimen of the final design is given in Appendix F.

C Supporting Figures - Critical Temperature Determination

The method for the determination of the critical transformation temperatures is exemplified in Figure C.1, where the point at which the change in length deviates from the slope (tangent) is found for all relevant critical transformation temperatures for this specimen. These points are seen in the overview image of the entire dilatometry curve, showing each point at its location.

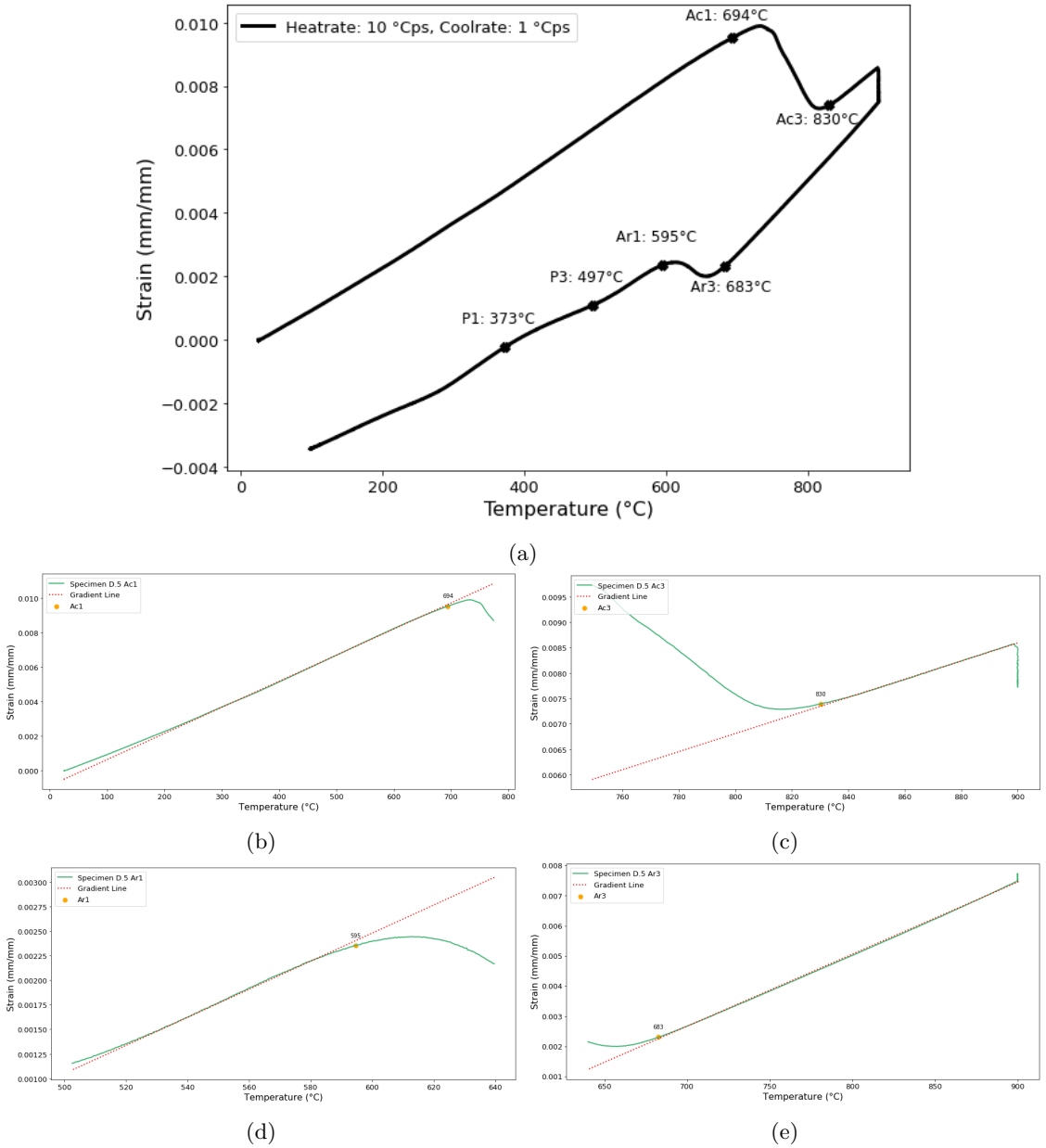

Figure C.1: Determination of critical transformation temperatures from the dilatometry curve. a) shows an overview image of each identified point and b)-e) shows how each individual point was found, not including the final pearlite transformation present during the heat treatment.

For all specimens tested and heat treated with dilatometry, the critical transformation temperatures were determined. These are given in Figure C.2 for the specimens that are not presented in Section 4.1. Intercritical annealing at 820 $°C$ and 720 $°C$ in the A_c region during cooling (Figures C.2b

and C.2c) were conducted to evaluate whether any phase transformation occurred, as only the A_c temperatures are reported in literature. However, this is not expected, as the A_r region is lower than the A_c region. It is evident that no phase transformation occurred during cooling and holding at the temperatures in the A_c intercritical region (820 $°C$ and 720 $°C$). The only phase transformation occurs is the martensite formation during quenching. Therefore, it is expected that these dilatometry specimens only contain martensite, not producing a DP microstructure.

For the two additional specimen intercritically annealed in the A_r region, at 610 $°C$, 630 $°C$ and 650 $°C$, Figures C.2d, C.2f and C.2e respectively there are two phase transformations occurring for the samples. The first, at a higher temperature during cooling, is the formation of ferrite, while the second is the martensite formation from the remaining austenite. This indicates that these heat treatments result in a DP structure. For all dilatometry curves, there is some deviation in the intensity of the martensite formation curve, further indicating that it is possible to qualitatively assess the martensite content of the resulting microstructure.

The effect of intercritical annealing time on the dilatometry curve is seen in Figures C.2g, C.2f, and C.2h. All the curves are similar and there is little indication of any major differences in the dilatometry curves. This indicates that the intercritical annealing time is less important than the intercritical annealing temperature on the resulting martensite content.

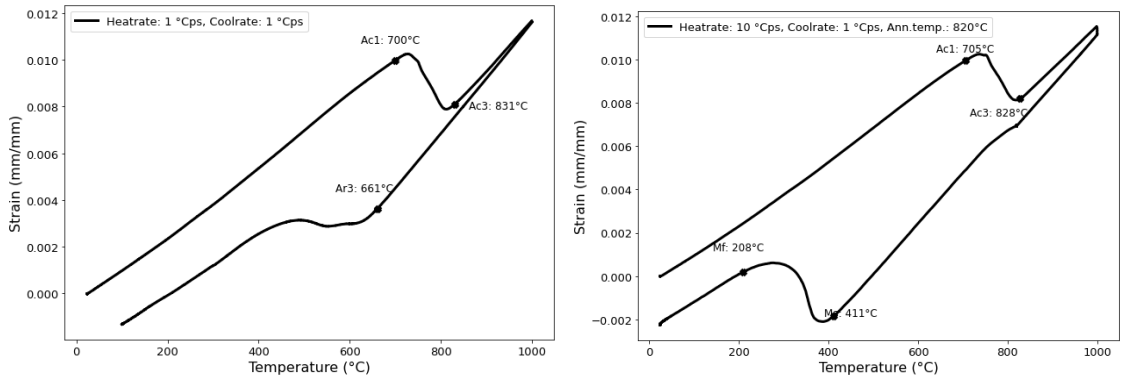

(a)

(b)

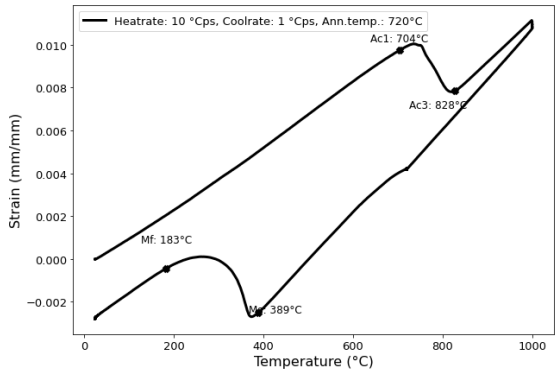

(c)

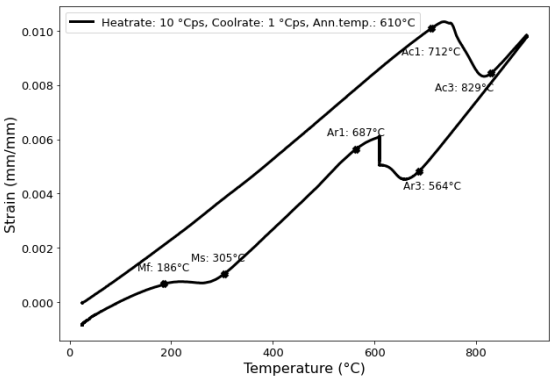

(d)

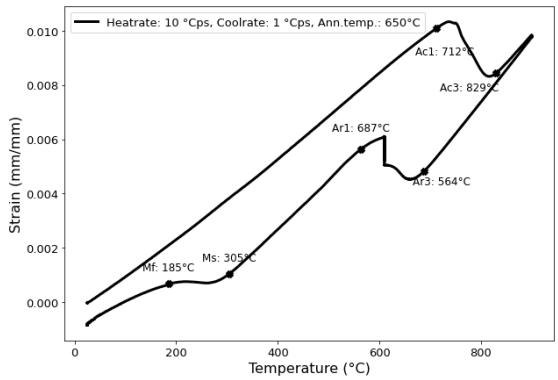

(e)

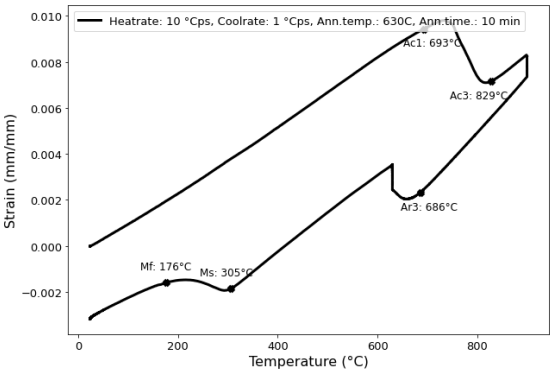

(f)

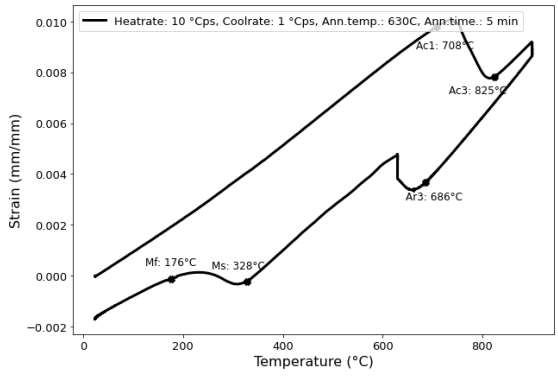

(g)

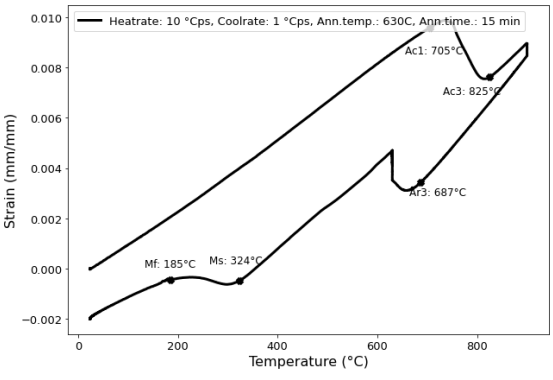

(h)

Figure C.2: Determination of critical transformation temperatures

D Supporting Figures - Quantitative and Qualitative Microstructure Analysis

Here supporting figures for the quantitative martensite content estimation and qualitative microstructure investigation are shown. First, this includes the comparison of martensite contents for each of the estimation methods, SEM, OM, and EBSD, for the intercritical annealing conditions not presented in Section 4.2.1, at 610 $°C$, 630 $°C$, and 650 $°C$. For SEM this is given in Figure D.1, for OM in Figure D.2, and for EBSD in Figure D.3.

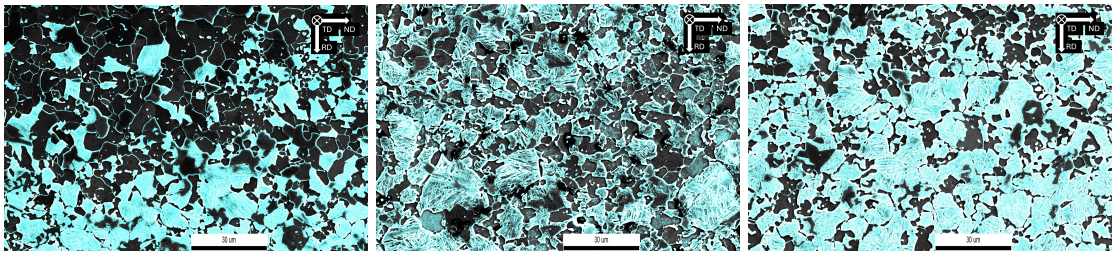

(a) (b) (c)

Figure D.1: Estimated martensite content from SEM with magnification 1000x, for dilatometry specimens, with increasing intercritical annealing temperature of a) 610 $°C$, b) 630 $°C$, and c) 650 $°C$. The martensite content is depicted as the cyan overlay in the images. There is an increase in martensite content as intercritical annealing temperature increase.

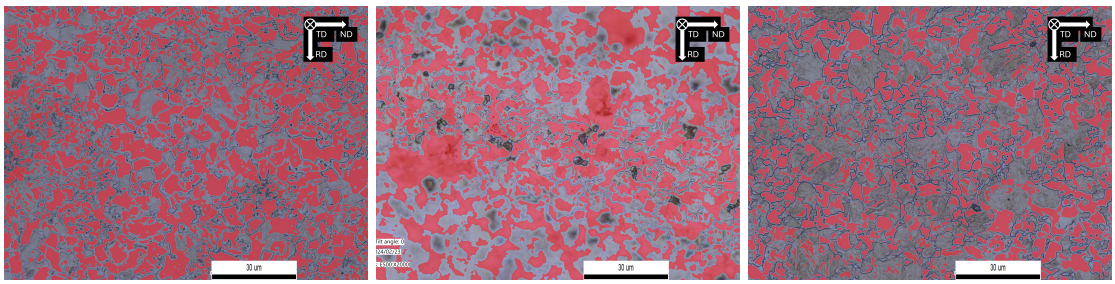

(a) (b) (c)

Figure D.2: Estimated ferrite content from OM with magnification 2000x, for dilatometry specimens, with increasing intercritical annealing temperature of a) 610 $°C$, b) 630 $°C$, and c) 650 $°C$. Ferrite is indicated by the red overlay in the images. There is a decrease in ferrite content as intercritical annealing temperature increase, causing an increase in martensite content.

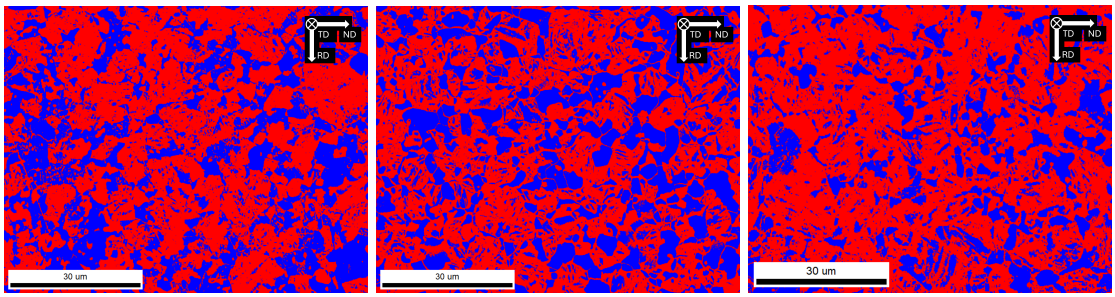

(a) (b) (c)

Figure D.3: Estimated martensite content from EBSD analysis, for dilatometry specimens, with increasing intercritical annealing temperature of a) 610 $°C$, b) 630 $°C$, and c) 650 $°C$. The red phase indicates areas with a low image quality, indicating martensite, while the blue has a high image quality, indicating ferrite. There is an increase in martensite content as intercritical annealing temperature increase.

As with the figures above, the effect of intercritical annealing time is estimated, and the average martensite content with increasing intercritical annealing time is reported. Figure D.4 shows the estimation of martensite content from SEM images of the specimens intercritically annealed for 5 and 15 minutes, which are given in Figure D.5 for the OM images. The intercritical annealing for 10 minutes is given in the previous figures as the 630 $°C$ intercritical annealing condition (Figures D.1b and D.2b for the SEM and OM image respectively).

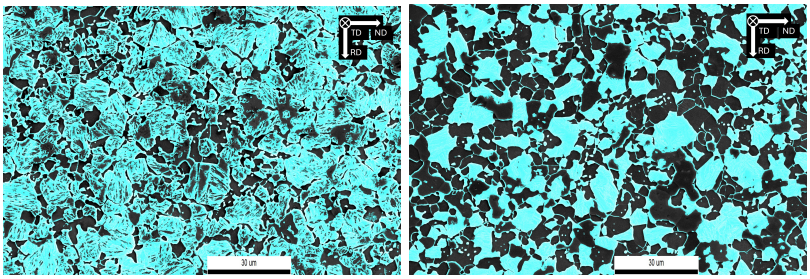

(a) (b)

Figure D.4: Estimated martensite content from SEM with magnification 1000x, for dilatometry specimens, with intercritical annealing time of a) 5 mins and b) 15 mins. The martensite content is depicted by the cyan overlay in the images.

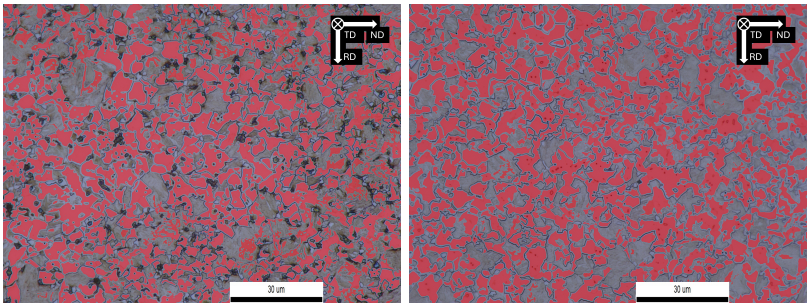

(a) (b)

Figure D.5: Estimated ferrite content from OM with magnification 2000x, for dilatometry specimens, with intercritical annealing time of a) 5 mins and b) 15 mins. Ferrite is indicated by the red overlay in the images.

The additional qualitative SEM analysis of the dilatometry specimens include the magnification of 300x of the specimens not analyzed in Section 4.2.2, which includes the specimens intercritically annealed at 610 $°C$, 630 $°C$, and 650 $°C$, as well as an annealing time of 5, 10, and 15 minutes.

Figure D.6, shows overview SEM images of the specimen intercritically annealed at 610 $°C$ and 650 $°C$ respectively.

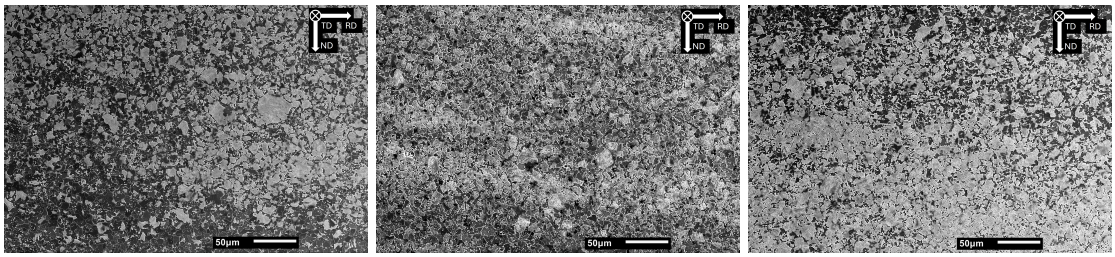

(a) (b) (c)

Figure D.6: Overview SEM images at magnification 300x of specimens intercritically annealed at 610 $°C$, 630 $°C$, and 650 $°C$. The lighter phase indicates martensite, while the dark phase indicates ferrite. A slight increase in martensite content is seen at the higher intercritical annealing temperatures

In Figure D.6, there is a distinguishable difference in the obtained martensite content. As expected, as 610 $°C$ there is less martensite present than at 650 $°C$, being intercritically annealed at a lower temperature. Additionally, the clusters of martensite are more dispersed in Figure D.6, when compared to that of Figure 27b, containing almost exclusivity martensite.

The effect of intercritical annealing time is seen in Figure D.7. Comparing specimen D.11 and D.12, a lower intercritical annealing time contains a seemingly slightly higher martensite content. This indicates that the martensite content decreases as intercritical annealing time increases, due to the phase transformation from austenite to ferrite occurring. With a low annealing time, the equilibrium martensite/ferrite ratio is not reached, and less austenite is transformed to ferrite, thus giving more martensite. However, the effect of time is less noticeable than the effect of temperature.

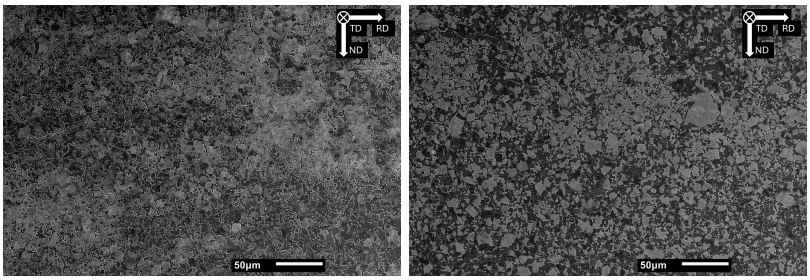

(a) (b)

Figure D.7: Overview SEM images at magnification 300x of specimens with different intercritical annealing times, a) 5 and b) 15 minutes respectively. The lighter phase indicates martensite, while the dark phase indicates ferrite.

E Supporting Figures - Dilatometry and Tensile Specimen Comparison

The supporting figures for the dilatometry and tensile specimen comparison include the measured hardness profiles and additional SEM comparison images. Hardness measurements were taken from one Gleeble tensile specimen and one dilatometry specimen for the three intercritical annealing conditions used in the Gleeble heat treatment. Furthermore, the hardness values obtained are compared to that of the as-received material. The qualitative SEM analysis was done on one dilatometry specimen and one Gleeble tensile specimen, to evaluate if any change in the nature of the martensite phase exist with the different heat treatment techniques.

Figure E.1 show the measured hardness across the centerline of the dilatometry (yellow) and Gleeble (blue) specimen, measured at increments of 1 mm, extending out from the center of the specimen. Additionally, the hardness of the as-received materials is given as the dashed line (black) for comparison. In the figures, there are vertical dashed lines to indicate the 10 mm double-necked gauge area that was cut after the heat treatment of the tensile specimen. Only the relevant area is given for the Gleeble specimens, to compare with the dilatometry specimens, with the full curves of the Gleeble specimens given in Appendix F.

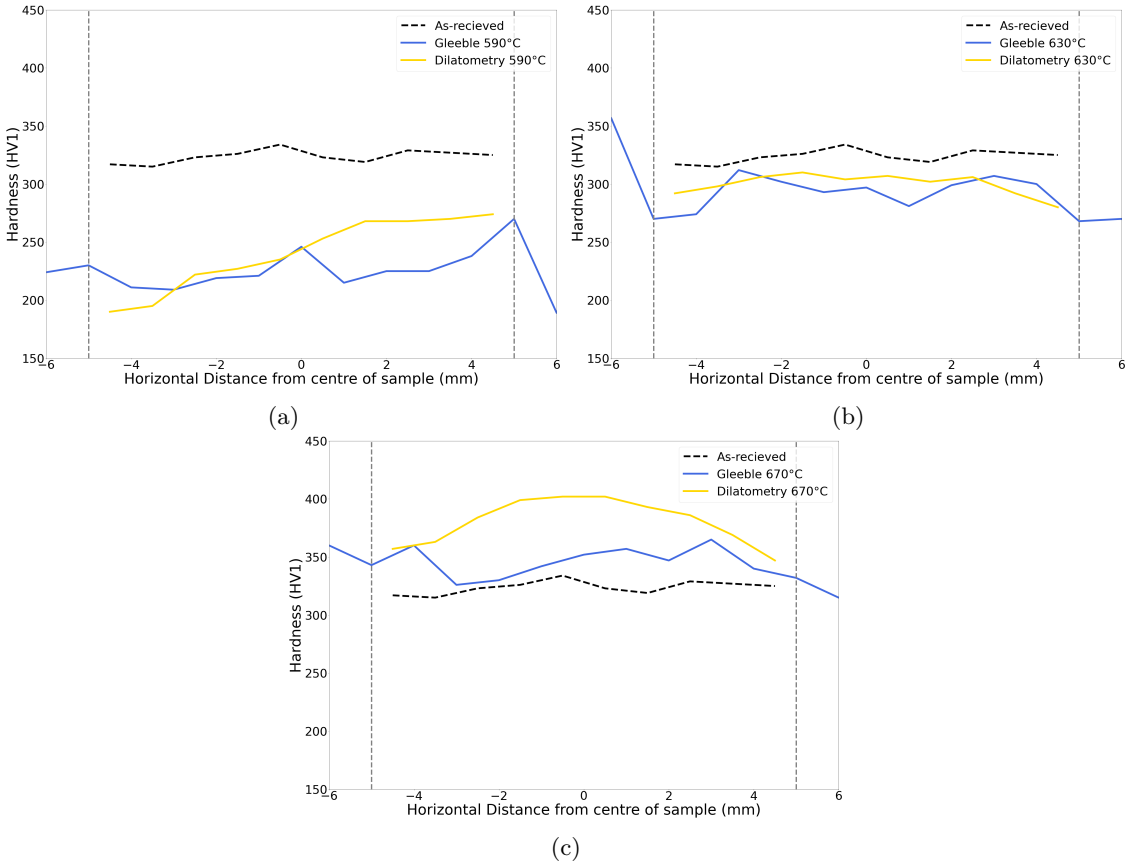

Figure E.1: Obtained HV1 hardness profile for the specimens heat treated in the dilatometer (yellow) and the Gleeble (blue) showing the development of hardness across the centerline along the length of the specimens, for the different intercritical annealing conditions. The dashed line (black) indicate the hardness of the as-received material. The vertical dashed lines (gray) indicate the boundaries of the double-necked area.

As seen in Figure E.1, in the 10 mm gauge area of the tensile specimens the hardness remain stable,

without significant variation. Furthermore, compared to the dilatometry specimen, the hardness is similar for all intercritical annealing conditions. At an intercritical annealing temperature of 590 $°C$ and 630 $°C$ there is an overlap in the measured hardness values of the dilatometer specimen and for the Gleeble specimens. For the 670 $°C$ specimen, the hardness profile of the dilatometry specimen increases towards the center of the specimen, and is above the Gleeble specimen for at all points. Outside the 10 mm gauge of the Gleeble specimen, seen in Appendix F, there is a significant immediate drop in hardness outside, before it increases towards the as-received material hardness. This indicates a different heat treatment has occurred in the area outside the gauge, due to a high thermal gradient in the Gleeble. Figure 30 compares the average hardness values obtained in the gauge area, with those previously obtained for the dilatometry specimens as a function of intercritical annealing temperature, which is quantified in Table 14. Furthermore, the estimated martensite content as a function of intercritical annealing temperature is present, to evaluate the accuracy of using hardness to estimate the martensite content.

As seen in the comparison in Figure 30 the obtained hardness values are very similar, following the same trends. For all temperatures, the hardness of the Gleeble specimens remain lower than that of dilatometry. For the 590 $°C$ intercritical annealing condition, the hardness is the same for dilatometry and for the Gleeble, at 240 ± 31 $HV1$ and 238 ± 25 $HV1$ respectively. At 630 $°C$ this difference increases to 300 ± 9 $HV1$ for the dilatometry specimen and 286 ± 13 $HV1$ for the Gleeble case. At 670 $°C$, the difference is largest, at 380 ± 20 $HV1$ for the dilatometry specimen, and 344 ± 12 $HV1$ for the Gleeble one. However, for both Gleeble and dilatometry specimens, there is an uncertainty in the between the hardness values. As the measured hardness value depend on where in the microstructure an indent is made, the obtained hardness value can significantly deviate if the specimen is particularly textures.

Additionally, there are differences in the fundamental part of each heat treatment technique, which can cause the small differences in the absolute hardness values. Specifically, the dilatometry specimens are smaller and quenched using helium while the Gleeble specimens are large tensile specimens quenched using pressurized air. The quenching of dilatometry specimens were observed to be slightly quicker than the tensile ones, with a higher quenching rate. This impacts the formation of martensite, although this is expected not significantly impact the martensite content. Furthermore, with longer quenching times there is more time for carbon diffusion out of the martensite phase, which decreases the hardness of the martensite phase. This explains the greater difference in hardness as intercritical annealing temperature increases, since more martensite is present. Additionally, dilatometry heats the samples using an induction coil, while the Gleeble utilizes resistance heating. This impacts the heat distribution over time, and a minute delay in achieving a uniform heat distribution across the 10 mm gauge is to be expected.

Comparing the Gleeble tensile specimen to the as-received specimen hardness, intercritical annealing at 590 $°C$ and 630 $°C$ result in a lower hardness, decreasing to 238 ± 25 $HV1$ and 286 ± 13 $HV1$ respectively. At 670 $°C$ there is a slight increase in hardness value to 344 ± 12 $HV1$. The difference in hardness indicate there is a difference in martensite content compared to the AR-specimen, with it being lower in the 590 $°C$ and 630 $°C$ intercritical annealing conditions and increased for the 670 $°C$ case.

To further validate the similar martensite content and to evaluate any difference in the microstructure with the two different heat treatment methods, Figure E.2 shows comparison SEM images of the microstructure of the dilatometry and Gleeble specimen. Additional images comparing the dilatometry and Gleeble heat treated specimens can be found in Appendix E.

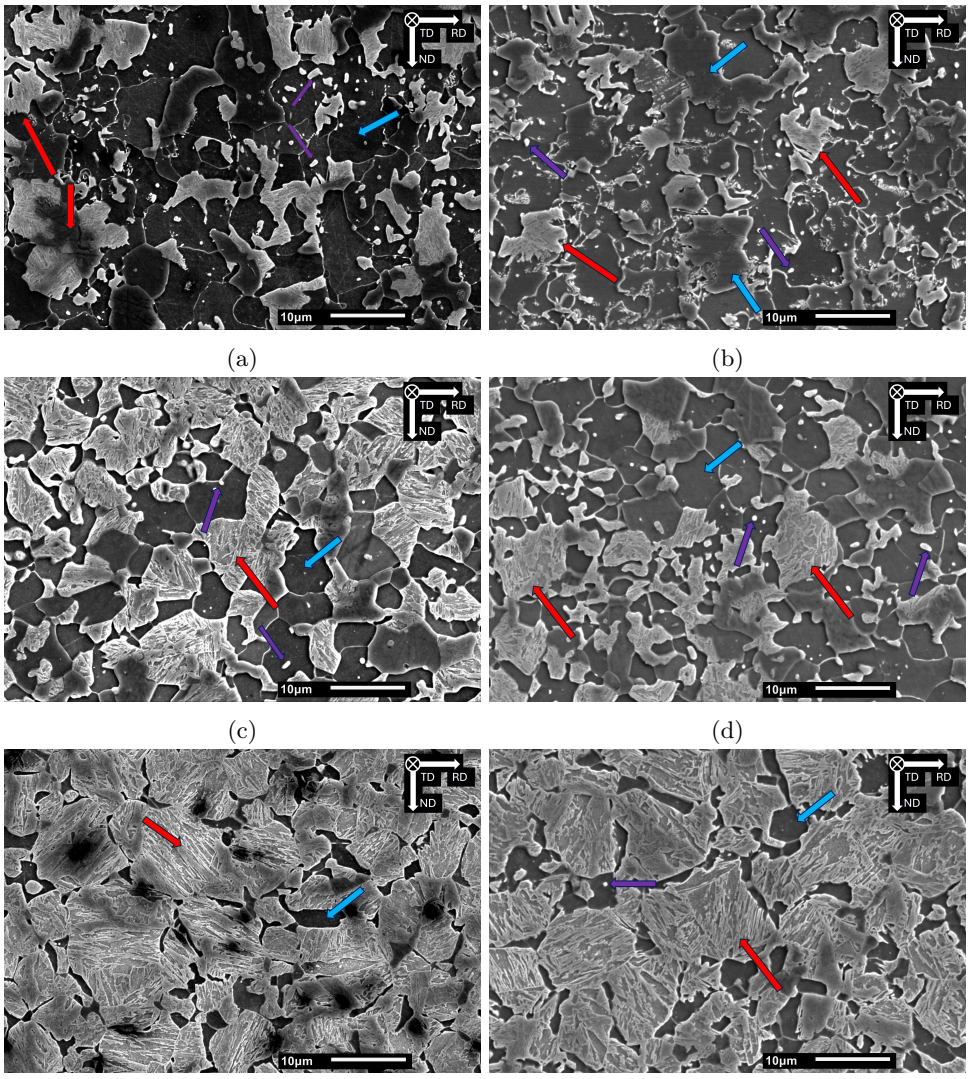

Figure E.2: SEM images taken at a 2000x magnification of the a), c), e) dilatometry and b), d), f) gleeble specimen at intercritical annealing at a), b) 590 $°C$, c), d) 630 $°C$, and e), f) 670 $°C$. Martensite grains (red arrows) and islands (purple arrows) are depicted lighter than the dark ferrite phase (blue arrows).

As seen in Figure E.2 for the same microstructure is present when comparing the dilatometry and Gleeble heat treated specimens. For the 590 $°C$ specimen the martensite content is the similar, with a small increase in martensite islands. Additionally, the martensite lath grains are in some location broken up for the Gleeble specimen, compare with the full martensite lath grains for the dilatometry specimen.

With increasing intercritical annealing temperature, to 630 $°C$ the martensite phase is more similar to the dilatometry specimen counterpart. Furthermore, there is a noticeable increase of martensite islands within the ferrite grains. Furthermore, there is a concentration of martensite on the lower left side of the Gleeble 630 $°C$ specimen (Figure E.2d), indicating a continued presence of banding in the Gleeble specimens.

The microstructures for intercritical annealing at 670 $°C$ are the most similar. There is no distinguished difference in the martensite phase content and grain size. However, some martensite islands are found in ferrite grains, but not to a significant extent. As for the dilatometry specimen,

this indicates that the ferrite grains are too small to accommodate and form martensite islands during quenching.

Figures E.3–E.5 show selected comparison SEM images of various locations in and outside the 10 *mm* gauge area, as well as with SEM images obtain for the dilatometry specimens. Since the purpose of the SEM investigation is to validate that the heat treatment in the *Gleeble 3800-GTC* thermo-mechanical simulator is similar to that of the dilatometer, in the 10 *mm* gauge area, these images are of specific interest. The images captured outside the 10 *mm* gauge are given in Appendix F, as they are not relevant in the comparison between Gleeble and dilatometry specimens.

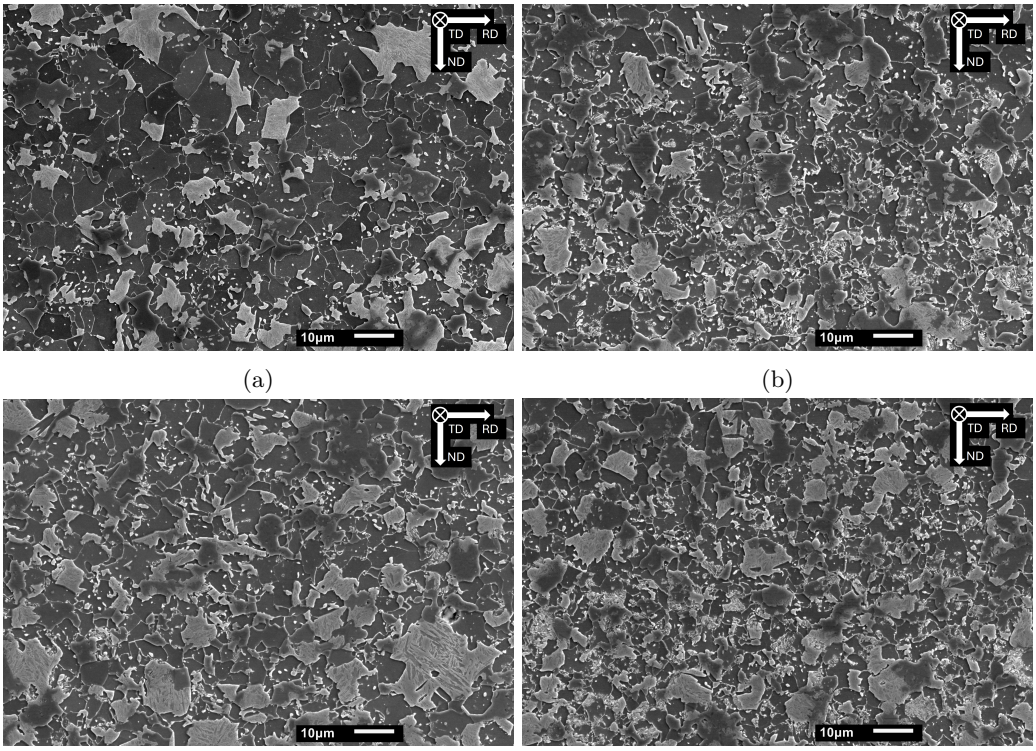

Figure E.3: SEM images taken at a 1000x magnification of the a) dilatometry specimen and b)-d) various locations of the tensile specimen intercritically annealed at 590 $°C$ comparing different locations of specimen produced with the Gleeble and the dilatometry specimen. Martensite is depicted as lighter than the dark ferrite phase.

As seen in the Figure E.3, there is a similar microstructure present across the entirety in of the GT590 specimen. Furthermore, compared to the dilatometry specimen, the martensite content is similar. All SEM images contain larger martensite grains dispersed with a surrounding ferrite matrix, with multiple small martensite islands within the ferrite grains. There is an increase in smaller martensite islands within the ferrite matrix in the GT590 specimen, across the entire gauge (Figures E.3b–E.3d), compared to the dilatometry specimen.

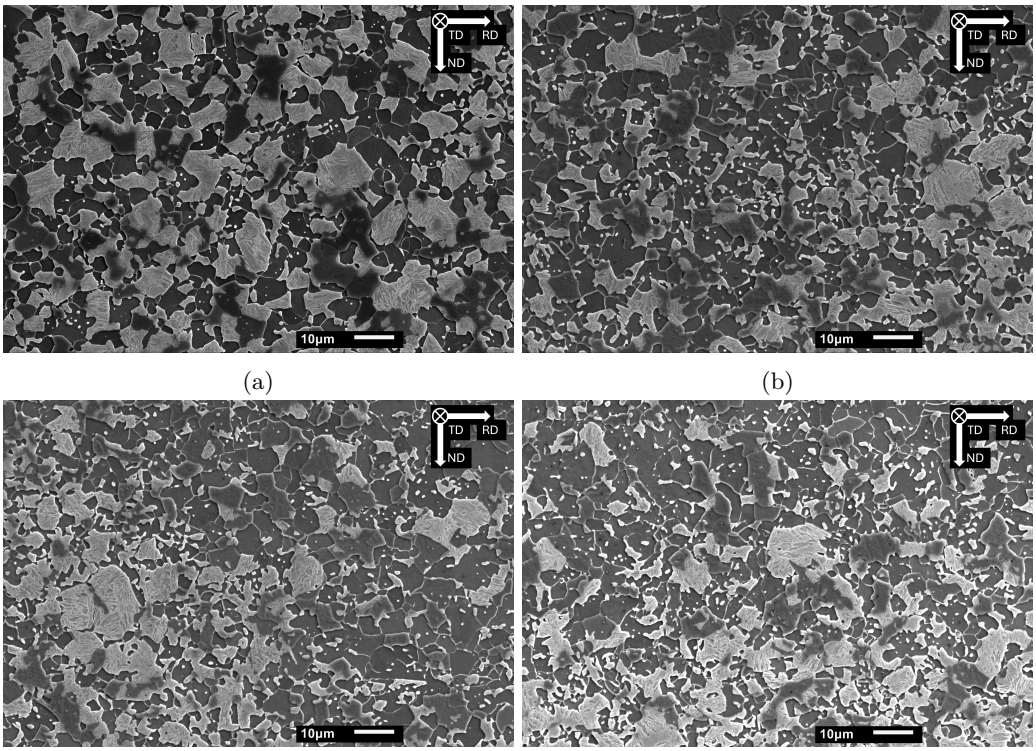

Figure E.4: SEM images taken at a 1000x magnification of the a) dilatometry specimen and b)-d) various locations of the tensile specimen intercritically annealed at 630 $°C$ comparing different locations of specimen produced with the Gleeble and the dilatometry specimen. Martensite is depicted as lighter than the dark ferrite phase.

For the GT590 specimen, seen in Figure E.4, a comparison similar to the GT590 specimen, between the dilatometry and Gleeble specimen can be made. The phase fraction of martensite and ferrite is the same, with similar grain sizes. Furthermore, while both Gleeble and dilatometry specimens contain martensite islands, there is a noticeable increase in martensite islands in the Gleeble specimen, compared with the dilatometry one. Furthermore, as exemplified by Figure E.4c, there is a presence of texture in the Gleeble specimens, since there is a concentration of martensite on one side of the SEM image, while the other side primarily contains ferrite.

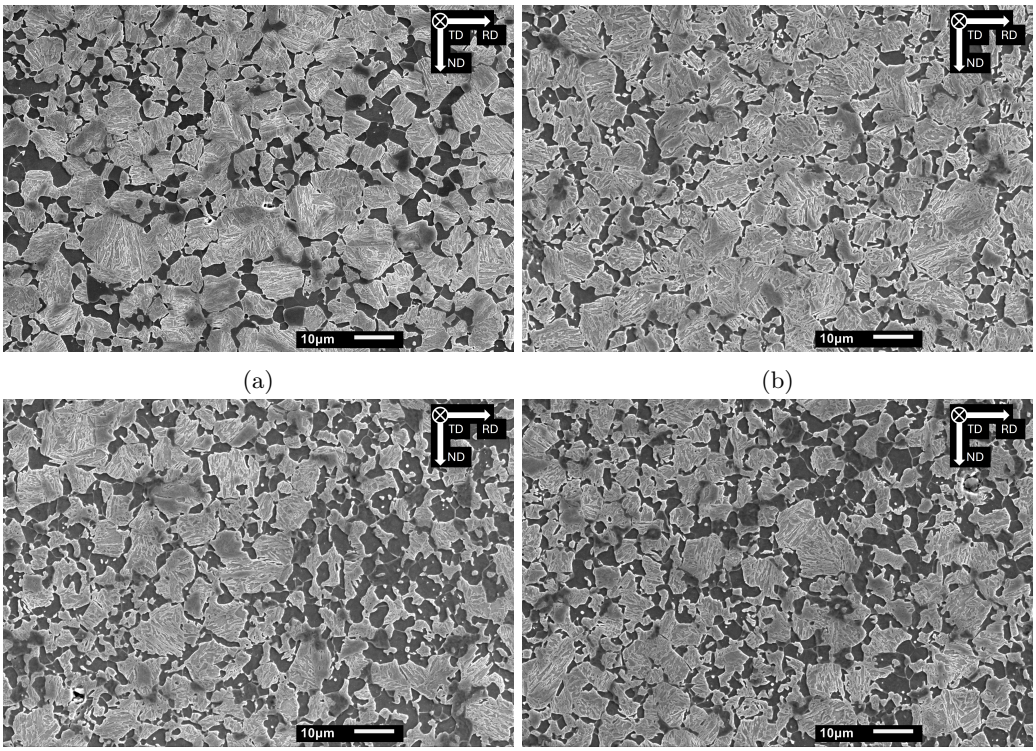

Figure E.5: SEM images taken at a 1000x magnification of the a) dilatometry specimen and b)-d) various locations of the tensile specimen intercritically annealed at 670 $°C$ comparing different locations of specimen produced with the Gleeble and the dilatometry specimen. Martensite is depicted as lighter than the dark ferrite phase.

Figure E.5 shows the comparison between dilatometry and the Gleeble produced specimens intercritically annealed at 670 $°C$. From the images there are clear similarities and the microstructure predominantly consists of martensite grains of similar grain sizes. In the dilatometry specimen, there are little to no martensite islands, which are more prevalent in the Gleeble specimen. Particularly, this is seen in Figures E.5c and E.5d. However, this is due to larger and more concentrated ferrite grain being present in the microstructure, when compared to the center specimen (Figure E.5b) and the dilatometry specimen (Figure E.5a).

Overall, the comparison between the dilatometry and Gleeble specimens, using hardness and SEM, yield that there is no significant difference between the two heat treatment techniques, and the Gleeble remains a viable method for the heat treatment of larger specimen in a manner possible for dilatometry. With this comparison the TDS, SSRT and fractographic results of Gleeble tensile specimen can be compared to the estimated martensite contents of the dilatometry heat treated specimens.

F Supporting Figures - Tensile Specimen Temperature Data and Hardness

The additional figures for the characterization of the tensile specimen include the temperature development at various locations on the specimen during heat treatment, and the hardness measurement outside the 10 mm gauge length area and the hardness across the width of the specimen

Temperature Development for Gleeble Tensile Specimen

The recording of the temperature development at various locations on the tensile specimens during heat treatment in the *Gleeble 3800-GTC* thermo-mechanical simulator are used to evaluate the area where the heat treatment is homogenous in the specimen. Figure F.1 show the recorded temperature at three different locations on the trial Gleeble specimens, one for the different intercritical annealing temperature. Specifically, the locations where thermocouples were attached were at the center of the specimen (the controlling thermocouple), 5 mm and 10 mm from the center of the specimen.

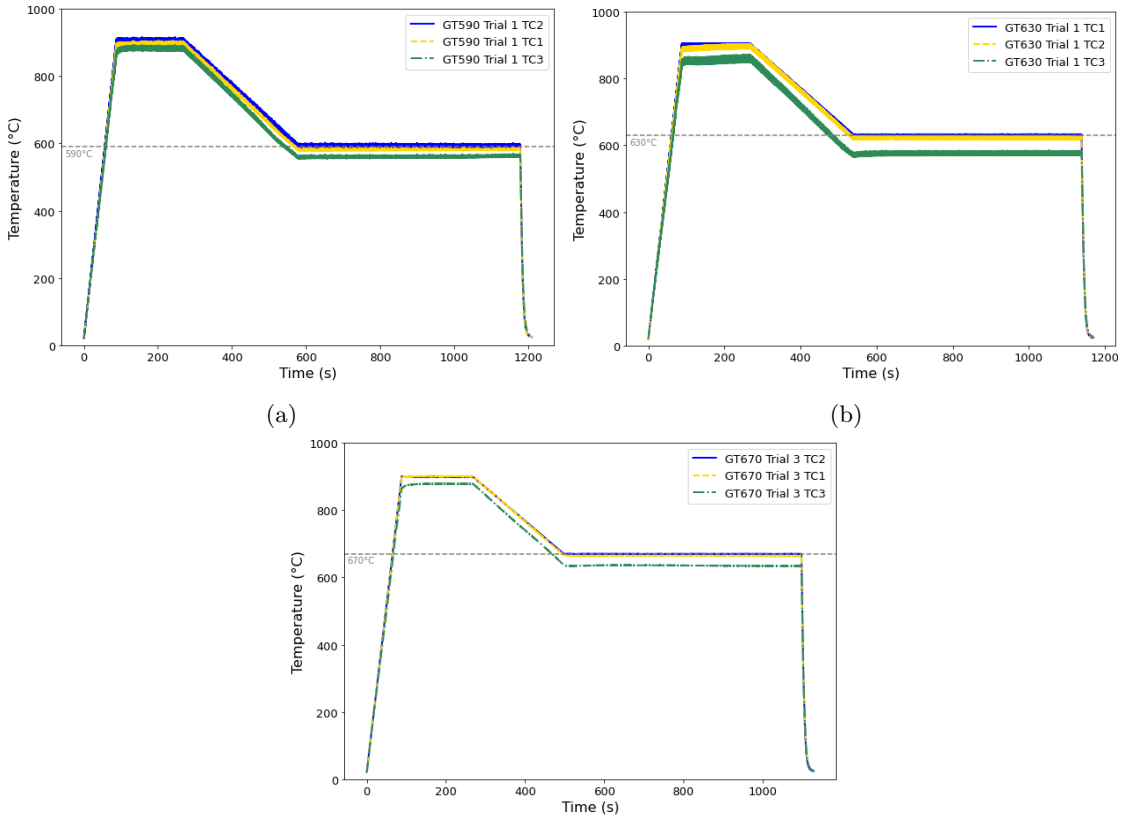

Figure F.1: Measured Temperature Profiles for the Gleeble trial specimens intercritically annealed at a) 590 $°C$, b) 630 $°C$, and c) 670 $°C$. The different lines indicate the controlling thermocouple in the center of the specimen, 5 mm from the center of the specimen and 10 mm from the center of the specimen. In b) and c) a non-controlling thermocouple were detached during the heat treatment, indicated by the instantaneous increase in temperature recorded.

As seen in Figure F.1, the thermocouples placed in the center of the specimen and 5 mm from the center of the specimen are indiscernible from each other, with an observed deviation in temperature

less than 5 $°C$. This indicates that in the 10 mm gauge of the specimen, the temperature can be assumed homogenous, meaning that the gauge area has undergone the same heat treatment across the entire area. Therefore, it can be assumed that the microstructure in this area is equal. The third thermocouple, placed 10 mm from the center of the specimen, records a lower temperature than the controlling one, reaching up to 50 $°C$ deviation for the specimen intercritically annealed at 670 $°C$. This indicates a sharp thermal gradient in the specimen. However, there is a trapezoidal like shape to the thermal gradient, where there is a flat homogenous plateau, with sharp decrease in temperature at the edges of this plateau.

Furthermore, in Figures F.1a and F.1b there is a much greater variance in the recorded temperature for all thermocouples than in Figure F.1c. This indicates that during some heat treatment procedures, the controlling program struggles to measure and adjust the temperature. Possible explanations for this include the quality of the thermocouple, the placement of the thermocouple wires and the quality of the thermocouple weld. It was during the trial experiments noticed, that with the multiple reuse of thermocouples, a greater variation in the recorded temperature occurred. With reuse of thermocouples, they might be bent or otherwise damages, giving inaccurate temperature readings. Additionally, thermocouples placed approximately 3 mm apart, on the same horizontal axis gave accurate readings, while if further or closer apart, or at a horizontal angle, gave greater variance. This is due to the thermocouple reading assuming the same temperature of the two wires, which during resistance heating occurs at the same vertical axis. For some trial specimens, a thermocouples broke during the heat treatment. This is an indication of a bad thermocouple weld, caused by either too low voltage, non-ideal surface roughness or a blunt thermocouple wire tip. However, for all trial specimens this occurred on a non-controlling thermocouple and thus not impacting the heat treatment procedure. Furthermore, a bad weld, caused by the aforementioned reasons, could increase the variance of the recorded temperature.

To avoid a large variation in the recorded temperature of the tensile specimen used for TDS and SSRT testing, the thermocouples were placed 3 mm apart, on the same vertical axis. The welding voltage was kept high (at 39), and each weld tip was cut at 45° to ensure a sharp tip before welding.

Tensile Specimen Hardness

Figure F.2 shows the measured hardness across the horizontal centerline of the specimen, measured at increments of 1 mm, extending out from the center of the specimen. In the figures, there are vertical dashed lines indicating the 10 mm double-necked gauge area that was cut after the heat treatment.

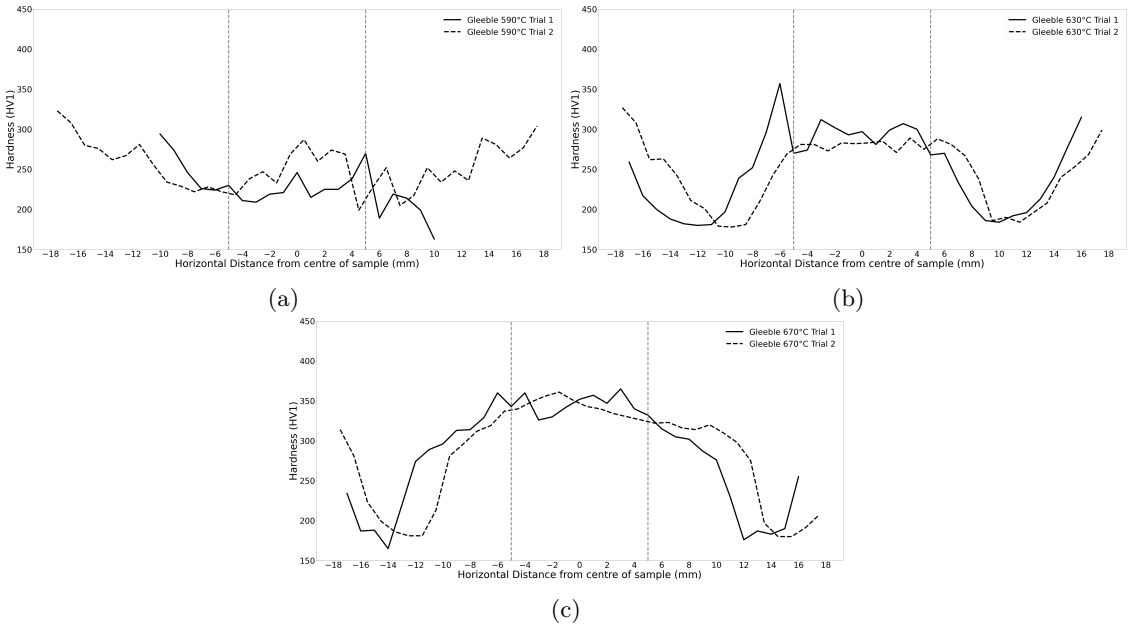

Figure F.2: Obtained HV1 hardness profile for trial tensile specimens heat treated in the *Gleeble 3800-GTC* thermo-mechanical simulator, showing the development of hardness as the distance from the center of the specimen increases in the horizontal direction. The gray dashed lines indicate the boundaries of the double-necked area.

As seen in Figure F.2, across the 10 mm horizontal gauge of the specimens the hardness remain stable, without major variation. For the specimens intercritically annealed at 590 $°C$, the average hardness in the gauge is 238 $HV1$, which increases to 286 $HV1$ and 344 $HV1$ for the specimens intercritically annealed at 630 $°C$ and 670 $°C$ respectively. Outside the gauge area, for the specimens intercritically annealed at 630 $°C$ and 670 $°C$ in Figures F.2b and F.2c respectively, the hardness decreases considerable on both sides of the 10 mm gauge, before increasing again. For the specimens intercritically at 590 $°C$, Figure F.2a does not have the same decrease. However, this is due to the average hardness in the gauge of 238 $HV1$ being similar to the hardness in the decreased area of the specimens intercritically annealed at a higher temperature. This indicates a different heat treatment has occurred in the area outside the gauge, which is consistent with the obtained temperature development curves.

In addition to the horizontal measurement of hardness values, vertical measurements were taken to verify that across the width of the 10 mm gauge, there is little deviation in hardness. This is seen in Figure F.3.

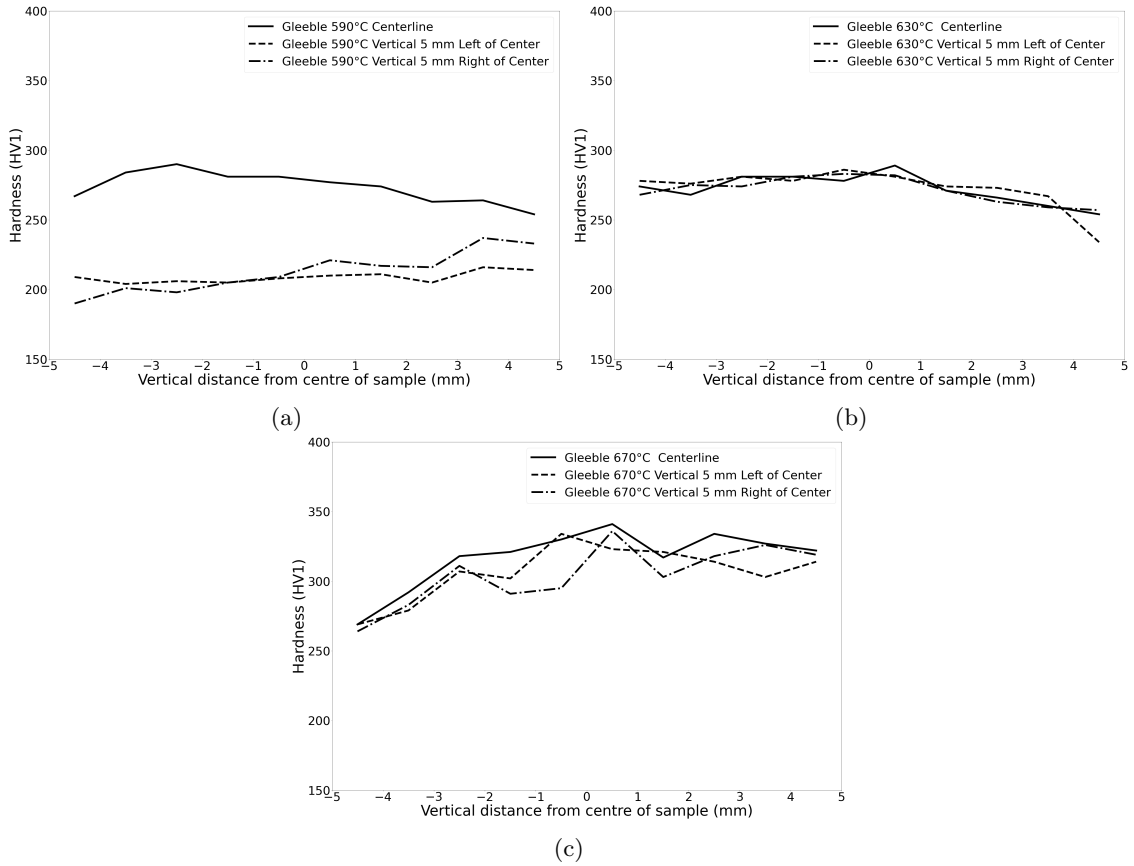

Figure F.3: Vertical hardness profiles obtain for tensile specimen heat treated in the *Gleeble 3800-GTC* thermo-mechanical simulator, taken in the center (green), 5 mm left of the center (yellow) and 5 mm right of the center (orange).

As seen in Figure F.3, for all specimens at all intercritical annealed temperatures, the hardness remains stable across the width of the gauge. Additionally, for the specimens intercritically annealed at 630 $°C$ and 670 $°C$, Figures F.3b and F.3c respectively, the hardness for all three investigated location (in the center and 5 mm right and left of the center) the hardness values are almost identical. This further indicates that the hardness across the horizontal length of the specimen is constant in the gauge. For the specimen intercritically annealed at 590 $°C$, Figure F.3a, the center measurement is higher than that of the edge. This is due to a strip of a high martensite content existing in the center of the specimen. As seen for the dilatometry specimens, there is a presence of texture in the specimens. Coupled with the rolling direction of the steel sheet being perpendicular to the tensile specimen length, this can explain the banding like microstructure obtained through dilatometry and through hardness. Therefore, it is expected that there will be some heterogeneity in the Gleeble specimens, like with dilatometry, during the investigation of the microstructure using SEM.

G Supporting Figures - TDS Plots

The supporting figures for the TDS plots contain the full TDS plots obtained for the various specimens, including both peaks, seen in Figure G.1. Additionally, the peak obtained by only testing the crucible is given in Figure G.2 to show the similarity of the full TDS desorption curves, leading to the changing of the baseline when calculating the absorbed H content.

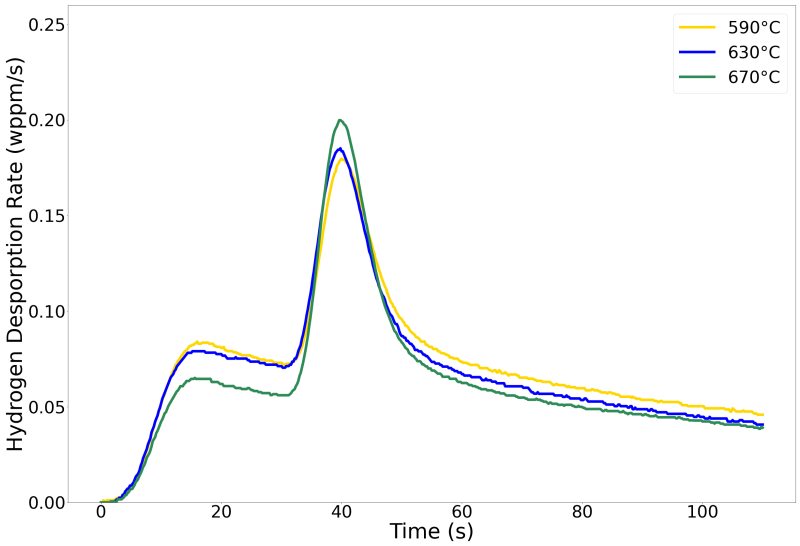

Figure G.1: Obtained TDS curves from the *Bruker Galileo G8 + IR oven* device, showing the desorbed hydrogen content per second as a function of time. For all intercritical annealing temperature. The initial increase is attributed to the crucible and the second to the diffusible H in the charged specimen.

As seen in Figure G.1 there are differences in the obtained curves. However, the main difference between the specimen lies in the peak obtained ($\sim 30\ s$) after the specimen has melted, when the absorbed hydrogen is released.

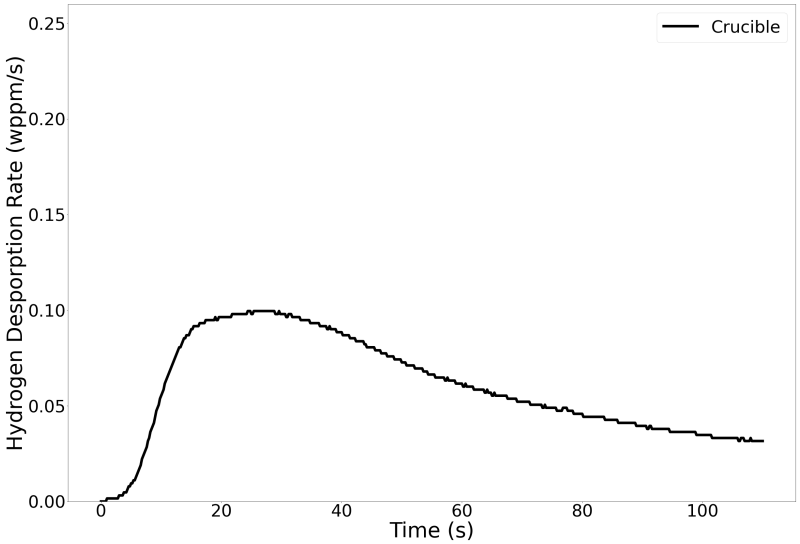

Figure G.2: TDS curve obtained for only the crucible without any H charged specimen present, showing the first curve of all other TDS curves is a result of the crucible and not the specimen.

H Supporting Figures - Nominal SSRT Stress-Strain Curves

The supporting figures of the SSRT testing include the nominal stress-strain curves, and the load-train deformation trend line curve for the estimation of the estimation of the engineering HE SSRT stress-strain curves. The full engineering and nominal stress-strain curves for the benchmarking and HE SSRT scenario are given in Figure H.1.

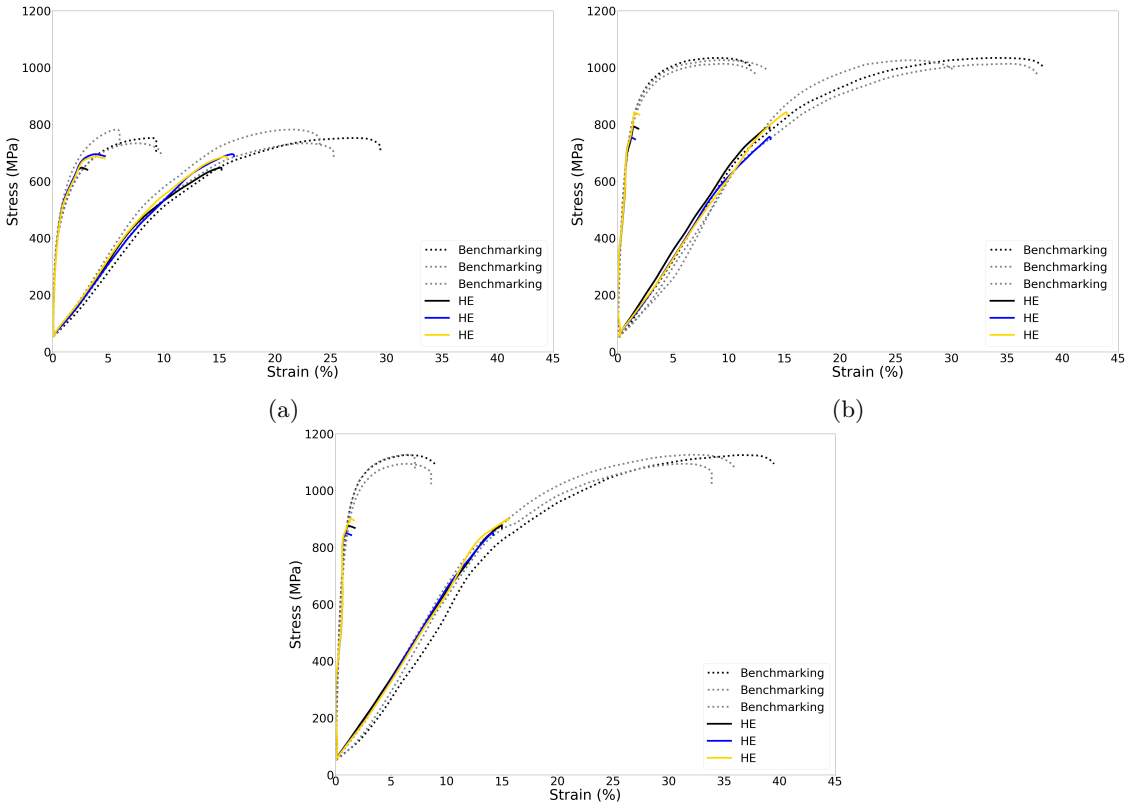

Figure H.1: Engineering stress-strain curves of all SSRT specimens, intercritically annealed at a) 590 $°C$, 630 $°C$, and 670 $°C$ showing the recorded nominal (right) and estimated engineering (left) strain curves as a function of stress. The benchmarking curve is depicted as the dashed line.

As seen in Figure H.1, there is a significant difference between the recorded engineering and nominal strain values. This indicates that the many components of the tensile setup all experience elastic strain during the SSRT tests. Furthermore, when comparing the engineering and nominal strain curves, the former have an equal elastic region for all specimens per intercritical annealing condition. Meanwhile, the elastic region of the nominal strain curves differs more for the different specimens per intercritical annealing condition. Additionally, there are differences in the nominal elongation at fracture, while the engineering strain at fracture are similar. This indicates a hysteresis effect, particularly related to the deformation of the polymeric parts of the tensile setup. Namely, the insulating *rigid resin* sleeve, the paint on the stainless steel grips and the kapton tape between the sleeve and the outer stainless steel grip sleeves.

The load-train deformation curves, showing the strain as a function of stress is given in Figure H.2. Furthermore, the trend line used in the reconstruction of the load-train deformation curve for the estimation of the engineering stress-strain curve is given in the plot.

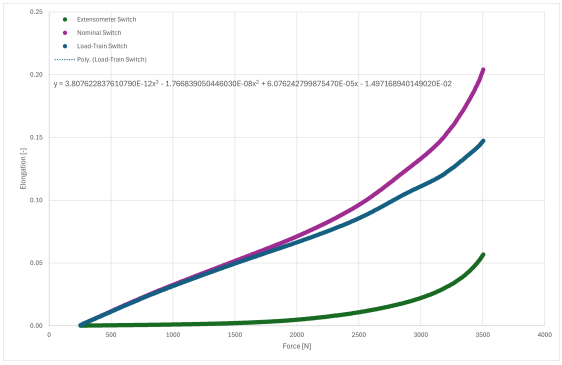

(a) GT590

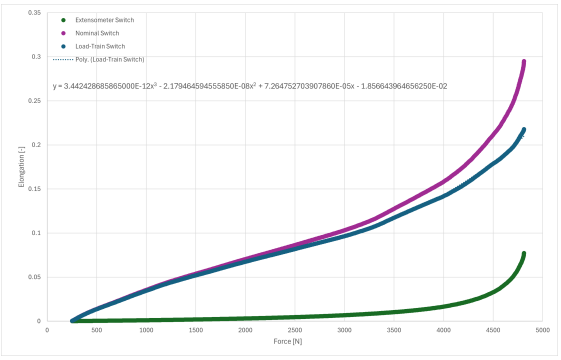

(b) GT630

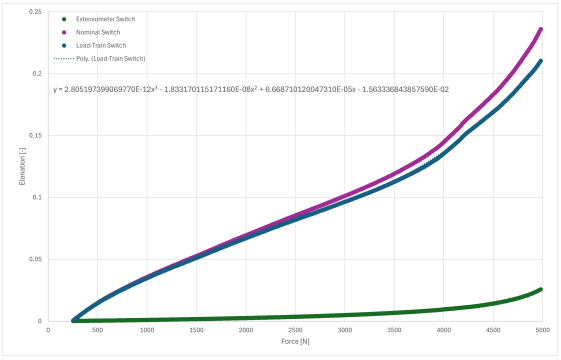

(c) GT670

Figure H.2: Linear regime of the average benchmarking curves, showing the estimation of the load-train displacement by subtracting the engineering strain from the nominal strain. The trend line of the load-train displacement curve, with the equation shown in the graph, expresses the stress of the load-train as a function of strain and is used to model the HE engineering stress-strain curves.

As seen in the curves, the trend line follows the entire part of the stress-strain curve the HE specimens experience, thereby giving an accurate estimation of the load-train displacement for the different specimens. Furthermore, the trend line is chosen to be a third-order polynomial since it most accurately follows the load-train displacement curve.

I Supporting Figures - Fractography Images

The supporting figures from the fractographic analysis include the benchmarking specimens intercritically annealed at 590 $°C$ and 630 $°C$, seen in Figures I.1 and I.2 respectively.

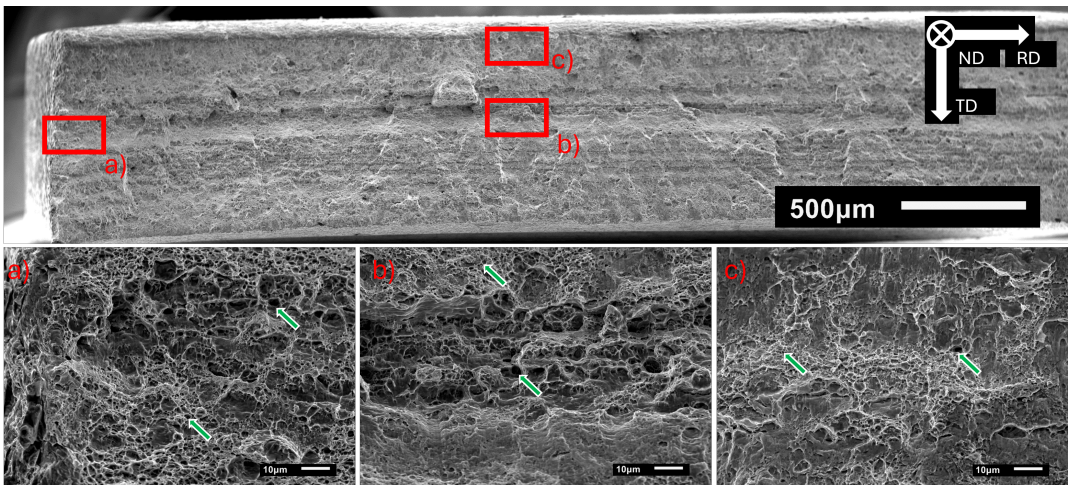

Figure I.1: SEM fractography image of the benchmarking tensile specimen intercritically annealed at 590 $°C$ at magnifications 30x and 1000x showing an overview of the fracture surface and highlighted locations of interest. Locations given clear indications of the dimple ductile fracture area are indicated with green arrows.

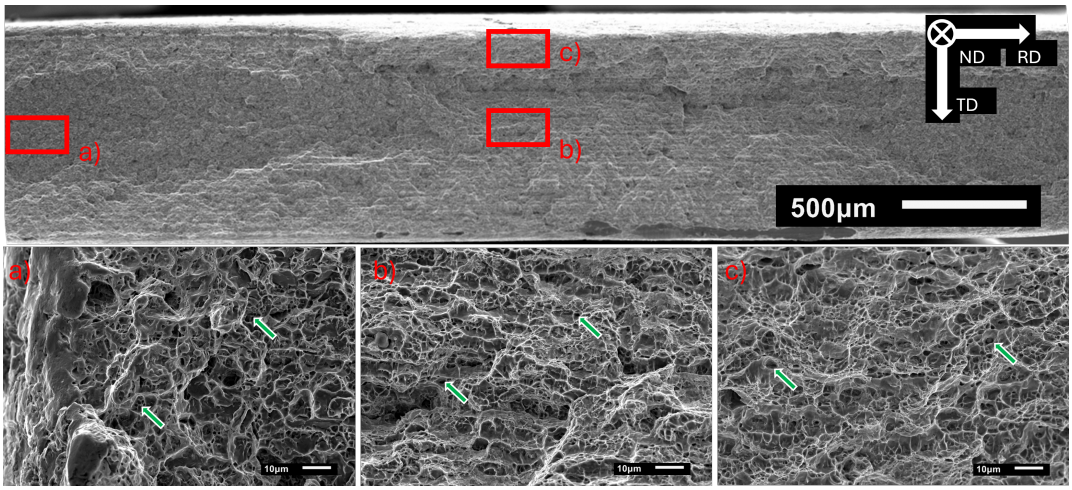

Figure I.2: SEM fractography image of the benchmarking tensile specimen intercritically annealed at 630 $°C$ at magnifications 30x and 1000x showing an overview of the fracture surface and highlighted locations of interest. Locations given clear indications of the dimple ductile fracture area are indicated with green arrows.

As seen in the figures, ductile fracture is the dominant fracture mode for the benchmarking specimens, seen by the presence of ductile dimples. There is no clear difference in the fracture surface across all intercritical annealing conditions.

Further analysis of the cross-section of the 590 $°C$ and 630 $°C$ specimens are given in Figures I.3 and I.4 respectively. For all specimens there is clear difference in the surface microstructure of the long and short edges. Furthermore, the corners consist of ferrite, indicating why quasi-cleavage fracture occurs in the center of the specimen short edge, rather than the specimen corner.

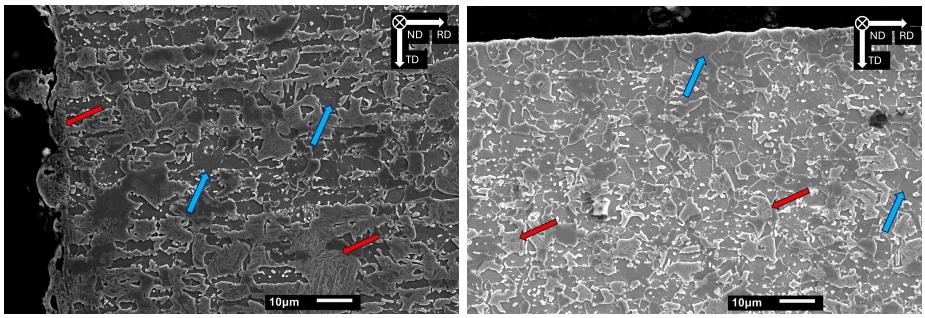

(a) (b)

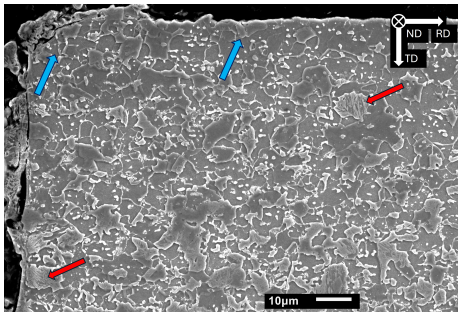

(c)

Figure I.3: SEM images at magnification 1000x of tensile specimens intercritically annealed at 590 $°C$, comparing the a) short and b) long edges and c) corner of the specimen. Ferrite and martensite are respectively indicated by blue and red arrows.

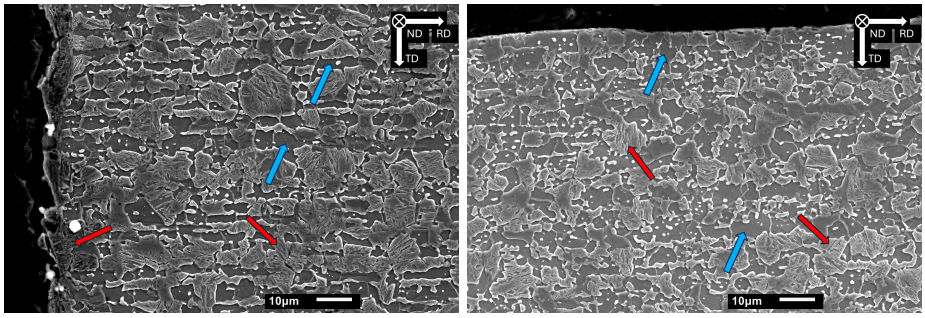

(a) (b)

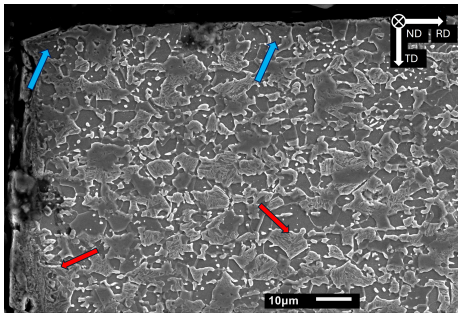

(c)

Figure I.4: SEM images at magnification 1000x of tensile specimens intercritically annealed at 630 $°C$, comparing the a) short and b) long edges and c) corner of the specimen. Ferrite and martensite are respectively indicated by blue and red arrows.